Streamwise Vortices in Hypersonic Flow on a Compression Ramp

Längswirbel in einer Hyperschall-Kompressionsrampenströmung

Von der Fakultät für Maschinenwesen der
Rheinisch-Westfälischen Technischen Hochschule Aachen
zur Erlangung des akademischen Grades eines
Doktors der Ingenieurwissenschaften
genehmigte Dissertation

vorgelegt von

Shibin Cao

Berichter: Univ.-Prof. Dr.-Ing. Herbert Olivier
Univ.-Prof. Dr.-Ing. Wolfgang Schröder

Tag der mündlichen Prüfung: 12.03.2021

Diese Dissertation ist auf den Internetseiten der Universitätsbibliothek online verfügbar.

Acknowledgment

The work presented in this dissertation was carried out during the years I was Ph.D. candidate and research assistant at the Shock Wave Laboratory of RWTH Aachen University. The dissertation was jointly funded by the China Scholarship Council and the Shock Wave Laboratory. The computing resources granted by the JARA Vergabegremium and RWTH Aachen University are gratefully acknowledged.

First of all, I would like to express my appreciation and thanks to my supervisor, the head of the Shock Wave Laboratory, Prof. Dr.-Ing. Herbert Olivier. I greatly appreciate the opportunity given by him to start the research on hypersonic flows. I am very grateful for the supports offered by him, such as the sufficient research freedom, the stimulating discussions, the valuable suggestions for my publications, and so on. His trust, patience and encouragement gave me great confidence in my research. It was his guidance and support that made me a better researcher. I am indebted to Prof. Dr. rer. nat. Igor Klioutchnikov, who provided me with numerous guidance on the implementation of numerical simulations and thoughtful advice on my research topic. I also appreciate his advice about how to present my results at a conference and in an article.

I am also grateful to all of the people that helped me at the Shock Wave Laboratory of RWTH Aachen University, Dr. Manuel Gageik, Mr. Amit Roghelia, Mr. Bastian Hammer, Dr. Sandra Ludescher, Mr. Markus Eichler, Mr. Yilmaz Seker, Mr. Aron Heibges, Dr. Zhiwei Han, Prof. Lin Bao, Dr. Dongdong Zhang, Prof. Qiu Wang, Dr. Sangdi Gu and Dr. Jiaao Hao. Thanks also go to my friends for their company and encouragement during my stay in Aachen.

Finally, I want to express my deepest gratitude to my parents for their care, support and encouragement over the years. The concern and love from my family is always a motivation for me to go ahead. I wish to express special thanks to my girlfriend Xiali for her love and giving me a meaningful and colourful life during the years of my doctoral studies.

Aachen, September 2020

Shibin Cao

Abstract

Compression ramp flows with a free-stream Mach number of 7.7 are numerically studied to uncover the physics beneath the experimentally observed phenomena. This work focuses on laminar SWBLI with a moderate flow separation. Direct numerical simulations (DNS) are performed to investigate the characteristics of the streamwise vortices and surface heat flux streaks occurring in the compression ramp flow. Excellent agreements between the DNS results and experimental data as well as theoretical predictions are achieved. The finite-span effects encountered in experiments are also examined. The DNS results demonstrate the occurrence of streamwise vortices and heat flux streaks in compression ramp flows in the absence of external disturbances. Additionally, the presence of surface heat flux streaks leads to a considerable surface heat transfer enhancement downstream of reattachment. The influence of free-stream Reynolds number and ramp angle on the features of the streamwise vortices and streaks are analysed in detail and compared with experimental measurements.

Another important finding of this dissertation is the flow unsteadiness triggered by the intrinsic instability in the separation bubble. In the fully developed flow, the surface heat flux downstream of reattachment exhibits a broadband low-frequency unsteadiness, which propagates in streamwise direction. Moreover, the unsteadiness of surface heat flux streaks is coupled with a pulsation of the reattachment position. By conducting a dynamic mode decomposition analysis, several oscillatory modes characterised by streamwise low-frequency periodicity are revealed in the separation bubble flow. This flow structure originates from the instability of the separation bubble flow and is linked to the downstream reattached flow by the shear layer above the bubble.

To evaluate the centrifugal instability resulting from the local streamline curvature near reattachment, the Görtler number for a compression ramp flow is accurately determined via different methods. The first one gives the variation of the Görtler number near reattachment on the basis of the DNS data. Additionally, based on a simplified physical model, a formula depending only on the flow conditions and the geometry of compression ramp is deduced to predict the Görtler number. Furthermore, it is found that the Görtler number increases with increasing ramp angle and unit Reynolds number, and it decreases with increasing Mach number and wall-to-stagnation temperature ratio.

Kurzfassung

In dieser Arbeit erfolgt die numerische Simulation mittels DNS (Direkte Numerische Simulation) einer Kompressionsrampenströmung bei einer Anströmmachzahl von 7,7. Ziel ist hierbei ein besseres physikalisches Verständnis der im Experiment beobachteten Phänomene. Die Strömung ist charakterisiert durch eine laminare Stoß/Grenzschichtwechselwirkung einhergehend mit einer moderaten Strömungsablösung. Die durchgeführten direkten numerischen Simulationen erlauben eine detaillierte Analyse beobachteter Längswirbel und entsprechender in Spannweitenrichtung periodisch auftretender Wärmestromstrukturen. Die numerisch erzielten Ergebnisse, experimentelle Daten als auch theoretische Vorhersagen zeigen eine sehr gute Übereinstimmung. Einflüsse einer endlichen Spannweite der Windkanalmodelle im Experiment werden ebenfalls numerisch untersucht. Auch bei Abwesenheit einer externen Störungsanregung zeigen die numerischen Ergebnisse auf der Kompressionsrampe typische Längswirbel- und Wärmestromstrukturen. Diese Wärmestromverteilungen führen auf der Kompressionsrampe zu einer signifikanten Erhöhung der Wärmestrombelastung. Einflüsse der Reynoldszahl und des Rampenwinkels werden ebenfalls analysiert und mit experimentellen Daten verglichen.

Ein weiteres wichtiges Ergebnis dieser Arbeit betrifft die beobachtete Strömungsinstationarität hervorgerufen durch eine Instabilitätsform der Strömung innerhalb der Ablöseblase. Anhand der zeitlichen Wärmestromverteilung stromab des Wiederanlegebereichs wird eine niederfrequente Instationarität identifiziert, die sich stromab ausbreitet. Dieser Instationaritätsmode wird zurückgeführt auf eine oszillierende Bewegung der Wiederanlegelinie. Eine DMD (Dynamic Mode Decompostion)-Analyse zeigt, dass der Ursprung der Instationarität gekoppelt ist am Auftreten verschiedener nierderfrequenter Vorgänge innerhalb der Ablöseblase, die von der freien Scherschicht stromab transportiert werden.

Zur Charakterisierung der im Wiederanlegebereich der Strömung auftretenden Zentrifugalinstabilität wird die Göthertzahl mit Hilfe zweier unterschiedlicher Vorgehensweisen bestimmt. Diese umfassen die Bestimmung mittels numerischer Daten als auch eines einfachen physikalischen Modells zur Abschätzung der Stromlinienkrümmung und der Scherschichtdicke vor dem Wiederanlegebereich. Basierend hierauf zeigt sich, dass die Göthertzahl mit zunehmendem Rampenwinkel und zunehmender Reynoldszahl ebenfalls wächst, während sie mit zumehmender Machzahl und zunehmendem Wandtemperaturverhältnis eine abnehmende Tendenz aufweist.

Contents

Acknowledgment **i**

Abstract **iii**

Kurzfassung **v**

List of Figures **xiv**

List of Tables **xv**

Nomenclature **xvii**

1 Introduction **1**
1.1 Motivation 1
1.2 Shock wave/boundary layer interaction (SWBLI) 2
1.2.1 Hypersonic compression ramp flow 2
1.2.2 Influencing parameters 5
1.3 Streamwise vortices in SWBLI 6
1.3.1 Streamwise heat flux streaks 6
1.3.2 Görtler vortices 7
1.3.3 Global instability of SWBLI 9
1.3.4 Baroclinic effects 11
1.3.5 Influence of leading-edge geometry 11
1.4 Low-frequency unsteadiness in SWBLI 13
1.5 Objectives and outline 14

2 Numerical methodology **17**
2.1 Governing equations 17
2.2 Discretisation approaches 19
2.2.1 WENO scheme - inviscid terms 20
2.2.2 Central difference scheme - viscous terms 22
2.2.3 TVD Runge-Kutta scheme - temporal terms 24
2.3 Boundary and initial conditions 25
2.4 Further numerical implementation 29

3 Mesh Study and Validation **31**
3.1 Region I: Hypersonic laminar boundary layer flow on a flat plate 31

3.2 Region II: Laminar separation in hypersonic compression ramp flow 35
3.3 Region III: Streamwise vortices downstream of reattachment 40
3.4 High Reynolds number condition 48
3.5 Finite-span effects 52
3.6 Summary 57

4 Streamwise vortices in hypersonic compression ramp flows 59
4.1 Basic characteristics 59
4.2 Surface heat transfer enhancement 62
4.3 Further remarks on the wavelength of the streamwise streaks 66
4.4 Effects of ramp angle 68
4.5 Three-dimensionality near reattachment 72
4.6 Summary 74

5 Unsteady effects in laminar separated hypersonic compression ramp flows 75
5.1 Unsteady effects for a low Reynolds number case 75
5.1.1 Spatio-temporal distribution of the surface heat flux 75
5.1.2 Unsteady features at flow reattachment 78
5.1.3 Dynamic mode decomposition of the separation bubble flow 79
5.2 Unsteady effects for a high Reynolds number case 85
5.3 Summary 88

6 Görtler number evaluation for laminar separated compression ramp flow 91
6.1 Determination of Görtler number 91
6.1.1 Numerical approach 91
6.1.2 Simplified approach 93
6.1.3 Verification of the separation bubble length and the simplified method 98
6.2 Görtler number variation in compression ramp flow 101
6.2.1 Further remarks on wall temperature influence 103
6.3 Summary 103

7 Conclusion 105

Bibliography 109

List of Figures

1.1 Canonical configurations employed for fundamental studies of SWBLI [3]. . 2
1.2 Sketch of a well-separated hypersonic compression ramp flow. 4
1.3 Typical wall pressure distribution for a well-separated compression ramp flow. S and R denote the separation and reattachment position, respectively. 4
1.4 Typical skin friction coefficient distribution for a well-separated compression ramp flow. S and R denote the separation and reattachment position, respectively. 5
1.5 Surface heat flux streaks observed on compression ramps in different experiments: (a) Simeonides and Haase [15], (b) Roghelia et al. [16], (c) Chuvakhov et al. [13]. Flow from left to right. 6
1.6 Sketch of Görtler vortices [26]. 7
1.7 Mechanism for the formation of streamwise streaks due to Görtler vortices, adopted from Yang et al. [20] and Ishiguro et al. [25]. 8
1.8 Determination of the radius of curvature for the concave shear layer in a compression ramp flow proposed by (a) Grasso and Marini [35], (b) Navarro-Martinez and Tutty [24] and (c) Roghelia et al. [16]. 9
1.9 (a) Schematic showing the variation of the turn angle for a double wedge flow. (b) Shape of the unstable mode at the critical angle. Both figures are adopted from the study of Sidharth et al. [44]. 10
1.10 Mechanism for the formation of streamwise vortices due to baroclinic effects, adapted from Zapryagaev et al. [51]. 12
1.11 Schematics of the flow structure for the low-frequency dynamics in a turbulent compression ramp flow, adapted from Priebe and Martín [6]. 13

2.1 Schematic illustration of sub-stencils for the calculation of the cell boundary flux $F_{i+\frac{1}{2}}$ including the flux vector splitting. 22
2.2 Physical domain with boundary conditions. 25
2.3 Schematic illustration for the out-flow boundary condition. f corresponds to density, velocity and pressure. n denotes the direction normal to the boundary. 26
2.4 Schematic illustration for the wall boundary conditions. f corresponds to temperature (for an adiabatic wall). n denotes the direction normal to the wall. 27
2.5 Schematic illustration for the periodic boundary condition. 28
2.6 Schematic illustration for the internal communication between two neighbouring sub-domains. 29

3.1 Regions of compression ramp flow. 31
3.2 Mesh distribution for case A2 (each 5th point is shown). 32
3.3 Temporal history of pressure and temperature signals at $x/L = 1$ and $y/L = 0.0012$ for case A2. 33
3.4 Streamwise distribution of the surface pressure on the flat plate for case A. 34
3.5 Streamwise distribution of the skin friction coefficient for case A. The theoretical value is calculated with Eq. 3.3. 35
3.6 Flat plate boundary layer profiles at $x/L = 1$ for case A. 36
3.7 Mesh distribution for case B3 (each 5th point is shown). 37
3.8 Temporal evolution of the separation (x_s) and reattachment (x_r) point for case B3. 37
3.9 Numerical schlieren for case B3. The symbols s, r and T denote the separation position, reattachment position and triple point, respectively. 38
3.10 Pressure coefficient and Stanton number distributions along the wall for case B. 39
3.11 Comparison of the surface pressure coefficient for the present DNS results and the results obtained by Gai and Khraibut [86]. 40
3.12 Mesh distribution for case C4 (each 8th point is shown). 41
3.13 Wall Stanton number distribution (top view) for case C4 at different instants of time, a)-f) correspond to $\bar{t} = 0$, 9, 21, 45, 60, 120. Solid lines denote iso-lines of zero skin friction coefficient. Flow from left to right. . . 42
3.14 Temporal history of the wall Stanton number at $x/L = 1.5$ and $z/L = 0.5$ for case C4. 43
3.15 Temporal growth of the standard deviation of the spanwise Stanton number variation (Eq. 3.8) at $x/L = 1.5$ for case C4. 44
3.16 Temporal growth of the spanwise velocity (Eq. 3.9) at $x/L = 1.04$ for case C4. 44
3.17 Streamwise distribution of the spanwise velocity (Eq. 3.9) at $\bar{t} = 9$ for case C4. 45
3.18 Temporal history of the wall Stanton number at $x/L = 1.5$ and $z/L = 0.5$ for case C2 and $x/L = 1.5$ and $z/L = 0.15$ for case C5. 45
3.19 Wall Stanton number distributions (top view) for case C1 at $\bar{t} = 30$ and cases C2-C5 at $\bar{t} = 60$. a)-e) correspond to cases C1, C2, C3, C4 and C5. Solid lines denote iso-lines of zero skin friction coefficient. Flow from left to right. 46
3.20 Spanwise wall Stanton number distributions for cases C1-C5 at $x/L = 1.4$ and the same instants of time as in figure 3.19. 47
3.21 Temporal evolution of the separation and reattachment positions for the 2-D simulation of case D1. 49
3.22 Streamwise distribution of (a) the skin friction coefficient and (b) the wall Stanton number for the converged 2-D results of cases D1 and D2. The theoretical value is calculated based on Eq. 3.3. 50

3.23 Wall Stanton number distribution (top view) for case D1 at different instants of time, a)-d) correspond to $\bar{t}$ = 0, 10, 20, 50. Solid lines denote iso-lines of zero skin friction coefficient. Flow from left to right. 50
3.24 Temporal history of the wall Stanton number at $x/L = 1.45$ and $z/L = 0.5$ for case D1. 51
3.25 Temporal growth of the standard deviation of the spanwise Stanton number variation (Eq. 3.8) at $x/L = 1.45$ for case D1. 51
3.26 Temporal growth of the spanwise velocity (Eq. 3.9) at $x/L = 1.04$ for case D1. 52
3.27 (a) Wall Stanton number distribution at $\bar{t} = 10$ for case D2. (b) Spanwise distribution of the wall Stanton number at $x/L = 1.45$ and $\bar{t} = 10$ for cases D1 and D2. 53
3.28 Streamwise distribution of the surface pressure coefficient and wall Stanton number on the symmetry plane for case C4 in comparison with the experimental data [16]. 54
3.29 Streamwise distribution of the surface pressure coefficient and wall Stanton number on the symmetry plane for case D1 in comparison with the experimental data [78]. 55
3.30 Streamwise distribution of the surface pressure coefficient and wall Stanton number for the validation case: Condition I, ramp angle = 20°, experimental data [16]. 56
3.31 Surface Stanton number distribution for the validation case: Condition I, ramp angle = 20°. 56

4.1 Instantaneous hypersonic compression ramp flow: (a) $M_\infty = 7.7$, $Re_{\infty,L} = 4.2 \times 10^5$, $\bar{t} = 100$ (case C4); (b) $M_\infty = 7.7$, $Re_{\infty,L} = 8.6 \times 10^5$, $\bar{t} = 60$ (case D1). 60
4.2 Vortex structure visualised by in-plane streamlines at $x/L = 1.5$ (case C4). Streamwise velocity contour u/u_∞ coloured for levels below 0.95 is also shown. 60
4.3 Vortex structure visualised by in-plane streamlines at $x/L = 1.45$ (case D1). Streamwise velocity contour u/u_∞ coloured for levels below 0.92 is also shown. 61
4.4 Time-averaged flow field for case C4. Wall Stanton number and density gradient is shown. 62
4.5 Spanwise variation of the wall Stanton number at $x/L = 1.5$ for the instantaneous and time-averaged flows (case C4). 63
4.6 Streamwise distribution of the spanwise-averaged wall Stanton number (solid line) and the standard deviation of the spanwise variation (dashed lines) for (a) the instantaneous flow ($\bar{t} = 100$) and (b) time-averaged flow. . 63

4.7 Streamwise distribution of the spanwise-averaged Stanton number for instantaneous and time-averaged flow in comparison with the 2-D solution (case C4). 64
4.8 Time-averaged flow field for case D1, wall Stanton number and density gradient. 65
4.9 Spanwise variation of the wall Stanton number at $x/L = 1.45$ for the instantaneous and time-averaged flows (case D1). 65
4.10 Streamwise distribution of the spanwise-averaged Stanton number for instantaneous and time-averaged flow in comparison with the 2-D solution (case D1). 65
4.11 Power spectra density as a function of wavelength for the spanwise variation of the wall Stanton number at $x/L = 1.5$ for the time-averaged flow (case C4). 66
4.12 Time-averaged distribution of the spanwise velocity field on different planes (case C4): (a) wall-parallel plane at $y_n/L = 0.009$. (b) z-y plane at $x/L = 1.04$. (c) x-y plane at $z/L = 0.6$. The density gradient at $z/L = 0$ is shown in (a) to highlight the position of the separation bubble. 67
4.13 Power spectra density as a function of wavelength for the spanwise variation of the wall Stanton number at $x/L = 1.45$ for the time-averaged flow (case D1). 68
4.14 Time-averaged distribution of the spanwise velocity field on the z-y plane at $x/L = 1.04$ (case D1). The same legend as figure 4.12 is used here. . . . 68
4.15 Time-averaged flow field for (a) case D3 and (b) case D4. The density gradient is shown for the plane at $z/L = 0$. Solid lines on the surface correspond to $c_f = 0$. 69
4.16 Temporal history of the wall Stanton number at $x/L = 1.45$ and $z/L = 0.5$ for case D4. 70
4.17 Streamwise distribution of the time- and spanwise-averaged (a) skin friction coefficient and (b) wall Stanton number for cases D1, D3 and D4. 71
4.18 Spanwise distribution of the wall Stanton number at $x/L = 1.4$ for (a) case D3 and (b) case D4. Dashed line corresponds to the instantaneous flow ($\bar{t} = 30$) and solid line to the time-averaged flow. 72
4.19 Streamwise distribution of the spanwise-averaged Stanton number for the instantaneous ($\bar{t} = 30$) and time-averaged flow in comparison with the 2-D solution for (a) case D3 and (b) case D4. 73
4.20 Schematic configuration of local streamlines in the reattachment region proposed by (a) Ginoux [12] and (b) the present thesis. (c) Streamlines on a near-wall plane ($y_n/L = 0.0008$) embedded in the wall Stanton number contour for case D1. N and S denote nodes and saddle points, respectively. 73

5.1 Temporal history of the wall Stanton number at $x/L = 1.5$ and $z/L = 0.5$ (case C4). 76

5.2 Relative standard deviation of the wall Stanton number for all spanwise positions at $x/L = 1.5$ (case C4). 76
5.3 Two-point temporal correlation maps for the wall Stanton number in (a) streamwise direction and (b) spanwise direction. Reference point is located at $x/L = 1.5$, $z/L = 0.5$ (case C4). 77
5.4 (a) Power spectra density of the wall Stanton number signal at $x/L = 1.5$ and $z/L = 0.5$. (b) Power spectra density map for all spanwise positions at $x/L = 1.5$. 78
5.5 Temporal history of reattachment positions in comparison with wall Stanton number. Black solid line corresponds to the reattachment position for the symmetry-plane ($z/L = 0.5$) and dash dot line to the spanwise-averaged reattachment position. Dashed line represents the wall Stanton number signal shown in figure 5.1. 79
5.6 (a) Spectrum of the eigenvalues obtained from the standard DMD (circle) and the modes selected by SPDMD (red triangle) for a subset of $N_{sp} = 9$. (b) A zoomed view for the selected modes. Green line is the unit circle. . . 82
5.7 DMD modes visualised by contours of spanwise velocity component (w/u_∞). (a-d) correspond to the real part of modes M0, M1, M3 and M4. 83
5.8 Flow structure of the oscillatory unstable modes revealed by the global stability analysis performed by (a) Sidharth et al. [44] and (b) Cao et al. [93]. 84
5.9 (a) Two iso-lines for $u/u_\infty = 0.1$ and $u/u_\infty = 0.9$ embedded in the contour of the dimensionless velocity gradient $\partial\bar{u}/\partial\bar{y}$ which highlights the shear layer. (b) The same iso-lines as in (a) embedded in the contour showing the real part of mode M4. 84
5.10 Relative standard deviation of the wall Stanton number for all spanwise positions at $x/L = 1.45$ (case D1). 85
5.11 Two-point temporal correlation maps for the wall Stanton number in (a) streamwise direction and (b) spanwise direction. Reference point is located at $x/L = 1.45$, $z/L = 0.5$ (case D1). 86
5.12 (a) Power spectra density map for all spanwise positions at $x/L = 1.45$ for case D1. (b) Spanwise-averaged PSD as a function of the nondimensional frequency for cases C4 ($x/L = 1.5$) and D1 ($x/L = 1.45$). 87
5.13 (a) Spectrum of the eigenvalues obtained from the standard DMD (circle) and the modes selected by SPDMD (red triangle) for a subset of $N_{sp} = 12$. (b) A zoomed view for the mode selection. Green line is the unit circle. . . 88
5.14 DMD modes visualised by contours of the spanwise velocity component. (a-d) correspond to the real part of modes N2, N4, N9 and N10. Circle dots denote the separation and reattachment positions. 89

6.1 Enlarged view of the reattaching shear layer quantified by the velocity gradient ($\partial\bar{u}/\partial\bar{y}$). The shown streamlines originate upstream of separation. The flow field is averaged in time and in spanwise direction for case D1. . . 92
6.2 (a) Non-dimensional streamline curvature distribution near reattachment for cases D1, D3 and D4 with different ramp angles. Straight lines represent the constant values estimated by Eq. (6.3). (b) Momentum thickness of the free shear layer near reattachment. 93
6.3 Görtler number distribution near reattachment for cases (a) D1, (b) D3, (c) D4 and (d) the three cases. Reattachment points are obtained from the time and spanwise averaged skin friction distributions. The straight lines are determined by Eq. (6.8) which is shown in the following. 94
6.4 Geometrical model for Görtler number estimation, a) original model in reference [98], b) model proposed in the present thesis. 95
6.5 Variation of the normalised separation bubble length with the scaled angle α. case 1 (cross); case 2 (triangle); case 3 (diamond); case 4 (square); case 5 (asterisk); case 6 (arrow). 99
6.6 Görtler stability diagram for different cases. Present thesis: ■ - E1, ▲ - E2, ▼ - E3; □ - Roghelia [16]; ▷ - Chuvakhov [13]; ◯ - Navarro-Martinez [24]; ◊ - Ohmichi [37]; Neutral curve - El-Hady and Verma [105]. 100
6.7 Variation of Görtler number and streamline curvature with (a) ramp angle, (b) unit Reynolds number, (c) Mach number, and (d) wall-to-stagnation temperature ratio. 102
6.8 Numerical schlieren for three cases listed in Table 6.1 with different wall and stagnation temperatures. The reattachment point is highlighted. . . . 104

List of Tables

2.1 Coefficients $a^r_{m,l}$ for a fifth-order WENO scheme [65]. 20

3.1 Flow conditions: Condition I at the shock tunnel TH2 [78]. 32
3.2 Cases for the mesh study of the flat plate boundary layer flow. 32
3.3 Cases for the mesh study of the two-dimensional compression ramp flow. . 36
3.4 Separation and reattachment positions and the separation bubble length for case B. 39
3.5 Three-dimensional mesh cases for the grid independence study. 41
3.6 Flow conditions: Condition XI at the shock tunnel TH2 [78]. 48
3.7 Cases for the mesh study of Condition XI. 49

4.1 Cases for investigating the effects of ramp angle. 69

6.1 Selected cases for the verification of the separation bubble length 98
6.2 Selected cases for the verification of the simplified approach 100

Nomenclature

Abbreviations

2-D	**Two-D**imensional
3-D	**Three-D**imensional
BC	**B**oundary **C**ondition
CFD	**C**omputational **F**luid **D**ynamics
DMD	**D**ynamic **M**ode **D**ecomposition
DNS	**D**irect **N**umerical **S**imulation
FFT	**F**ast **F**ourier **T**ransform
GSA	**G**lobal **S**tability **A**nalysis
MPI	**M**essage **P**assing **I**nterface
PSD	**P**ower **S**pectra **D**ensity
RSD	**R**elative **S**tandard **D**eviation
SPDMD	**S**parsity-**P**romoting **D**ynamic **M**ode **D**ecomposition
std	**st**andard **d**eviation
SVD	**S**ingular **V**alue **D**ecomposition
SWBLI	**S**hock **W**ave/**B**oundary **L**ayer **I**nteraction
TVD	**T**otal **V**ariation **D**iminishing
WENO	**W**eighted **E**ssentially **N**on-**O**scillatory

Roman Symbols

a_∞	free-stream speed of sound
a, b, c, d	coefficients for the WENO scheme
C	$= \rho_w \mu_w / \rho_\infty \mu_\infty$, Chapman–Rubesin coefficient
C_D, C_P	coefficients of the central difference scheme
c_f	$= \tau_w / (0.5 \rho_\infty u_\infty^2)$, skin friction coefficient

c_p	$= (p - p_\infty)/(0.5\rho_\infty u_\infty^2)$, wall pressure coefficient
e	total energy
f	representative of parameters in a function; frequency
F, G, H	flux vector in the ξ-, η- and ζ-direction
g	index for ghost grid
G	Görtler number for a laminar flow
G_T	Görtler number for a turbulent flow
h_0	total enthalpy
i, j, k	index for the grid point in the ξ-, η- and ζ-direction
L	flat plate length
L_b	separation bubble length
L_z	spanwise length
M	Mach number
N_i, N_j, N_k	number of grid points in the ξ-, η- and ζ-direction
N_{sp}	number of modes selected by SPDMD
p	pressure
q_w	surface heat flux
q_∞	freestream values
Pr	Prandtl number
R	radius of curvature
R_{nm}	two-point spatio-temporal correlation parameter
Re	unit Reynolds number
St	wall Stanton number
St_z	spanwise-averaged wall Stanton number
$\overline{St}$	time-averaged wall Stanton number
$\widehat{St}$	relative standard deviation of wall Stanton number
$\bar{t}$	$= tu_\infty/L$, non-dimensional time
T	temperature, triple point
T_0	total temperature
U	solution vector
u, v, w	velocity component
x, y, z	Cartesian coordinate system

Greek Symbols

α	scaled angle
β	non-dimensional wavenumber
δ	boundary layer thickness
δ_1	boundary layer displacement thickness
δ_2	boundary layer momentum thickness
δ_s	boundary layer thickness at separation
δ_r	shear layer thickness at reattachment
ξ, η, ζ	curvilinear coordinate system
γ	ratio of specific heats; regularisation parameter for SPDMD
λ	wavelength; shear constant; eigenvalue of the Jacobian matrix
Λ	Görtler number based on wavelength
θ_f	ramp angle
θ_s	separation angle
θ_{inc}	incipient separation angle
μ	viscosity
μ_i	eigenvalue of an individual DMD mode
ρ	density
$\bar{\chi}$	$= M_\infty^3\sqrt{C}/\sqrt{Re_{\infty,x}}$, viscous interaction parameter
ω	vorticity; normalised nonlinear weights coefficient
Φ_i	DMD modes
σ	root-mean-square value
τ	time delay; shear stress
τ_w	wall shear stress

Subscripts

aw	adiabatic wall condition
e	condition at the edge of the boundary layer
r	reattachment
s	separation

w	wall condition
∞	freestream condition

Superscripts

$*$	values evaluated at the Eckert reference temperature

1 Introduction

1.1 Motivation

Shock wave/boundary layer interaction (SWBLI) is ubiquitous in high-speed flight relating to transonic, supersonic and hypersonic vehicles. When a boundary layer on the surfaces of a vehicle (either internal or external) encounters a shock wave, e.g., generated by an adjacent or opposite surface or by a back pressure that constrains the flow, a complex viscous-inviscid coupling takes place causing dramatic changes in the flowfield. If the adverse pressure gradient induced by the shock wave is strong enough to cause boundary layer separation, the consequence of the interaction is exacerbated with the formation of intense vortices, complex shock patterns, large-scale unsteadiness, etc. The practical impact on the vehicle can be very harmful and must be considered for design tradeoffs. From both engineering and theoretical points of view, heat transfer rates and flow unsteadiness are perhaps the main issues of interest in the framework of SWBLI [1–3].

The presence of SWBLI can lead to severe thermal loads with peak heating rates up to 10-100 times that under the incoming attached boundary-layer flow [1]. Therefore, one main task is to predict the location and magnitude of the heating peak. The difficulty is amplified by the occurrence of spatial and temporal variation of the heat transfer. Numerous experiments have demonstrated the ubiquitous presence of streamwise surface heat flux streaks (or temperature streaks on an adiabatic wall), either in two-dimensional (2-D) or general three-dimensional (3-D) configurations. The streamwise streaks are often associated with streamwise vortices that seem to be a typical consequence of SWBLI [4]. However, the physical mechanism responsible for their formation and evolution is still not well understood, which motivates this thesis.

Numerous studies involving SWBLI, especially in strong interactions, have inevitably encountered flow unsteadiness. In turbulent SWBLI, the unsteady flowfield is associated with low-frequency, large-scale motions of the dominant flow structures, e.g., oscillation of the shock and breathing of the separated region [5]. The low-frequency unsteadiness is driven both by fluctuations in the upstream boundary layer and some large-scale instabilities intrinsic to the separated flow. For strong separations, the dominant mechanism is the inherent instability in the separated flow [5, 6]. Essentially, the inherent instability of a separated flow is irrespective of the state of the upstream boundary layer, which motivates the present thesis to investigate the potential flow unsteadiness in the instance of an undisturbed laminar incoming boundary layer and the effects of flow unsteadiness on the behaviour of streamwise heat flux streaks. An improved understanding of the physics

in laminar SWBLI also contributes to the prediction and control of laminar-turbulent transition in this case.

1.2 Shock wave/boundary layer interaction (SWBLI)

The fundamental physics of SWBLI are typically examined in classical situations, among which some common configurations are shown in figure 1.1 [3]. As pointed out by Délery et al. [7], the basic physics of SWBLI exhibit close similitude among many configurations. In the present thesis, a compression ramp (figure 1.1(b)) is employed because this simple model enables a fundamental investigation of the flow around control surfaces, engine inlets, body flaps, junctions, etc., of high-speed vehicles.

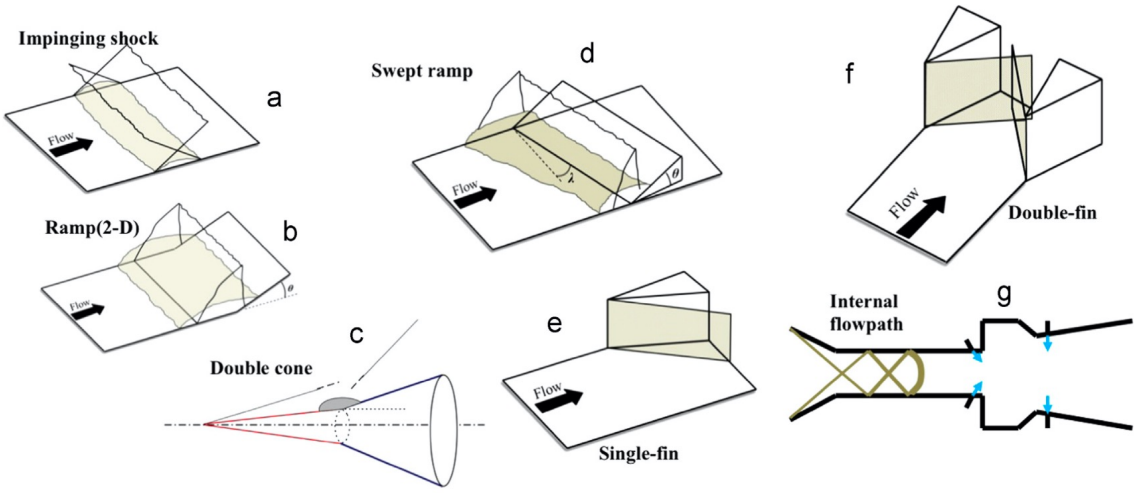


Figure 1.1: Canonical configurations employed for fundamental studies of SWBLI [3].

1.2.1 Hypersonic compression ramp flow

When a flat plate is followed by a ramp plate with a certain deflection angle, which comprises the compression ramp configuration, an oblique shock ideally forms at the corner if the free-stream is supersonic. As a result, the boundary layer on the flat plate is subjected to an adverse pressure gradient induced by the shock. During the interaction, the flow behaviour is determined by the resistance of the boundary layer to the pressure rise [2]. The adverse pressure is balanced by the flow momentum carried by the boundary layer and shear forces in the near-wall region. Note that shear forces play a predominant role in the case of a laminar boundary layer, which is termed a viscous-dominated flow. Therefore, the resistance of a laminar boundary layer to the adverse pressure gradient is sensitive to Reynolds number. However, in a turbulent flow, the influence of the shear forces is less obvious and the interaction depends weakly, in general, on the Reynolds

number, because the velocity profile of a turbulent boundary layer is much fuller, thus carrying more momentum. In this context, a turbulent boundary layer is preferred when one aims to avoid or delay flow separation. However, a laminar flow is sometimes preferred, for example, due to a lower heating load.

If the strength of the shock wave is further increased (e.g., by increasing the ramp angle), the boundary layer may no longer withstand the induced adverse pressure gradient and eventually separate near the corner. The situation at which the flow starts separating is called incipient separation. The critical ramp angle for the incipient separation in a laminar compression ramp flow is given by Needham [8]:

$$\theta_{\mathrm{inc}} = 80\sqrt{\bar{\chi}_L}/M_\infty, \tag{1.1}$$

where M_∞ denotes the free-stream Mach number, and $\bar{\chi}_L$ is the viscous interaction parameter evaluated at the ramp corner:

$$\bar{\chi}_L = M_\infty^3\sqrt{C}/\sqrt{Re_{\infty,L}}, \tag{1.2}$$

with $C = \rho_w\mu_w/\rho_\infty\mu_\infty$ being the Chapman–Rubesin coefficient and $Re_{\infty,L}$ the free-stream Reynolds number based on the flat plate length L.

A strong interaction usually corresponds to a situation with separated boundary layer which results in a reorganisation of the flow-field structure. Figure 1.2 schematically shows a well-separated compression ramp flow. Owing to a large adverse pressure gradient, the boundary layer flow separates ahead of the corner and reattaches on the ramp surface, forming a separation bubble with a recirculating flow between the separation point and reattachment point. A dividing streamline originating from the separation point and terminating at the reattachment point separates the recirculating flow from the flow streaming from upstream to downstream. A free shear layer forms closely above the separation bubble, where an energy transfer occurs from the outer high-speed flow towards the separated region.

Regarding the shock system, a relatively weak shock is generated at the leading edge of the flat plate due to the viscous interaction. A separation shock is formed above the separation point as a response to the deflection of the shear layer. The reattachment process produces a sequence of compression waves that coalesce into a reattachment shock in the outer stream. The separation shock and the reattachment shock meet at the triple point 'T' producing a main ramp shock at a certain distance above the wall and, most commonly, an expansion fan propagating towards the wall. It is noted that the consequence of the intersection of the separation and reattachment shock is not always an expansion fan, but can also be a weak shock, for example, at low supersonic Mach numbers [2]. This pattern of shock-shock interaction belongs to type VI interference according to the classification of Edney [9].

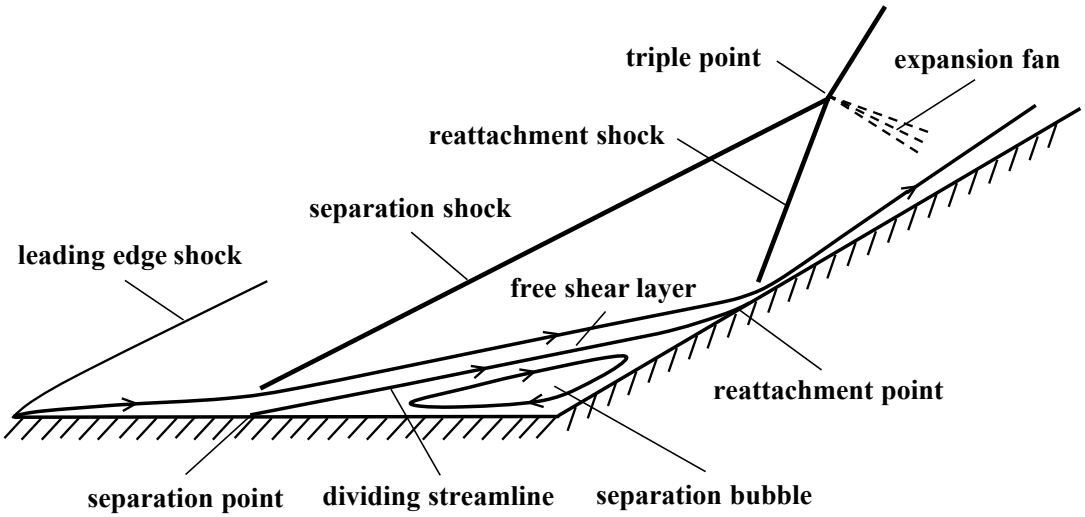


Figure 1.2: Sketch of a well-separated hypersonic compression ramp flow.

Figure 1.3 shows a typical wall pressure distribution for a well-separated compression ramp flow. An initial pressure rise occurs during the separation process, followed by a pressure plateau in the separated region. A second and more progressive pressure rise takes place during the reattachment process. The separation and reattachment positions can be easily identified from the skin friction coefficient (c_f) distribution along the wall, as shown in figure 1.4. The separation and reattachment points are located at which the skin friction is zero on the flat plate and the ramp respectively. The x-wise distance between the two positions is defined as the separation bubble length L_b in the present thesis.

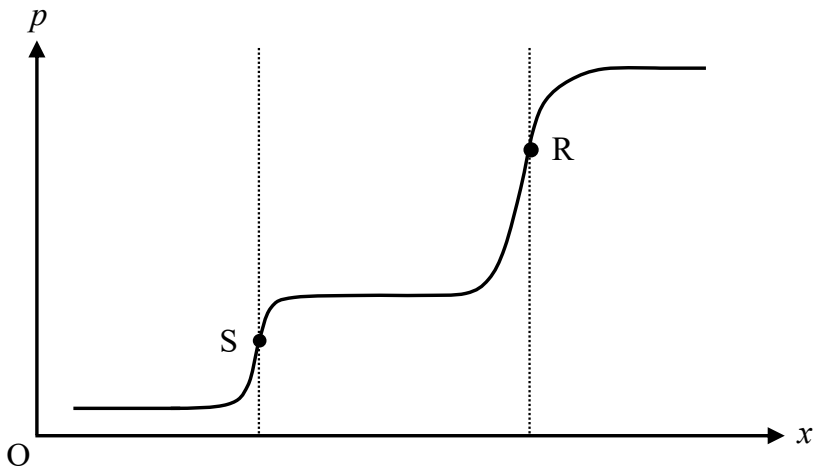


Figure 1.3: Typical wall pressure distribution for a well-separated compression ramp flow. S and R denote the separation and reattachment position, respectively.

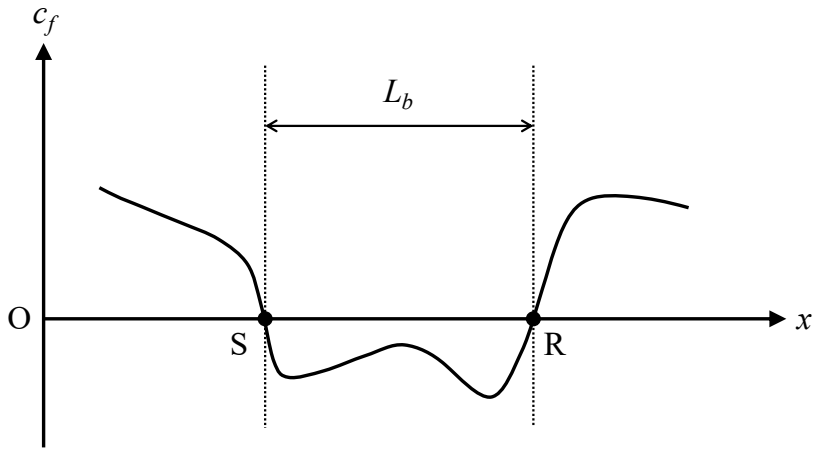


Figure 1.4: Typical skin friction coefficient distribution for a well-separated compression ramp flow. S and R denote the separation and reattachment position, respectively.

1.2.2 Influencing parameters

The main parameters influencing the SWBLI on a compression ramp are free-stream Mach number, free-stream Reynolds number, ramp angle as well as wall and total temperatures. In general, the separation bubble length increases with increasing ramp angle, Reynolds number and wall temperature, and with decreasing Mach number and total temperature. A brief explanation for these effects is given in the following.

In a laminar interaction, as aforementioned, an increase in unit Reynolds number results in a decrease in shear forces, causing a reducing resistance of the boundary layer to the adverse pressure gradient. The consequence is an increase in the separation bubble length. Increasing ramp angle simply leads to a stronger ramp shock and thus a higher adverse pressure gradient. As a result, the separation bubble length rises. A variation in Mach number changes the shock strength and the boundary layer profile simultaneously. The overall effect is that the separation bubble length decreases as the Mach number is increased. But this effect is modest especially in the hypersonic regime [2].

Experiments performed for a hypersonic compression ramp flow showed that wall cooling leads to a reduction in the separation bubble length compared to the adiabatic case [10]. This was experimentally confirmed by the observed increase in the separation bubble length on a heated compression ramp model [11]. When the wall temperature is decreased, the sonic-point location in the boundary layer profile moves towards the wall, resulting in a thinner subsonic region. At the same time, the density is greater, which corresponds to an increased momentum. Therefore, the overall effect of wall cooling is to make the boundary layer more resistant, which reduces the separation bubble length. Increasing total temperature for a fixed wall temperature is equivalent to wall cooling because the

wall-to-stagnation temperature ratio decreases. High temperature real gas effects are not considered in this context.

1.3 Streamwise vortices in SWBLI

In SWBLI, three-dimensionality is frequently observed even for nominally two-dimensional configurations (e.g. cases a and b in figure 1.1). The three-dimensionality usually manifests itself in streamwise streaks which are associated with streamwise vortices [4, 12]. The presence of the vortices complicates the heat transfer on the surface and promotes the transition from laminar to turbulent flow.

1.3.1 Streamwise heat flux streaks

Figure 1.5 shows the experimentally observed surface heat flux streaks in hypersonic compression ramp flows visualised by infrared imaging and temperature-sensitive paint techniques. The presence of streamwise streaks modifies the spatial distribution of the heat transfer, giving rise to local and global enhancements of surface heating. For instance, the spanwise heat flux variation with respect to the averaged value was obtained up to 30% by Chuvakhov et al. [13], 35% by Luca et al. [14], 50% by Simeonides and Haase [15], etc. In addition, the streak pattern is usually nonuniform in spanwise direction. In other words, the wavelength of the streaks (the spanwise distance between two adjacent streaks) varies slightly in spanwise direction. It is further noted that the general wavelength exhibits parametric dependent variations. Luca et al. [14] revealed that the wavelength decreases with increasing unit Reynolds number and ramp angle. While in the experiments of Roghelia et al. [16], the wavelength is more or less insensitive to the studied ramp angles. Furthermore, the leading edge bluntness of the flat plate also has a great influence on the wavelength [13, 17]. From an engineering point of view, these facts point to a challenge for the thermal protection system of a flight vehicle.

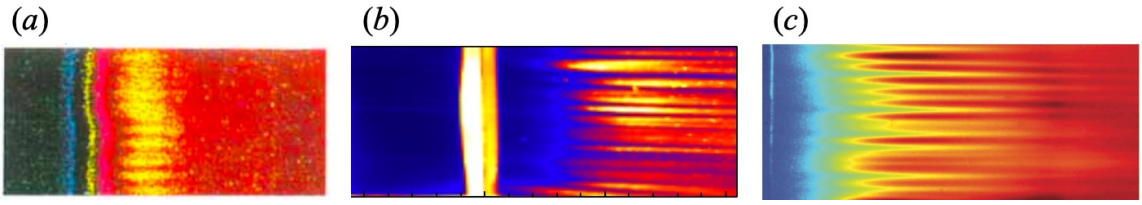


Figure 1.5: Surface heat flux streaks observed on compression ramps in different experiments: (a) Simeonides and Haase [15], (b) Roghelia et al. [16], (c) Chuvakhov et al. [13]. Flow from left to right.

The presence of the streamwise streaks is not limited to compression ramps [4]. For instance, they were also observed on the hollow cylinder flare [18], double cone [19],

double wedge [20] and oblique shock-wave/boundary-layer interaction [21]. The physical mechanisms responsible for the formation and evolution of the streaks and the associated vortices are still not well understood. Some possible mechanisms affecting the formation and behaviour of the streaks are summarised in the following.

1.3.2 Görtler vortices

Fundamentally, Görtler instability occurs in boundary layers over concave walls due to the action of centrifugal forces [22, 23]. The instability manifests itself in the form of streamwise-oriented, counter-rotating vortices, which is referred to as Görtler vortices (see figure 1.6). The formation of Görtler vortices is accompanied by energetic streamwise high- and low-momentum streaks caused by the vertical displacement of fluid by the vortices. As a result, a lateral variation of heat flux occurs on the surface which is similar to the pattern shown in figure 1.5. For the case of a compression ramp flow, the highly curved streamlines formed around the reattachment point (see figure 1.2) enable the appearance of centrifugal instability. Therefore, the experimentally or numerically observed heat flux striation phenomenon has been often attributed to the formation of Görtler vortices supported by the concave flow curvature in the reattaching flow regions [14–17, 24, 25], see figure 1.7 for example.

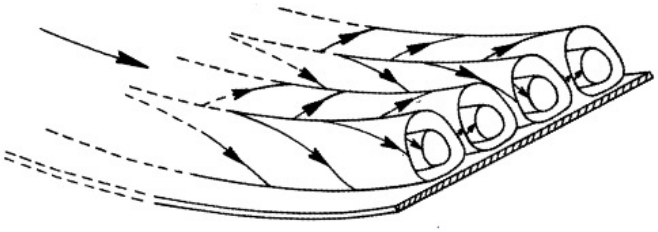


Figure 1.6: Sketch of Görtler vortices [26].

Görtler vortices have been observed not only in laminar flow, but also in transitional and turbulent SWBLI [18, 27–32]. Loginov et al. [27] performed numerical simulations and showed the presence of streamwise vortices in the mean flow visualised by oil flow technique. Zhuang et al. [33] experimentally analysed the instantaneous structures of a turbulent compression ramp flow and found that streamwise Görtler-like vortices are present both inside and downstream of the separation bubble. Recent numerical simulations performed by Priebe and Martín [6] and Pasquariello et al. [32] showed the footprints of Görtler-like vortices in compression ramp flow and oblique SWBLI, respectively. Those researchers calculated the Görtler number for a turbulent boundary layer and found a sufficiently large value supporting the presence of Görtler vortices.

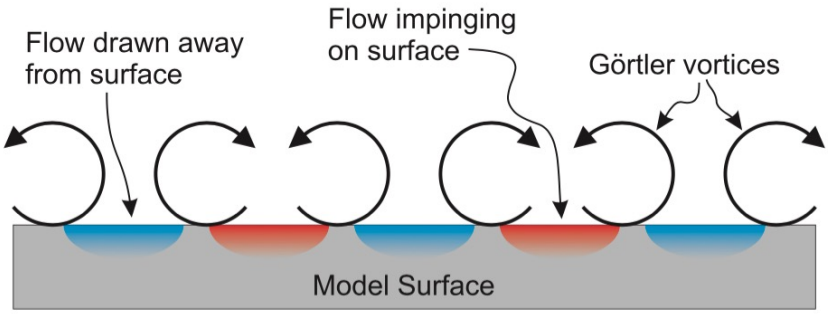


Figure 1.7: Mechanism for the formation of streamwise streaks due to Görtler vortices, adopted from Yang et al. [20] and Ishiguro et al. [25].

The Görtler number was originally defined by Görtler [26] for the case of laminar boundary layers on a concave wall:

$$G = Re_{\infty,\delta_2}\sqrt{\frac{\delta_2}{R}}, \tag{1.3}$$

where Re_{∞,δ_2} is the free-stream Reynolds number based on the momentum thickness δ_2, and R denotes the radius of curvature of the wall. For a turbulent compression ramp flow, the Görtler number can be estimated as [27, 34]

$$G_T = \frac{\delta_2}{0.018\delta_1}\sqrt{\frac{\delta_2}{R}}, \tag{1.4}$$

where R is the radius of curvature of the mean-flow streamlines within the boundary layer close to the ramp corner, δ_2 is the momentum thickness and δ_1 the displacement thickness at the compression corner.

On the other hand, several researchers proposed different ways to determine the Görtler number for a laminar compression ramp flow [16, 24, 35–37]. However, there is a discrepancy in the formulation of Görtler number in these papers. Particularly, the determination of boundary-layer thickness and the definition of radius of curvature were inconsistent. Determining the streamline curvature in a laminar compression ramp flow is challenging due to the presence of a large separation bubble. Grasso and Marini [35] calculated the radius of the circle tangent to the computed separation and reattachment points, as shown in figure 1.8(a). Alternatively, Navarro-Martinez and Tutty [24] estimated the radius from the circle tangent to the surface at reattachment and to the flat plate surface (figure 1.8(b)). Both methods yield an overestimation of the radius of curvature because, in reality, the radius of curvature is smaller at reattachment. Based on the numerical simulation results, Balakumar et al. [36] and Cao et al. [38] suggested calculating the exact value of the curvature radius along a single streamline in the reattaching shear layer. As

this method is not applicable to experimental data, Roghelia et al. [16] proposed simply measuring the curvature from high-resolution schlieren images (see figure 1.8(c)). In the present thesis, two methods of determining the radius of curvature near reattachment are proposed to estimate the Görtler number for a laminar separated compression ramp flow as accurately as possible.

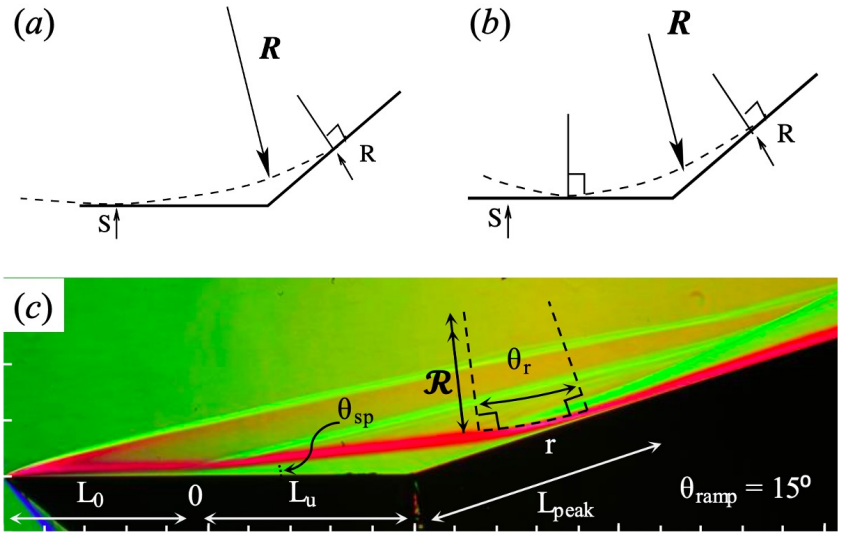


Figure 1.8: Determination of the radius of curvature for the concave shear layer in a compression ramp flow proposed by (a) Grasso and Marini [35], (b) Navarro-Martinez and Tutty [24] and (c) Roghelia et al. [16].

1.3.3 Global instability of SWBLI

Global stability analysis (GSA) of laminar separation bubbles has seen great progress in recent years [39, 40]. GSA considers the linear stability of small-amplitude perturbations superposed on a steady base flow without assumptions on the spatial variation of the base flow and the directionality of perturbation waves [40, 41]. This makes GSA suitable for studying the stability of flows with separation [42–44]. Therefore, more attention is turned to the instabilities in laminar SWLBI and their connection to the streamwise streaks. Hildebrand et al. [45] investigated the flow instability of a recirculation bubble created by an oblique shock wave impinging on a Mach 5.92 laminar flat plate boundary layer. It was found that the most unstable global mode drives the formation of long streamwise streaks downstream of the separation bubble, and the corrugation in the impinging shock foot was found to play a role in the physical mechanism sustaining the three-dimensional instability. Sidharth et al. [44] investigated the onset of three-dimensionality in a Mach 5 slender-double-wedge flow over an adiabatic wall and found a stationary unstable mode associated with streamwise streaks in wall temperature downstream of the corner. It was further shown that streamwise deceleration of the recirculating flow plays a dominant role

in the three-dimensional instability. These findings point to an intrinsic instability lying in the separation bubble, which contributes to the formation of downstream streaks. A significant contribution of the separation bubble flow to the wavelength selection mechanism of the streamwise streaks was also demonstrated by Dwivedi et al. [46].

It is known that beyond a critical condition (e.g., a critical ramp angle), a two-dimensional separation bubble flow bifurcates to a three-dimensional one due to global instabilities [44, 45, 47]. For instance, Sidharth et al. [44] found that by increasing the turning angle of the second compression ramp for a double wedge configuration, the two-dimensional flow destabilises to three-dimensional perturbations at a critical angle, which results in the growth of spanwise periodic flow structures, as shown in figure 1.9. A similar situation can take place in an oblique SWBLI [45], backward-facing step [48], open cavity flows [49], etc. By further increasing the turn angle beyond the bifurcation, Sidharth et al. [44] found a family of global unstable modes including an oscillatory one. This mode exhibits streamwise periodicity in the separation bubble. Several unsteady modes were also revealed for a compression ramp flow over a heated wall [50]. These results indicate the presence of flow unsteadiness for a base flow far beyond the bifurcation point.

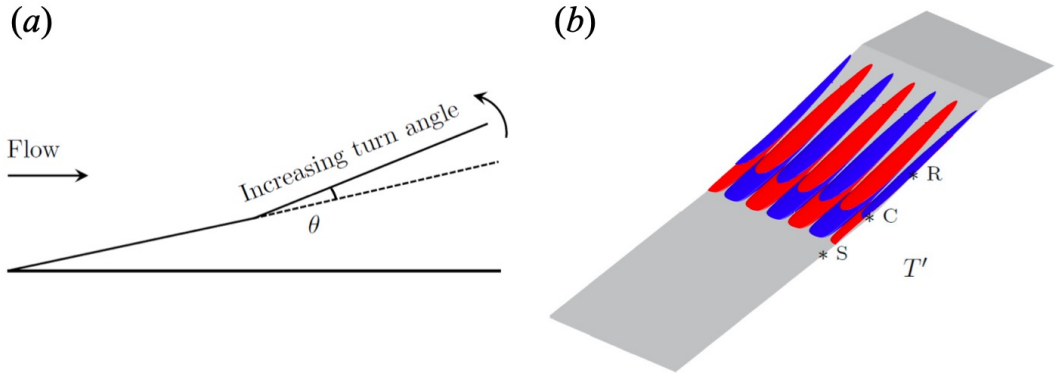


Figure 1.9: (a) Schematic showing the variation of the turn angle for a double wedge flow. (b) Shape of the unstable mode at the critical angle. Both figures are adopted from the study of Sidharth et al. [44].

It is noted that in the aforementioned global stability analysis, external perturbations originating upstream of the separation bubble are absent. It means that streamwise streaks can occur in the absence of external disturbances. However, in high-speed experimental facilities, it is hard to exclude environmental disturbances. In other words, separating the effects of external disturbances from that of the intrinsic instability is challenging in experiments. In fact, when the two-dimensional base flow is stable (e.g., the turning angle in figure 1.9(a) is below the critical value), the experimentally observed streamwise streaks can be a consequence of the amplification of upstream disturbances via other mechanisms (e.g., centrifugal instability, transient growth). As direct numerical simulation (DNS) has the advantage of creating a nearly disturbance-free environment, one can use DNS to study a naturally generated three-dimensional flow and the intrinsic instability of the fluid

dynamic system, which serves as an objective the present thesis. It also facilitates the explanation of the physical mechanism underlying the experimentally observed streamwise streaks.

1.3.4 Baroclinic effects

In a recent paper, Zapryagaev et al. [51] suggested another mechanism for the generation of the streamwise vortices. The vorticity transport equation is

$$\frac{\partial \boldsymbol{\omega}}{\partial t} + (\boldsymbol{u} \cdot \nabla)\boldsymbol{\omega} = (\boldsymbol{\omega} \cdot \nabla)\boldsymbol{u} - \boldsymbol{\omega}(\nabla \cdot \boldsymbol{u}) + \frac{1}{\rho^2}\nabla\rho \times \nabla p + \nabla \times (\frac{\nabla \cdot \tau}{\rho}). \tag{1.5}$$

Here, $\boldsymbol{\omega}$ is the vorticity vector; $\boldsymbol{u}$ is the velocity vector; τ is the viscous stress tensor. This equation includes a term $\nabla\rho \times \nabla p$ representing the baroclinic effect, which arises from the misalignment of pressure and density gradients. A schematic sketch of the baroclinic effects is presented in figure 1.10. In the compression ramp flow, a considerable density gradient occurs in the boundary layer and the free shear layer above the separation bubble, and its direction is normal to the wall in most regions. Meanwhile, any spanwise pressure perturbations, for instance, introduced by free-stream turbulence, could lead to pressure gradients in the z-direction. As a result, the baroclinic torque constructed by the density and pressure gradients produces a streamwise component of the vorticity vector ω_l, which is aligned in streamwise direction l. This circumstance promotes the formation of streamwise vortices in the separated and reattached flow regions. Using an input-output analysis, Dwivedi et al. [46] were able to analyse the formation of streamwise streaks as a result of the amplification of external disturbances in a compression ramp flow. It was shown that baroclinic effects arising from the interactions of base-flow density gradients with spanwise gradients of pressure perturbations play a dominant role in triggering the streamwise streaks on the ramp surface. Therefore, baroclinic effects and centrifugal effects are two potential mechanisms that can amplify upstream disturbances, leading to vortical structures [51].

1.3.5 Influence of leading-edge geometry

Some early studies proposed leading-edge imperfections as a source of disturbances which are amplified downstream, forming the streamwise vortices [14, 52]. However, Matsumura et al. [53] and Roghelia et al. [16] demonstrated the presence of heat flux streaks on the compression ramps with a well-prepared sharp leading edge. Additionally, Roghelia et al. [17] reported an almost identical wavelength on the compression ramps at two facilities for similar flow conditions and model configurations. This suggests that external disturbances (for example, induced by leading-edge imperfections, free-stream turbulence and surface roughness) can be an excitation but cannot explain the matching streaks observed in

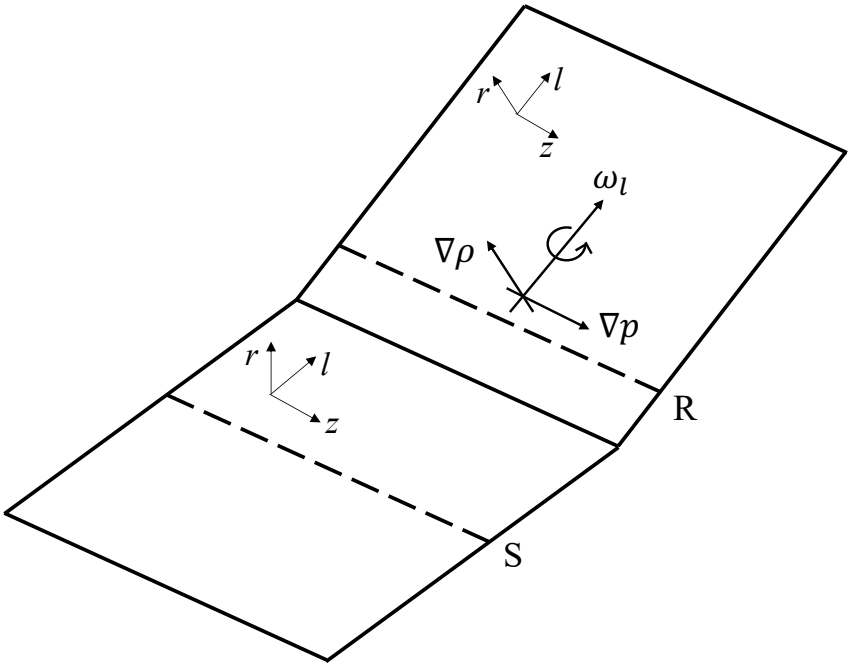


Figure 1.10: Mechanism for the formation of streamwise vortices due to baroclinic effects, adapted from Zapryagaev et al. [51].

different facilities. From a numerical point of view, the numerically constructed physical model possesses an exactly sharp leading edge, which can exclude the influence of leading-edge imperfections. Several numerical studies [24, 37, 54–56] showed the occurrence of streamwise vortices and streaks for compression ramp flows with an exactly sharp leading edge.

On the other hand, a deterministic influence of a sufficiently strong artificial forcing at the leading edge on the formation of streamwise streaks has been observed experimentally [14, 57–59]. It was shown that a specific wavelength of the streaks can be forced by introducing a leading-edge geometry with the preferential length scale [58, 59]. This serves as a flow control criterion for a compression ramp flow. Moreover, the formation and behaviour of the streamwise streaks were shown to be highly sensitive to the leading-edge bluntness [13, 17, 60]. Chuvakhov et al. [13] found that both the maximum Stanton numbers in the reattachment region and the amplitude of spanwise variation of the Stanton number induced by streamwise vortices decrease significantly in the case of a small leading-edge bluntness. Roghelia et al. [17] showed that for a sufficiently large radius of the leading edge, streamwise streaks disappear on the compression ramp. In summary, at present it is not clear which lengthscale of a leading-edge imperfection depending on the flow conditions is necessary to have a significant influence on the development of streamwise vortices.

1.4 Low-frequency unsteadiness in SWBLI

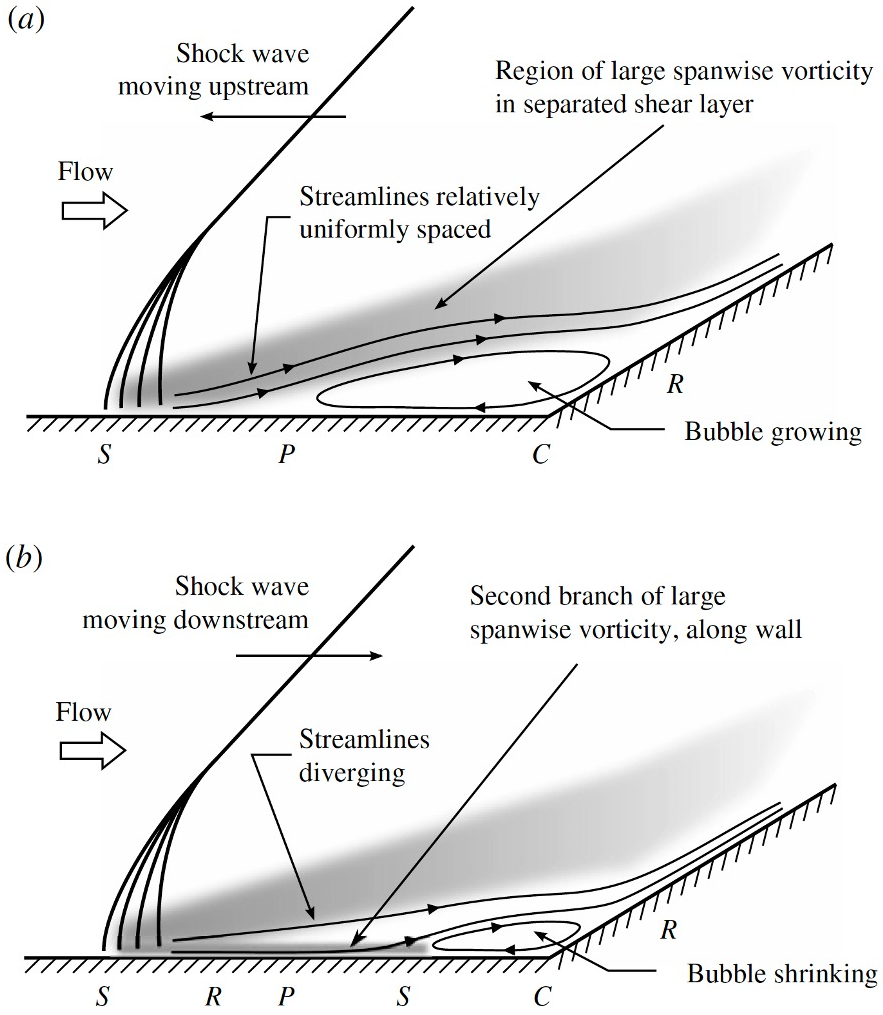


Figure 1.11: Schematics of the flow structure for the low-frequency dynamics in a turbulent compression ramp flow, adapted from Priebe and Martín [6].

Flow unsteadiness is typical of turbulent flows. A main research focus in turbulent SWBLI is the low-frequency large-scale shock oscillation associated with the pulsation of the separated flow [1, 3, 5, 6]. As shown in figure 1.11, the growth of the bubble is associated with the shock moving upstream, whereas the shrinking of the bubble is associated with the shock moving downstream [6]. Concerning the physical mechanisms responsible for the low-frequency unsteadiness, a wealth of past and recent results suggests that the unsteadiness is driven either by fluctuations in the upstream turbulent boundary layer or by some large-scale instabilities intrinsic to the downstream separated flow [5]. The relevant importance of the two mechanisms depends on the strength of the interaction. A combined mechanism dominates for weakly separated flows, while for strong separations, the dominant driving mechanism is the inherent instability in the separated flow. It was

shown that in strong interactions, the separation bubble pulsates in response to a global instability that leads to flapping of the reattachment point [5, 61].

As aforementioned, global unstable modes – both stationary and oscillatory – will occur in laminar separated flows when the value of a critical parameter (e.g. the ramp angle) is far beyond the bifurcation point [44, 50]. Therefore, the presence of global instabilities for a flow with strong separation is irrespective of the state of incoming boundary layer. In this view, the investigation of the global instability in laminar separated flows could provide insights into the flow dynamics in turbulent SWBLI [61] too.

In addition to the upstream and downstream mechanisms discussed above, evidence for the existence of unsteady streamwise Görtler-like vortices was also uncovered in turbulent SWBLI [27, 30, 32]. Priebe et al. [30] and Pasquariello et al. [32] decomposed their numerical data and identified instantaneous footprints of unsteady streamwise vortices for compression ramp and impinging shock cases, respectively. They also showed that their unsteadiness is linked to the shock oscillation and the large-scale flapping of the reattachment line. Therefore, Pasquariello et al. [32] argued that the streamwise vortices inside the separation bubble might be seen as a continuous forcing for the low-frequency unsteadiness for a strong turbulent SWBLI.

The investigation of the unsteadiness and its coupling with the streamwise vortices in laminar SWBLI is scarce. Zapryagaev et al. [51] and Kavun et al. [62] analysed the wall pressure fluctuations in the reattachment region for a compression ramp flow at Mach number 6 and revealed a maximum in the spectra of pressure fluctuations. This peak had a Strouhal number of 0.64 and was interpreted by the longitudinal pulsation of the reattachment position [62]. In general, the coupling of the streamwise streaks with the flow unsteadiness in turbulent SWBLI may also be present in laminar SWBLI if oscillatory unstable modes are present in the separation bubble. This is clearly demonstrated in Chapter 5 of the present thesis.

1.5 Objectives and outline

The main objective of the present thesis is to complement the experimental campaign carried out in the hypersonic Aachen Shock Tunnel TH2 at the Shock Wave Laboratory of RWTH Aachen University and detail the physics beneath the experimentally observed phenomena by using direct numerical simulation. The present thesis examines the contribution of separation bubble instability and centrifugal effects to the formation, evolution and unsteadiness of the streamwise vortices and streaks. Numerical simulations are firstly performed to reveal the presence of streamwise vortices in the absence of external disturbances. As a disturbance-amplifier, the centrifugal instability may always be at work whether the disturbances are generated externally or internally. Therefore, it is necessary to accurately determine the Görtler number where the streamline curvature is

considerable, which serves as another task of the present thesis. The detailed objectives are listed as follows.

- The first aim is to setup a numerical methodology appropriate for simulating the experiments and reproducing the experimentally observed phenomena, in an attempt to achieve a good agreement between the numerical and experimental results.
- The second aim is to investigate the contribution of the separation bubble flow to the formation and evolution of streamwise vortices and streaks with an emphasis on the influence on flow unsteadiness.
- The third aim is to build a simple physical model for the determination of the Görtler number for a laminar separated compression ramp flow.

The present thesis is organised as follows. In Chapter 2, a detailed description of the numerical methodology is given, including the governing equations, the numerical schemes applied to DNS, the boundary and initial conditions, etc. In Chapter 3, a comprehensive mesh study is presented to show the grid independence of the considered flow. Meanwhile, comparisons of DNS results with experimental data and theoretical predictions are provided. Additionally, the finite-span effects of the compression ramp configuration on the flow properties are briefly discussed. The basic characteristics of the streamwise vortices and streaks are analysed in Chapter 4 accompanied by showing the influence of free-stream Reynolds number and ramp angle. Additional effort is put into the three-dimensional flow reattachment. Chapter 5 presents the unsteady effects for two hypersonic compression ramp flows. The unsteady features of streamwise heat flux streaks are investigated. Dynamic mode decomposition (DMD) is utilised to identify the instabilities in the separation bubble flow. In Chapter 6, methods of determining the Görtler number are proposed and verified. Variations of the Görtler number with governing flow parameters and ramp angle are also studied. Conclusions are given in Chapter 7, where some ideas for future work are mentioned.

2 Numerical methodology

Direct numerical simulations with robust shock-capturing feature are applied to study the hypersonic compression ramp flow problem. This chapter introduces the governing equations, discretisation methods, initial and boundary conditions as well as the implementation of numerical simulations.

2.1 Governing equations

The three-dimensional Navier-Stokes equations for unsteady, compressible flow are considered in curvilinear coordinates in conservative nondimensional form [63, 64]:

$$\frac{\partial U}{\partial \bar{t}} + \frac{\partial F}{\partial \xi} + \frac{\partial G}{\partial \eta} + \frac{\partial H}{\partial \zeta} = \frac{\partial F^{\nu}}{\partial \xi} + \frac{\partial G^{\nu}}{\partial \eta} + \frac{\partial H^{\nu}}{\partial \zeta}. \tag{2.1}$$

Here, U is the solution vector, F, G and H are the inviscid fluxes, and F^{ν}, G^{ν} and H^{ν} denote the viscous fluxes. They are given by

$$U = J \begin{pmatrix} \bar{\rho} \\ \bar{\rho}\bar{u} \\ \bar{\rho}\bar{v} \\ \bar{\rho}\bar{w} \\ \bar{\rho}\bar{e} \end{pmatrix}, \tag{2.2}$$

$$F = J \begin{pmatrix} \bar{\rho}\bar{\theta}_1 \\ \bar{\rho}\bar{\theta}_1\bar{u} + \xi_x\bar{p}\Upsilon \\ \bar{\rho}\bar{\theta}_1\bar{v} + \xi_y\bar{p}\Upsilon \\ \bar{\rho}\bar{\theta}_1\bar{w} + \xi_z\bar{p}\Upsilon \\ \bar{\rho}\bar{\theta}_1(\bar{e} + \frac{\bar{p}}{\bar{\rho}}\Upsilon) \end{pmatrix}, G = J \begin{pmatrix} \bar{\rho}\bar{\theta}_2 \\ \bar{\rho}\bar{\theta}_2\bar{u} + \eta_x\bar{p}\Upsilon \\ \bar{\rho}\bar{\theta}_2\bar{v} + \eta_y\bar{p}\Upsilon \\ \bar{\rho}\bar{\theta}_2\bar{w} + \eta_z\bar{p}\Upsilon \\ \bar{\rho}\bar{\theta}_2(\bar{e} + \frac{\bar{p}}{\bar{\rho}}\Upsilon) \end{pmatrix}, H = J \begin{pmatrix} \bar{\rho}\bar{\theta}_3 \\ \bar{\rho}\bar{\theta}_3\bar{u} + \zeta_x\bar{p}\Upsilon \\ \bar{\rho}\bar{\theta}_3\bar{v} + \zeta_y\bar{p}\Upsilon \\ \bar{\rho}\bar{\theta}_3\bar{w} + \zeta_z\bar{p}\Upsilon \\ \bar{\rho}\bar{\theta}_3(\bar{e} + \frac{\bar{p}}{\bar{\rho}}\Upsilon) \end{pmatrix}, \tag{2.3}$$

$$
F^{\nu} = J \begin{pmatrix} 0 \\ \Psi(\xi_x\bar{\tau}_{\xi\xi} + \xi_y\bar{\tau}_{\xi\eta} + \xi_z\bar{\tau}_{\xi\zeta}) \\ \Psi(\xi_x\bar{\tau}_{\eta\xi} + \xi_y\bar{\tau}_{\eta\eta} + \xi_z\bar{\tau}_{\eta\zeta}) \\ \Psi(\xi_x\bar{\tau}_{\zeta\xi} + \xi_y\bar{\tau}_{\zeta\eta} + \xi_z\bar{\tau}_{\zeta\zeta}) \\ \Psi(\bar{u}(\xi_x\bar{\tau}_{\xi\xi} + \xi_y\bar{\tau}_{\xi\eta} + \xi_z\bar{\tau}_{\xi\zeta}) \\ +\bar{v}(\xi_x\bar{\tau}_{\eta\xi} + \xi_y\bar{\tau}_{\eta\eta} + \xi_z\bar{\tau}_{\eta\zeta}) \\ +\bar{w}(\xi_x\bar{\tau}_{\zeta\xi} + \xi_y\bar{\tau}_{\zeta\eta} + \xi_z\bar{\tau}_{\zeta\zeta})) \\ -\Gamma(\xi_x\bar{q}_{\xi} + \xi_y\bar{q}_{\eta} + \xi_z\bar{q}_{\zeta}) \end{pmatrix}, G^{\nu} = J \begin{pmatrix} 0 \\ \Psi(\eta_x\bar{\tau}_{\xi\xi} + \eta_y\bar{\tau}_{\xi\eta} + \eta_z\bar{\tau}_{\xi\zeta}) \\ \Psi(\eta_x\bar{\tau}_{\eta\xi} + \eta_y\bar{\tau}_{\eta\eta} + \eta_z\bar{\tau}_{\eta\zeta}) \\ \Psi(\eta_x\bar{\tau}_{\zeta\xi} + \eta_y\bar{\tau}_{\zeta\eta} + \eta_z\bar{\tau}_{\zeta\zeta}) \\ \Psi(\bar{u}(\eta_x\bar{\tau}_{\xi\xi} + \eta_y\bar{\tau}_{\xi\eta} + \eta_z\bar{\tau}_{\xi\zeta}) \\ +\bar{v}(\eta_x\bar{\tau}_{\eta\xi} + \eta_y\bar{\tau}_{\eta\eta} + \eta_z\bar{\tau}_{\eta\zeta}) \\ +\bar{w}(\eta_x\bar{\tau}_{\zeta\xi} + \eta_y\bar{\tau}_{\zeta\eta} + \eta_z\bar{\tau}_{\zeta\zeta})) \\ -\Gamma(\eta_x\bar{q}_{\xi} + \eta_y\bar{q}_{\eta} + \eta_z\bar{q}_{\zeta}) \end{pmatrix},
$$

$$
H^{\nu} = J \begin{pmatrix} 0 \\ \Psi(\zeta_x\bar{\tau}_{\xi\xi} + \zeta_y\bar{\tau}_{\xi\eta} + \zeta_z\bar{\tau}_{\xi\zeta}) \\ \Psi(\zeta_x\bar{\tau}_{\eta\xi} + \zeta_y\bar{\tau}_{\eta\eta} + \zeta_z\bar{\tau}_{\eta\zeta}) \\ \Psi(\zeta_x\bar{\tau}_{\zeta\xi} + \zeta_y\bar{\tau}_{\zeta\eta} + \zeta_z\bar{\tau}_{\zeta\zeta}) \\ \Psi(\bar{u}(\zeta_x\bar{\tau}_{\xi\xi} + \zeta_y\bar{\tau}_{\xi\eta} + \zeta_z\bar{\tau}_{\xi\zeta}) \\ +\bar{v}(\zeta_x\bar{\tau}_{\eta\xi} + \zeta_y\bar{\tau}_{\eta\eta} + \zeta_z\bar{\tau}_{\eta\zeta}) \\ +\bar{w}(\zeta_x\bar{\tau}_{\zeta\xi} + \zeta_y\bar{\tau}_{\zeta\eta} + \zeta_z\bar{\tau}_{\zeta\zeta})) \\ -\Gamma(\zeta_x\bar{q}_{\xi} + \zeta_y\bar{q}_{\eta} + \zeta_z\bar{q}_{\zeta}) \end{pmatrix}, \tag{2.4}
$$

where

$$
\begin{aligned}
\bar{\theta}_1 &= \bar{u}\xi_x + \bar{v}\xi_y + \bar{w}\xi_z, \\
\bar{\theta}_2 &= \bar{u}\eta_x + \bar{v}\eta_y + \bar{w}\eta_z, \\
\bar{\theta}_3 &= \bar{u}\zeta_x + \bar{v}\zeta_y + \bar{w}\zeta_z, \\
\Upsilon = \frac{1}{\gamma M_{\infty}^2}, \Psi &= \frac{1}{Re_{\infty,L}}, \Gamma = \frac{1}{(\gamma-1)M_{\infty}^2 Pr},
\end{aligned} \tag{2.5}
$$

$\xi_{x,y,z}$, $\eta_{x,y,z}$, $\zeta_{x,y,z}$ are the metric coefficients and J is the determinant of the Jacobian matrix of the transformation of the Cartesian coordinates x, y and z into the curvilinear coordinates $\xi(x,y,z)$, $\eta(x,y,z)$ and $\zeta(x,y,z)$. Here, the coordinates are nondimensional parameters. $\bar{\tau}$ and $\bar{q}$ are the transformed shear stress tensor and heat flux vector, respectively. The total energy $\bar{e}$ is defined as

$$
\bar{e} = \frac{\bar{u}^2 + \bar{v}^2 + \bar{w}^2}{2} + \frac{\Upsilon}{\gamma - 1}\frac{\bar{p}}{\bar{\rho}}. \tag{2.6}
$$

The system of equations is closed by the perfect gas law relating the density $\bar{\rho}$, the pressure $\bar{p}$ and the temperature $\bar{T}$:

$$\bar{p} = \bar{\rho}\bar{T}. \tag{2.7}$$

Sutherland's law is used to determine the viscosity $\bar{\mu}$:

$$\bar{\mu} = \frac{1+\bar{S}}{\bar{T}+\bar{S}}\bar{T}^{3/2}, \bar{S} = \frac{110.4\text{K}}{T_\infty}. \tag{2.8}$$

The ratio of specific heats γ and the Prandtl number Pr used in the simulation are 1.4 and 0.71, respectively. The nondimensional variables are normalised using the free-stream parameters:

$$\bar{\rho} = \frac{\rho}{\rho_\infty}, \bar{u} = \frac{u}{u_\infty}, \bar{v} = \frac{v}{u_\infty}, \bar{w} = \frac{w}{u_\infty}, \bar{p} = \frac{p}{p_\infty}, \bar{e} = \frac{e}{u_\infty^2}, \bar{T} = \frac{T}{T_\infty}, \bar{\mu} = \frac{\mu}{\mu_\infty}. \tag{2.9}$$

The free-stream Mach number and Reynolds number are $M_\infty = u_\infty/a_\infty$ and $Re_{\infty,L} = \rho_\infty u_\infty L/\mu_\infty$, respectively. The flat plate length L is used as the reference length, and thus the nondimensional time is $\bar{t} = tu_\infty/L$.

2.2 Discretisation approaches

In terms of the numerical method applied for the hypersonic compression ramp flow problem, time integration is performed by an explicit third-order total variation diminishing (TVD) Runge-Kutta scheme. A weighted essentially non-oscillatory (WENO) finite difference scheme of fifth-order is applied for the discretization of the inviscid fluxes, based on the work of Jiang and Shu [65]. A sixth-order central difference scheme is used to approximate the viscous fluxes. The development of the in-house DNS solver has been carried out by the group of Professor Igor Klioutchnikov [63, 64, 66, 67] at the Shock Wave Laboratory of RWTH Aachen University. The DNS solver has been successfully applied for many shock-related physical problems (e.g., transonic airfoils [68–70]) and especially to study hypersonic compression ramp flows [38, 54, 71–73]. A detailed description of the numerical method is given in the following.

2.2.1 WENO scheme - inviscid terms

WENO schemes are widely used for spatial discretisation of hyperbolic conservation law equations. They are especially suited if discontinuities such as shock waves are expected in the solution [74]. In the present work, a fifth-order WENO scheme is applied to the discretisation of the inviscid fluxes. The scheme is explained in the following, exemplarily for the flux in the ξ-direction.

The derivative of the flux F at the mesh point i is defined as

$$\left(\frac{\partial F}{\partial \xi}\right)_i = \frac{F_{i+\frac{1}{2}} - F_{i-\frac{1}{2}}}{\Delta\xi} + \mathcal{O}\left(\Delta\xi^5\right), \tag{2.10}$$

where the cell boundary fluxes $F_{i+\frac{1}{2}}$ are

$$\begin{aligned} F_{i+\frac{1}{2}} &= \sum_{m=0}^{r-1} \omega_m M_m^r, \\ M_m^r &= \sum_{l=i+m-r+1}^{i+m} a_{m,l}^r F_l. \end{aligned} \tag{2.11}$$

Here, M_m^r is the m-th of r ($r = (N+1)/2 = 3$) sub-stencils with polynomial coefficients $a_{m,l}^r$ for a fifth-order approximation ($N = 5$) which are listed in Table 2.1.

Table 2.1: Coefficients $a_{m,l}^r$ for a fifth-order WENO scheme [65].

m	$l=0$	$l=1$	$l=2$
0	1/3	-7/6	11/6
1	-1/6	5/6	1/3
2	1/3	5/6	-1/6

The normalised nonlinear weights coefficient ω_m, defined as

$$\begin{aligned} \omega_m &= \frac{\bar{\omega}_m}{\bar{\omega}_0 + ... + \bar{\omega}_{r-1}}, \\ \bar{\omega}_m &= \frac{b_m^r}{(\epsilon + IS_m)^2}, \end{aligned} \tag{2.12}$$

preserves monotonicity in the vicinity of strong gradients by the means of the smoothness indicators IS_m. The parameter ϵ is added to avoid a division by zero for smooth solutions

and is set to $\epsilon \approx 10^{-13}$. The coefficients b_m^r are called optimal coefficients for the fifth-order of accuracy in smooth solution regions with $b_0^r = 1/10$, $b_1^r = 6/10$ and $b_2^r = 3/10$ [65].

In order to improve the numerical stability of the scheme, the propagation direction of the characteristics is taken into account resulting in a Lax-Friedrichs flux vector splitting:

$$F_i = F_i^+ + F_i^-, \tag{2.13}$$

where the algebraic sign of the eigenvalue λ of the flux Jacobian $A = \partial F/\partial U$ determines the propagation direction. The Jacobian matrix A can be transformed into the characteristic form $A = R\Lambda R^{-1}$ with the diagonal matrix of eigenvalues Λ, the right R and the left R^{-1} eigenvectors. The resulting fluxes take the form

$$F_i^{\pm} = \frac{1}{2}\left(F_i \pm \lambda_{max} U_i\right). \tag{2.14}$$

Due to the usage of the maximal eigenvalue λ_{max} within the stencil, it is called a local Lax-Friedrichs flux vector splitting. Finally, the inviscid flux given by Eq. (2.11) yields to [64]

$$\begin{aligned} F_{i+\frac{1}{2}} =& \frac{1}{12}[-F_{i-1} + 7F_i + 7F_{i+1} - F_{i+2}] + \\ & \sum_{s=1}^{5} \Big[-\Phi_N\left(R_s^{-1}\Delta F^+_{i-\frac{3}{2}}, R_s^{-1}\Delta F^+_{i-\frac{1}{2}}, R_s^{-1}\Delta F^+_{i+\frac{1}{2}}, R_s^{-1}\Delta F^+_{i+\frac{3}{2}}\right) \\ & + \Phi_N\left(R_s^{-1}\Delta F^-_{i+\frac{5}{2}}, R_s^{-1}\Delta F^-_{i+\frac{3}{2}}, R_s^{-1}\Delta F^-_{i+\frac{1}{2}}, R_s^{-1}\Delta F^-_{i-\frac{1}{2}}\right)\Big] R_s, \end{aligned} \tag{2.15}$$

with

$$\begin{aligned} \Delta F^{\pm}_{i+\frac{1}{2}} &= F^{\pm}_{i+1} - F^{\pm}_i, \\ \Phi_N(a,b,c,d) &= \frac{1}{3}\omega_0(a - 2b + c) + \frac{1}{6}\left(\omega_2 - \frac{1}{2}\right)(b - 2c + d), \end{aligned} \tag{2.16}$$

where the function Φ_N determines the non-linear corrections added to the central term depending on the weights shown in Eq. (2.12), the flux differences $\Delta F^{\pm}_{i+\frac{1}{2}}$ and the eigenvectors R_s and R_s^{-1} for the s-th component of the flux. Figure 2.1 demonstrates the sub-stencil configuration for the whole flux calculation including the Lax-Friedrichs flux vector splitting.

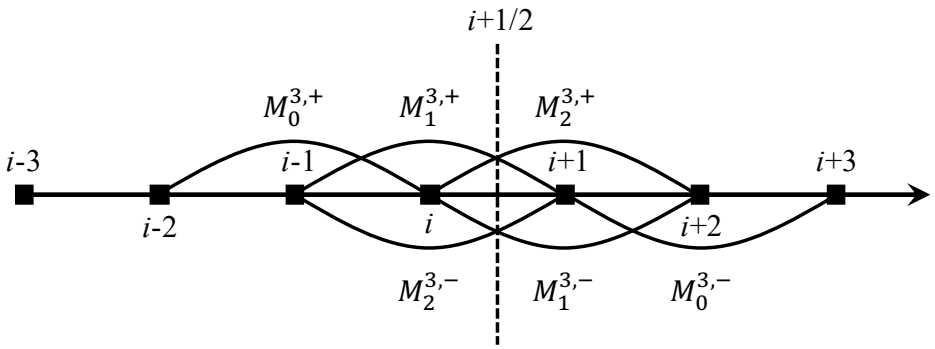


Figure 2.1: Schematic illustration of sub-stencils for the calculation of the cell boundary flux $F_{i+\frac{1}{2}}$ including the flux vector splitting.

2.2.2 Central difference scheme - viscous terms

The viscous fluxes F^ν, G^ν and H^ν are approximated by using a sixth-order central difference scheme [64]. The approximation of the derivatives is computed corresponding to the Taylor series. It is known that the partial derivatives of the viscous fluxes are all second-order partial derivatives. In general, taking the term $\frac{\partial F^\nu}{\partial \xi}$ for example, the resulting derivatives include the following two basic forms:

$$\text{Double derivative:} \quad \frac{\partial}{\partial \xi}\left(A\frac{\partial f}{\partial \xi}\right) = A\frac{\partial^2 f}{\partial \xi^2} + \frac{\partial A}{\partial \xi}\frac{\partial f}{\partial \xi}, \tag{2.17}$$

$$\begin{aligned} \text{Mixed derivative:} \quad & \frac{\partial}{\partial \xi}\left(A\frac{\partial f}{\partial \eta}\right) = A\frac{\partial^2 f}{\partial \xi \partial \eta} + \frac{\partial A}{\partial \xi}\frac{\partial f}{\partial \eta}, \\ \text{or} \quad & \frac{\partial}{\partial \xi}\left((Af)\frac{\partial f}{\partial \eta}\right) = (Af)\frac{\partial^2 f}{\partial \xi \partial \eta} + \frac{\partial (Af)}{\partial \xi}\frac{\partial f}{\partial \eta}. \end{aligned} \tag{2.18}$$

Here, A corresponds to the metric coefficients such as $\xi_x \cdot \eta_y$, and f represents the velocity components $(\bar{u}, \bar{v}, \bar{w})$ or temperature $(\bar{T})$. The approximation of the derivatives in the above equations is given in the following.

The first derivative is calculated as

$$\left(\frac{\partial f}{\partial \xi}\right)_{i,j} = \frac{f_{i+\frac{1}{2},j} - f_{i-\frac{1}{2},j}}{\Delta \xi} + \mathcal{O}\left(\Delta \xi^6\right), \tag{2.19}$$

where

$$f_{i+\frac{1}{2}} = C_{D,0}\left(f_{i+1} + f_i\right) + C_{D,1}\left(f_{i+2} + f_{i-1}\right) + C_{D,2}\left(f_{i+3} + f_{i-2}\right),$$
$$f_{i-\frac{1}{2}} = C_{D,0}\left(f_i + f_{i-1}\right) + C_{D,1}\left(f_{i+1} + f_{i-2}\right) + C_{D,2}\left(f_{i+2} + f_{i-3}\right), \tag{2.20}$$

with

$$C_{D,0} = \frac{37}{60}, C_{D,1} = -\frac{2}{15}, C_{D,2} = \frac{1}{60}. \tag{2.21}$$

Note that the terms $\frac{\partial f}{\partial \eta}$, $\frac{\partial A}{\partial \xi}$ and $\frac{\partial (Af)}{\partial \xi}$ take a similar form as $\frac{\partial f}{\partial \xi}$.

The double derivative is given by

$$\left(\frac{\partial^2 f}{\partial \xi^2}\right)_{i,j} = \frac{\left(\frac{\partial f}{\partial \xi}\right)_{i+\frac{1}{2},j} - \left(\frac{\partial f}{\partial \xi}\right)_{i-\frac{1}{2},j}}{\Delta \xi} + \mathcal{O}\left(\Delta \xi^6\right), \tag{2.22}$$

where

$$\left(\frac{\partial f}{\partial \xi}\right)_{i+\frac{1}{2},j} = \left[C_{P,0}\left(f_{i+1} - f_i\right) + C_{P,1}\left(f_{i+2} - f_{i-1}\right) + C_{P,2}\left(f_{i+3} - f_{i-2}\right)\right]\Delta \xi^{-1}, \tag{2.23}$$

$$\left(\frac{\partial f}{\partial \xi}\right)_{i-\frac{1}{2},j} = \left[C_{P,0}\left(f_i - f_{i-1}\right) + C_{P,1}\left(f_{i+1} - f_{i-2}\right) + C_{P,2}\left(f_{i+2} - f_{i-3}\right)\right]\Delta \xi^{-1}, \tag{2.24}$$

with

$$C_{P,0} = \frac{245}{180}, C_{P,1} = -\frac{25}{180}, C_{P,2} = \frac{1}{90}. \tag{2.25}$$

The mixed derivative is given by

$$\left(\frac{\partial^2 f}{\partial \xi \partial \eta}\right)_{i,j} = \frac{\left(\frac{\partial f}{\partial \eta}\right)_{i+\frac{1}{2},j} - \left(\frac{\partial f}{\partial \eta}\right)_{i-\frac{1}{2},j}}{\Delta \xi} + \mathcal{O}\left(\Delta \xi^6 + \Delta \eta^6\right), \tag{2.26}$$

where

$$\begin{aligned}\left(\frac{\partial f}{\partial \eta}\right)_{i+\frac{1}{2}} &= C_{D,0}\left(\left(\frac{\partial f}{\partial \eta}\right)_{i+1}+\left(\frac{\partial f}{\partial \eta}\right)_{i}\right)\\ &+ C_{D,1}\left(\left(\frac{\partial f}{\partial \eta}\right)_{i+2}+\left(\frac{\partial f}{\partial \eta}\right)_{i-1}\right)\\ &+ C_{D,2}\left(\left(\frac{\partial f}{\partial \eta}\right)_{i+3}+\left(\frac{\partial f}{\partial \eta}\right)_{i-2}\right),\end{aligned} \tag{2.27}$$

$$\begin{aligned}\left(\frac{\partial f}{\partial \eta}\right)_{i-\frac{1}{2}} &= C_{D,0}\left(\left(\frac{\partial f}{\partial \eta}\right)_{i}+\left(\frac{\partial f}{\partial \eta}\right)_{i-1}\right)\\ &+ C_{D,1}\left(\left(\frac{\partial f}{\partial \eta}\right)_{i+1}+\left(\frac{\partial f}{\partial \eta}\right)_{i-2}\right)\\ &+ C_{D,2}\left(\left(\frac{\partial f}{\partial \eta}\right)_{i+2}+\left(\frac{\partial f}{\partial \eta}\right)_{i-3}\right).\end{aligned} \tag{2.28}$$

The derivative $\left(\frac{\partial f}{\partial \eta}\right)_{i,j}$ is calculated as

$$\left(\frac{\partial f}{\partial \eta}\right)_{i,j} = \frac{f_{i,j+\frac{1}{2}} - f_{i,j-\frac{1}{2}}}{\Delta \eta} + \mathcal{O}\left(\Delta \eta^6\right), \tag{2.29}$$

where

$$\begin{aligned} f_{j+\frac{1}{2}} &= C_{D,0}\left(f_{j+1}+f_j\right) + C_{D,1}\left(f_{j+2}+f_{j-1}\right) + C_{D,2}\left(f_{j+3}+f_{j-2}\right),\\ f_{j-\frac{1}{2}} &= C_{D,0}\left(f_{j}+f_{j-1}\right) + C_{D,1}\left(f_{j+1}+f_{j-2}\right) + C_{D,2}\left(f_{j+2}+f_{j-3}\right).\end{aligned} \tag{2.30}$$

2.2.3 TVD Runge-Kutta scheme - temporal terms

For time integration an explicit third-order TVD Runge-Kutta scheme [75] is applied. Let

$$\frac{\partial U}{\partial \bar{t}} = Q, \tag{2.31}$$

with Q being the sum of the derivatives of the inviscid and viscous fluxes. Then, the general formula of the scheme is written as

$$U_a = U^n + \Delta \bar{t} Q\left(U^n\right), \tag{2.32}$$

$$U_b = \frac{3}{4}U^n + \frac{1}{4}U_a + \frac{1}{4}\Delta\bar{t}Q\left(U_a\right), \tag{2.33}$$

$$U^{n+1} = \frac{1}{3}U^n + \frac{2}{3}U_b + \frac{2}{3}\Delta\bar{t}Q\left(U_b\right). \tag{2.34}$$

The subscripts a and b denote two intermediate time stages between two consecutive time steps (from n to $n+1$) with the time interval being $\Delta\bar{t}$.

2.3 Boundary and initial conditions

Figure 2.2 shows a typical physical domain for solving the Navier-Stokes equations (Eq. (2.1)) exemplarily for a hypersonic compression ramp flow. The boundary conditions (BC) prescribed in the numerical simulation is also illustrated in the figure. On the flat plate and the following inclined ramp plate surface, the no-slip wall condition is applied. For the thermal condition on the wall, either isothermal or adiabatic conditions can be used, which are discussed later. An in-flow boundary condition is imposed at the inlet (the left surface), and an out-flow boundary condition at the outlet (the right surface). In spanwise direction, periodic boundary conditions are prescribed on both lateral surfaces. For the upper surface, the same in-flow boundary condition is utilised as for the inlet. The boundary conditions mentioned above must be physical in nature and need to be numerically implemented. In the following, a detailed description about how these boundary conditions are realised in the numerical simulation is presented.

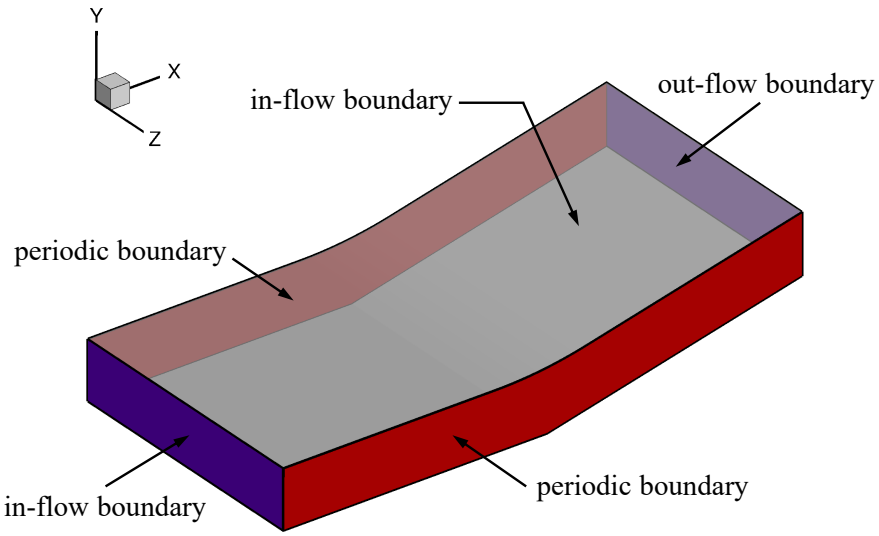


Figure 2.2: Physical domain with boundary conditions.

As aforementioned, the fifth-order WENO scheme and the sixth-order central difference scheme calculate the cell boundary flux and its derivative on the basis of the fluxes on six adjacent grid points. For instance, to calculate the flux at $i+\frac{1}{2}$, the fluxes at the points from $i-2$ to $i+3$ are required (see Fig. 2.1). Therefore, to define a boundary located at $i+\frac{1}{2}$ for the computational domain, three extra grid points have to be added outside the physical computational domain, which are named as ghost points composing the so-called ghost grid.

For the in-flow boundary condition, the free-stream values (for convenience, they are termed as q_∞) are set at all the ghost points:

$$f_{in} = q_\infty, f = \{\bar{u}, \bar{v}, \bar{w}, \bar{p}, \bar{\rho}\}, \tag{2.35}$$

where the subscript in denotes the in-flow boundary.

At the outlet, since the flow will be supersonic except for a very small region near the wall, the flow information virtually cannot propagate upstream. Therefore the values of the last three grid points in the computational domain are transferred to the ghost points to a simple zero-gradient condition at the boundary:

$$\left.\frac{\partial f}{\partial n}\right|_{out} = 0, f = \{\bar{u}, \bar{v}, \bar{w}, \bar{p}, \bar{\rho}\}, \tag{2.36}$$

where the subscript *out* denotes the out-flow boundary and n denotes the direction normal to the boundary. As illustrated in figure 2.3, the zero gradient is realised by assuming

$$\begin{aligned} f_g &= f_i; \\ f_{g+1} &= f_{i-1}; \\ f_{g+2} &= f_{i-2}. \end{aligned} \tag{2.37}$$

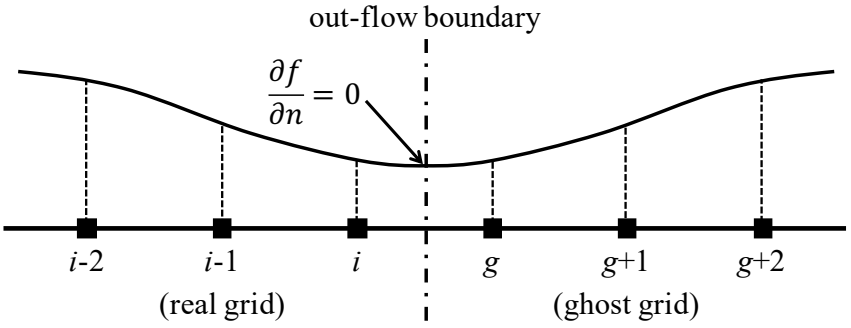


Figure 2.3: Schematic illustration for the out-flow boundary condition. f corresponds to density, velocity and pressure. n denotes the direction normal to the boundary.

Regarding the no-slip wall, the velocities are zero at the wall boundary:

$$\bar{u}|_{wall} = \bar{v}|_{wall} = \bar{w}|_{wall} = 0. \tag{2.38}$$

In terms of the wall thermal condition, two cases need to be separately considered. For an isothermal wall, a constant temperature must be set at the boundary: $\bar{T}_{wall} = \text{const}$. It is noted that the defined wall boundary is not located at the first real grid point but coincides with the symmetry plane between the first real and ghost grid point. To this end, one-sided differences [76] are employed to approximate the heat flux at the wall. In other words, the temperature gradient at the wall is approximated by using the temperature at the real grid points and the constant wall temperature.

For an adiabatic wall (i.e., there is no net heat flux across the wall), the thermal condition is given by

$$\left.\frac{\partial \bar{T}}{\partial n}\right|_{wall} = 0. \tag{2.39}$$

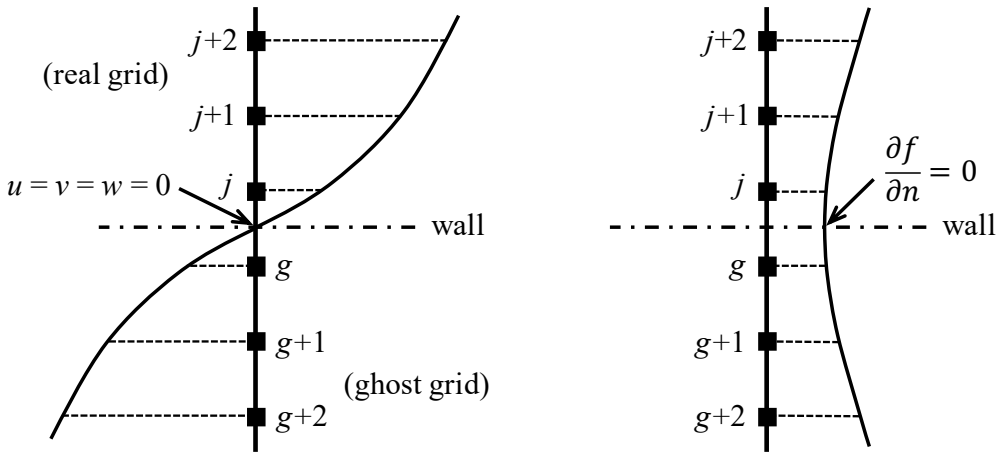


Figure 2.4: Schematic illustration for the wall boundary conditions. f corresponds to temperature (for an adiabatic wall). n denotes the direction normal to the wall.

Figure 2.4 shows a sketch for the implementation of the wall boundary in numerical simulations. To ensure that the velocities are zero at the wall, the following statements are used:

$$\begin{aligned} f_g &= -f_j; \\ f_{g+1} &= -f_{j+1}; \\ f_{g+2} &= -f_{j+2}, \end{aligned} \tag{2.40}$$

where f corresponds to $\bar{u}, \bar{v}$, and $\bar{w}$. The corresponding statements for temperature (adiabatic wall) are identical to Eq. (2.37).

In terms of the periodic boundary condition for the lateral surfaces, figure 2.5 provides a sketch for its numerical implementation. The key is to ensure that all the fluxes at both spanwise boundaries are identical. Thus, the information at the first three real grid points on the left side is sent to the ghost grid points on the right side and vice versa:

$$\begin{aligned} f_g &= f_k; \\ f_{g+1} &= f_{k+1}; \\ f_{g+2} &= f_{k+2}. \end{aligned} \tag{2.41}$$

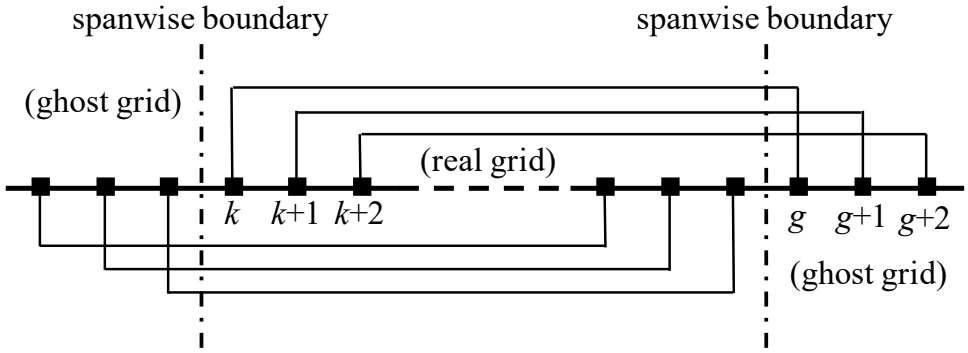


Figure 2.5: Schematic illustration for the periodic boundary condition.

It is noted that in the present thesis, one case with in-flow boundary condition on the lateral sides is considered to mimic the experimental setup. For this case, the values on the ghost grid points on both sides are approximated by the free-stream values, which will be discussed in detail in Chapter 3.

Regarding the initial condition, it is convenient to prescribe the free-stream values (q_∞) for all the real grid points at the beginning of the simulation, i.e. at $\bar{t} = 0$:

$$f(\bar{t} = 0) = q_\infty, f = \{\bar{u}, \bar{v}, \bar{w}, \bar{p}, \bar{\rho}\}. \tag{2.42}$$

Note that this is only applied for two-dimensional simulations. For three-dimensional simulations, the initial flow field is directly extrapolated from the converged results of the two-dimensional simulations.

2.4 Further numerical implementation

The DNS solver is programmed in C language in a Linux platform. In order to carry out simulations with large numerical costs in a realistic time, the solver is parallelized by message passing interface (MPI) [64]. For the implementation of MPI, the whole computational domain has to be divided into several sub-domains with each sub-domain running in one process. The number of grid points in each sub-domain is identical. In order to exchange the data from one process to another and fulfil the requirement for the employed high order schemes, three extra grid points are added in each direction for all sub-domains. Figure 2.6 illustrates the internal communication between two neighbouring sub-domains. The constructed DNS solver showed a high scalability when tested in different supercomputer platforms [77]. Based on tests conducted on new generation computers (CLAIX-2016 and CLAIX-2018) at RWTH Aachen University, the typical code performance of the DNS solver is 0.011 $\frac{\text{core}\cdot\text{millisecond}}{\text{point}\cdot\text{step}}$.

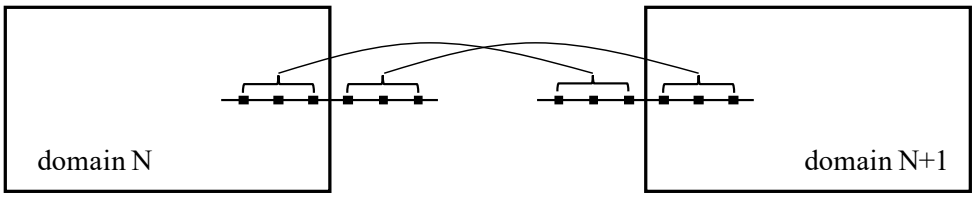


Figure 2.6: Schematic illustration for the internal communication between two neighbouring sub-domains.

3 Mesh Study and Validation

In this chapter, a comprehensive mesh study is performed to demonstrate the grid independence for the considered hypersonic compression ramp flows. In addition, the accuracy of the solutions is validated by comparing with theoretical predictions and several experimental and numerical data. To carry out the mesh study and validation, it is convenient to divide the compression ramp flow field into three regions shown in figure 3.1, which are characterised by different flow phenomena. Region I refers to the area from the leading edge up to the beginning of the shock boundary-layer interaction. In this region the viscous flow is typical of a flat plate boundary layer. Region II corresponds to the main region of SWBLI, where the boundary layer on the flat plate separates when experiencing a strong adverse pressure gradient induced by the ramp shock and subsequently reattaches on the ramp. Region III is located downstream of reattachment, where the streamwise vortices develop. In the following, the mesh study is conducted concerning these three flow phenomena.

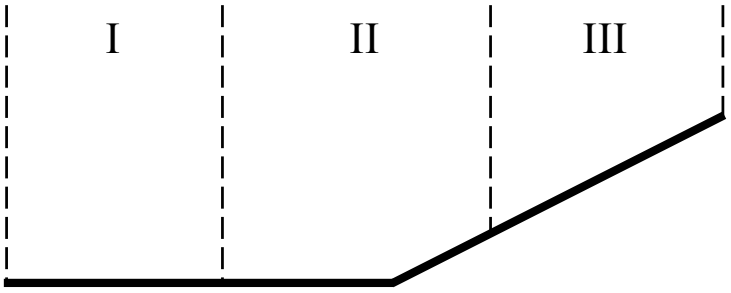


Figure 3.1: Regions of compression ramp flow.

3.1 Region I: Hypersonic laminar boundary layer flow on a flat plate

The flow conditions considered in the mesh study are based on those used in the experimental campaign carried out in the hypersonic Aachen Shock Tunnel TH2 at the Shock Wave Laboratory of RWTH Aachen University. Table 3.1 lists the flow conditions including the wall temperature T_w. Due to the short running time of the shock tunnel, the model wall is usually treated as an isothermal wall. The total enthalpy h_0 is relatively low allowing a perfect gas assumption. The compression ramp model used in the experiments includes a flat plate with a sharp leading edge, whose length is $L = 100$ mm. Hence, in

this section, the same configuration is used to study the flat plate boundary layer flow. Based on the flow conditions given in Table 3.1, a laminar boundary layer is expected on the flat plate ($Re_{\infty,L} = 4.2 \times 10^5$).

Table 3.1: Flow conditions: Condition I at the shock tunnel TH2 [78].

M_∞	Re_∞ (m^{-1})	h_0 (MJ/kg)	T_∞ (K)	p_∞ (Pa)	u_∞ (m/s)	T_w (K)
7.7	4.2×10^6	1.7	125	760	1726	293

To resolve a flat plate boundary layer in the hypersonic regime, apart from the near wall refinement, special consideration should be given to the viscous interaction occurring at the leading edge. Table 3.2 lists the considered meshes for the grid independence study of the flat plate boundary-layer flow. Near the leading edge ($x/L = 0$), the mesh is clustered in streamwise direction, and the number of grid points located within 5% of the flat plate length is given in the third column. In wall-normal direction, the first ten grid points maintain a constant spacing which is shown as $\Delta y_w/L$ in the fourth column. Then, the mesh is stretched by a factor of 1.02 in a clustered layer near the wall. The remaining mesh is stretched by a factor of 1.06. Figure 3.2 shows a simple mesh distribution for case A2. Furthermore, the number of grid points inside the boundary layer ($y \leq \delta_{0.99}$) at $x/L = 1$ is shown in the last column. Note that the boundary layer thickness at $x/L = 1$ is 1.9 mm. For all cases, the rectangular physical domain has a height of 20 mm and a length of 101 mm. In order to introduce the free-stream flow, ten (case A1) or twenty (cases A2 and A3) grid points are placed ahead of the leading edge in a section of 1 mm length ($-0.01 \leq x/L \leq 0$). It is noted that in this and the following chapters, the Cartesian coordinates x, y, z are normalised by the flat plate length L.

Table 3.2: Cases for the mesh study of the flat plate boundary layer flow.

Case	Mesh	N_i ($0 \leq x/L \leq 0.05$)	$\Delta y_w/L$ ($\times 10^{-5}$)	N_j ($y \leq \delta_{0.99}$)
A1	160×60	30	41	30
A2	360×120	60	15	62
A3	480×180	120	8	94

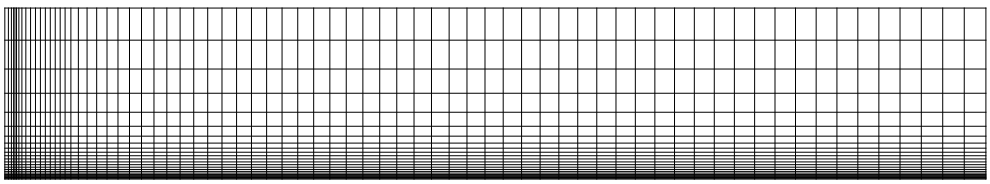


Figure 3.2: Mesh distribution for case A2 (each 5th point is shown).

Figure 3.3 shows the temporal history of the pressure and temperature inside the boundary layer at $x/L = 1$ for case A2. A steady state of the boundary layer flow is achieved from $\bar{t} = 5$ on. Note that due to the presence of a leading edge shock induced by the viscous interaction, the pressure is slightly higher than the free-stream value.

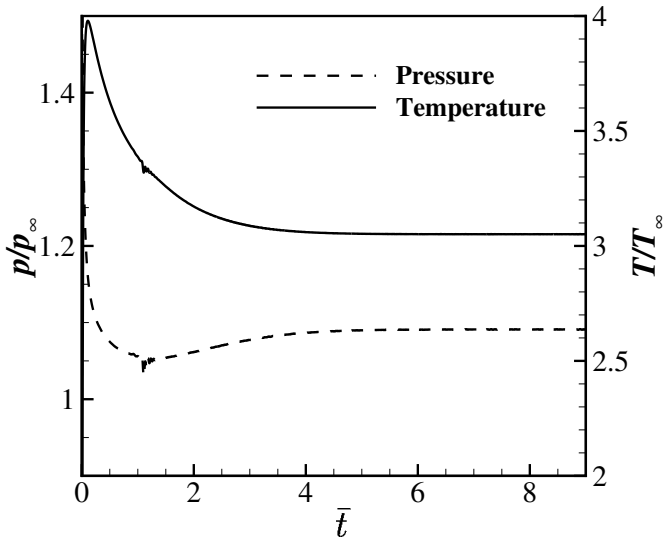


Figure 3.3: Temporal history of pressure and temperature signals at $x/L = 1$ and $y/L = 0.0012$ for case A2.

For a hypersonic boundary layer over a flat plate, two regions of viscous interaction are identified, i.e. strong and weak interaction region [79]. A region is defined as a strong interaction when the viscous interaction parameter $\bar{\chi}$ $(= M_\infty^3\sqrt{C}/\sqrt{Re_{\infty,x}})$ is larger than 3. For the flow conditions considered herein, $\bar{\chi} = 3$ corresponds to $x/L = 0.05$. Therefore, the strong interaction region is located at $0 \leq x/L \leq 0.05$. The pressure induced by a strong viscous interaction can be expressed as [79]

$$p/p_\infty = 1 + 0.15\bar{\chi}, \tag{3.1}$$

and the pressure in the weak interaction region is given by [80, 81]

$$p/p_\infty = 1 + \frac{1}{2}\gamma A\bar{\chi}, \tag{3.2}$$

where $A = (\gamma - 1) \cdot 0.332 \cdot (1 + 2.6 \cdot T_w/T_0)$ with T_0 being the total temperature. Figure 3.4 illustrates the induced pressure distribution by the viscous interaction and the corresponding comparison with Eqs. (3.1) and (3.2). It is shown that in the weak interaction region ($x/L > 0.05$), the induced pressures are in excellent agreement with the theoretical prediction for all cases. In the strong interaction region, however, the pressure is

over estimated by case A1 due to an over-prediction of the leading edge shock strength. Moreover, the induced pressures for cases A2 and A3 are almost identical from $x/L = 0.05$ up to $x/L = 0.007$. Further upstream, the pressure distribution has a small discrepancy with Eq. (3.1) for both cases. It should be noted that in the immediate neighbourhood of the leading edge, both numerical and theoretical results are invalid because the continuum assumption breaks down.

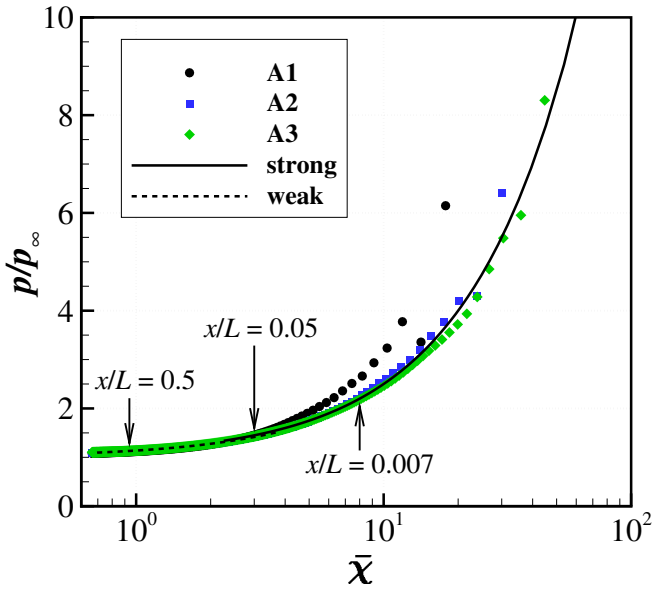


Figure 3.4: Streamwise distribution of the surface pressure on the flat plate for case A.

Subsequently, figure 3.5 shows the streamwise distribution of the skin friction coefficient (c_f) for cases A1, A2 and A3 (or case A for short). To validate the accuracy of the results, a theoretical estimation [82] based on the reference temperature concept [83] is compared:

$$c_f^* = \frac{0.664\sqrt{C^*}}{\sqrt{Re_{e,x}}}, \tag{3.3}$$

where C^* is the Chapman-Rubsin parameter evaluated at a reference temperature T^*, and the subscript e denotes the condition at the edge of the boundary layer. Since the viscous interaction is weak in most regions, the free-stream values are employed as the condition at the boundary-layer edge. The most popular correlation for T^* is due to Eckert [83]:

$$\frac{T^*}{T_e} = 1 + 0.032M_e^2 + 0.58\left(\frac{T_w}{T_e} - 1\right). \tag{3.4}$$

As seen in figure 3.5, while case A1 under estimates the skin friction, cases A2 and A3 yield almost identical values which are in good agreement with the theoretical prediction (Eq. 3.3).

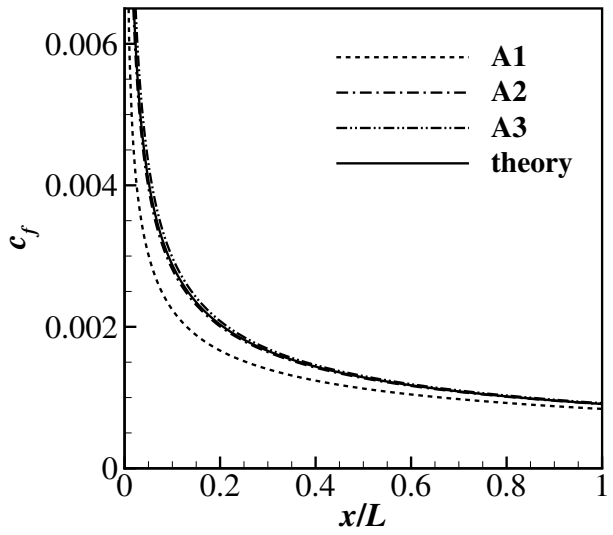


Figure 3.5: Streamwise distribution of the skin friction coefficient for case A. The theoretical value is calculated with Eq. 3.3.

Finally, the numerically resolved boundary layer velocity and temperature profiles are compared with the similarity solutions of the compressible boundary layer equations [79, 82]. Figure 3.6 shows the velocity and temperature boundary layer profiles at $x/L = 1$. Once again, almost identical temperature and velocity profiles are apparent for cases A2 and A3, and they agree well with the similarity solution. Note that the small deviation can be attributed to the zero streamwise pressure gradient assumption introduced in the solution of the compressible boundary layer equations [82]. Based on the above discussions on the viscous interactions, skin friction coefficient and boundary layer profiles, it can be concluded that the mesh resolution for case A2 is sufficient to resolve the considered flat plate boundary-layer flow.

3.2 Region II: Laminar separation in hypersonic compression ramp flow

When the flat plate is followed by a ramp with a deflection angle of 15°, the boundary layer separates upstream of the corner and reattaches on the ramp. In the following, 2-D simulations are performed to study the grid independence of the compression ramp flow for the flow conditions given in Table 3.1. The length of the ramp is also 100 mm. Based on the results obtained previously, four meshes listed in Table 3.3 are considered. The

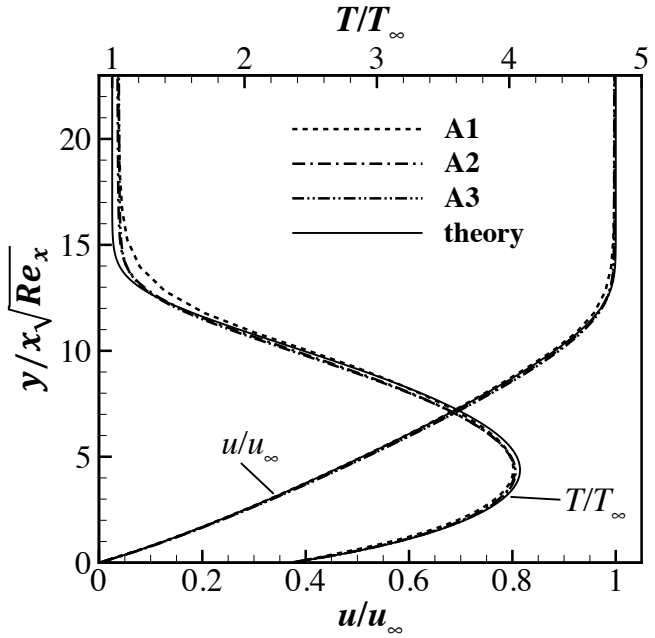


Figure 3.6: Flat plate boundary layer profiles at $x/L = 1$ for case A.

same mesh distribution near the leading edge ($0 \leq x/L \leq 0.05$) and wall-normal mesh spacing as for case A2 are used for case B1. Then, wall-normal grid points are doubled for case B2. Next, streamwise grid points are doubled for case B3. Finally, grid refinements are made simultaneously in streamwise and wall-normal directions for case B4. As shown in figure 3.7, where a sample mesh distribution for case B3 is presented, the wall-normal mesh on the flat plate and the ramp is perpendicular to the surface except for regions near the corner and the outlet. Near the corner ($0.8 \leq x/L \leq 1.2$), an arc segment is used at the upper boundary to smoothly connect the mesh on the flat plate and the ramp. Note that the streamwise mesh is equi-spaced at $0.15 \leq x/L \leq 0.75$ and $1.0 \leq x/L \leq 1.9$. But the mesh spacing in the former region ($\Delta x/L = 0.0026$) is larger than that in the latter region ($\Delta x/L = 0.0016$). Furthermore, the number of grid points located in the boundary layer at the separation position x_s is also listed in the last column.

Table 3.3: Cases for the mesh study of the two-dimensional compression ramp flow.

Case	Mesh	N_i ($0 \leq x/L \leq 0.05$)	$\Delta y_w/L$ ($\times 10^{-5}$)	N_j ($y \leq \delta_{0.99}$)
B1	540×120	60	15	49
B2	540×240	60	8	75
B3	1080×240	90	8	75
B4	1600×320	90	5	118

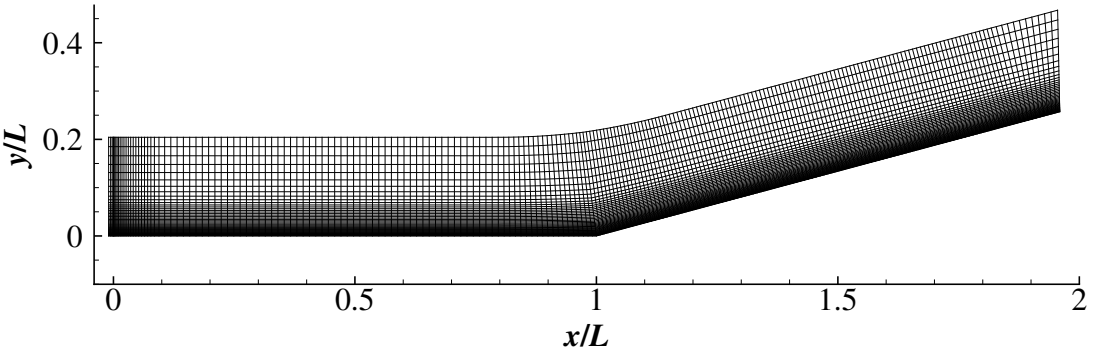


Figure 3.7: Mesh distribution for case B3 (each 5th point is shown).

As aforementioned, the laminar boundary layer flow on the flat plate is fully established after $\bar{t} = 5$ (see figure 3.3). However, the flow establishment time is much longer for the separated compression ramp flow. Figure 3.8 presents the temporal evolution of the separation bubble size for case B3. The separation and reattachment positions are determined by the positions where the skin friction coefficient is zero. It is obvious that the separation bubble grows rapidly during the early stage. Subsequently, it extends gradually until about $\bar{t} = 100$, from which on the size of the separation bubble is almost constant. Figure 3.9 shows the temporally converged numerical schlieren for case B3. The separation and reattachment positions are marked as 's'and 'r', respectively. The intersection of the separation and reattachment shock is the triple point 'T'. This 2-D converged flow field is later used as an initial flow field for 3-D simulations. This procedure significantly saves computing resources.

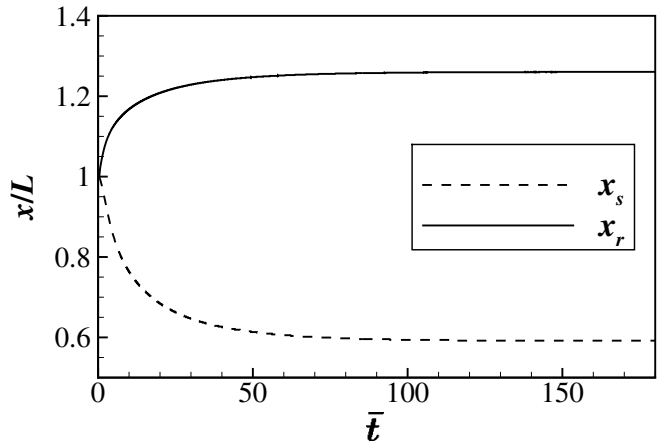


Figure 3.8: Temporal evolution of the separation (x_s) and reattachment (x_r) point for case B3.

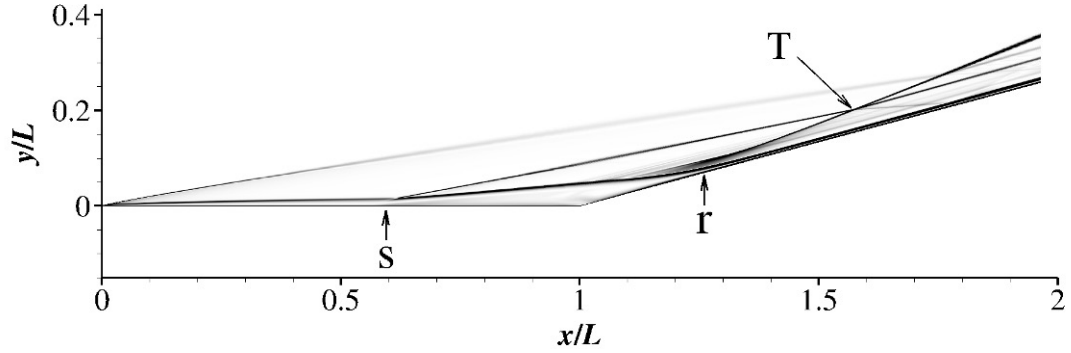


Figure 3.9: Numerical schlieren for case B3. The symbols s, r and T denote the separation position, reattachment position and triple point, respectively.

The length of the separation bubble is a good measure of the quality of mesh resolution. The separation and reattachment positions as well as the separation bubble length L_b/L obtained from the converged flow field for cases B1-B4 (case B for short) are shown in Table 3.4. Compared to case B1, the separation point moves upstream by 3.1%, and the reattachment point moves downstream by 1.4% for the finest mesh case B4. As a result, the separation bubble length increases by 5.8%. It is also seen that the rise in the separation bubble length from case B2 to B4 is very small (1.2%). Furthermore, figure 3.10 shows the pressure coefficient (c_p) and the Stanton number (St) distributions along the wall for case B, which are defined as

$$c_p = \frac{p - p_\infty}{\frac{1}{2}\rho_\infty u_\infty^2}, \tag{3.5}$$

$$St = \frac{q_w}{\rho_\infty u_\infty (h_{aw} - h_w)}, \tag{3.6}$$

where q_w is the surface heat flux, h_{aw} and h_w are the adiabatic wall enthalpy and wall enthalpy respectively [79]. The almost identical separation bubble length for cases B2, B3 and B4 is apparent. However, visible fluctuations exist in the separation bubble and downstream of reattachment for cases B1 and B2 for the Stanton number distribution. This is due to the insufficient mesh resolution in streamwise direction. By doubling the grid points in streamwise direction (case B3), the fluctuations disappear. While the difference between cases B3 and B4 is insignificant, both cases will be examined with respect to the 3-D flow phenomena associated with the streamwise vortices in the next section. Furthermore, the pressure rise due to SWBLI is compared with the inviscid pressure jump in figure 3.10(a). The inviscid pressure jump is calculated by oblique shock theory:

$$c_{p,inviscid} = \frac{4}{1+\gamma}\left(\sin^2\beta - \frac{1}{M_\infty^2}\right), \tag{3.7}$$

where β is the shock angle which is determined by the free-stream Mach number and ramp angle. It is seen that in the vicinity of reattachment, the pressure rise induced by the SWBLI is increased by 18% compared to the inviscid level. However, due to the impingement of the expansion wave emanating from the triple point (see figure 3.9), the pressure decreases at $x/L = 1.8$ and then becomes close to the inviscid level.

Table 3.4: Separation and reattachment positions and the separation bubble length for case B.

Case	x_s/L	x_r/L	L_b/L
B1	0.611	1.246	0.635
B2	0.595	1.259	0.664
B3	0.594	1.261	0.667
B4	0.592	1.264	0.672

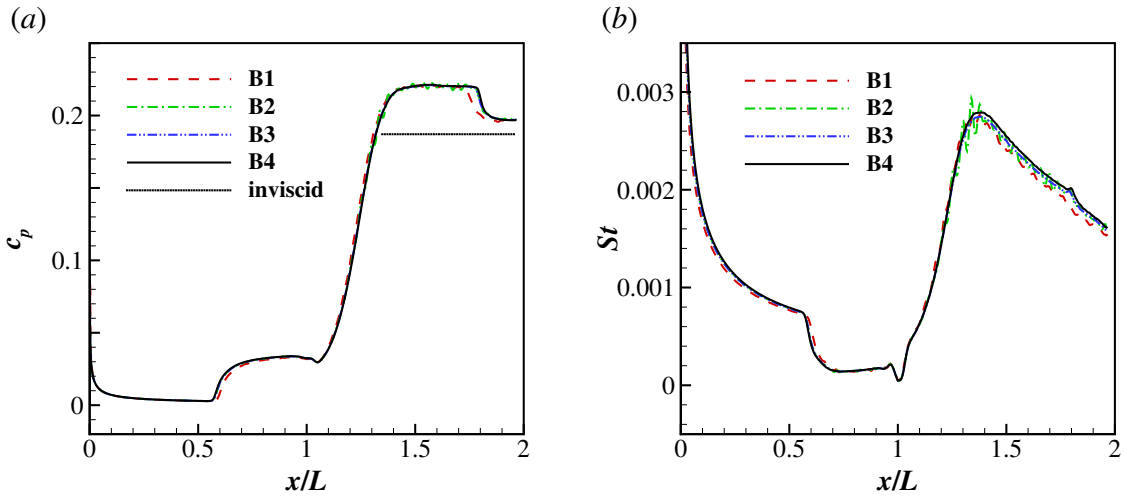


Figure 3.10: Pressure coefficient and Stanton number distributions along the wall for case B.

Additionally, to examine the accuracy and efficiency of the present DNS solver, the numerical simulations performed using a famous CFD solver - US3D - are employed. US3D is a finite volume-based solver which was developed at the University of Minnesota specifically for high-speed flows [84, 85]. The utilised flow conditions and geometry are [86]: $M_\infty = 9.0$, $Re_\infty = 3.3 \times 10^6$ m^{-1}, $T_\infty = 160$ K, $T_w/T_0 = 0.11$, $L = 85$ mm and the ramp angle is 18°. These are based on the experimental studies performed by Mallinson et al. [87]. The numerical simulations were conducted by Gai and Khraibut [86], who used a high mesh resolution of 4031×1009 grid points to resolve the considered compression ramp flow. The comparison of the surface pressure coefficient is shown in figure 3.11. Excellent agreement is achieved except for a very small deviation of the separation position. In

fact, the reported separation bubble length in [86] is $\Delta x/L = 0.878$, compared to 0.849 in the present DNS results, yielding a deviation of 3.3%. As demonstrated by Gai and Khraibut [86], the separation bubble length obtained with a mesh resolution of 1194×299 yields a deviation of 27% compared to the finest mesh case (4031 × 1009). However, the applied mesh size in the present DNS is 1080×240. It means that much less grid points are required to resolve the compression ramp flow when using the present DNS solver.

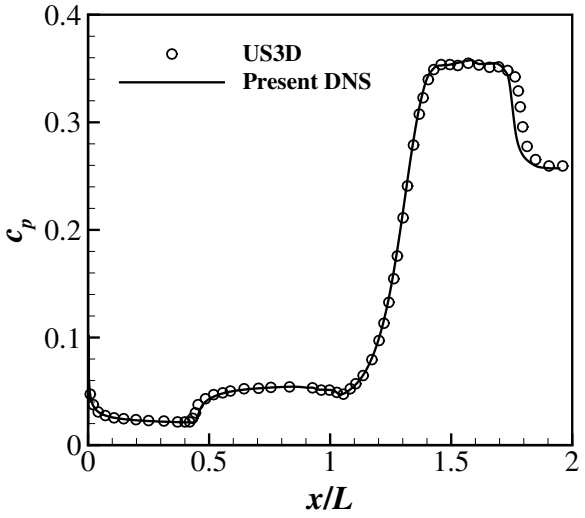


Figure 3.11: Comparison of the surface pressure coefficient for the present DNS results and the results obtained by Gai and Khraibut [86].

3.3 Region III: Streamwise vortices downstream of reattachment

Due to the presence of the streamwise vortices, a highly three-dimensional flow forms near and downstream of reattachment. Therefore, a comprehensive three-dimensional mesh study is required to ensure the grid convergence for this flow phenomenon. As shown in Table 3.5, five cases with different mesh resolutions, spanwise widths (L_z) and initial spanwise velocity (w) distributions are considered. The spanwise length of the compression ramp configuration L_z is listed in the third column. The mesh is uniformly distributed in spanwise direction, as shown in figure 3.12, and the constant mesh spacing ($\Delta z/L$) is listed in the fourth column. Periodic boundary conditions are prescribed in spanwise directions. Note that the experimental model has a width of 200 mm [16]. The same flow conditions as listed in Table 3.1 are applied here. Note that all three-dimensional simulations start at the new nominal time $\bar{t} = 0$, and the initial flow field is extrapolated from the converged results of cases B3 or B4 by duplicating the 2-D flow field in spanwise

direction. To accelerate the growth of three-dimensionality, an initial distribution of the spanwise velocity component (w) is imposed for cases C1, C2, C4 and C5. Specifically, a random distribution of $w/u_\infty \in [-0.02, 0.02]$ is used for the first twenty wall-normal grid points at the first time step. Note that from the second time step on, no artificial disturbances are imposed. The initial disturbances dissipate quickly but contributes to the growth of three-dimensionality. To investigate the influence of this initialisation, for case C3 the initial flow is assumed to be nominally two-dimensional ($w/u_\infty = 0$). In this case the numerical round-off error provides an extremely low-level disturbance for the growth of three-dimensionality.

Table 3.5: Three-dimensional mesh cases for the grid independence study.

Case	Mesh	L_z (mm)	$\Delta z/L(\times 10^{-3})$	Initial w
C1	$1080 \times 240 \times 120$	100	8.33	random
C2	$1080 \times 240 \times 240$	100	4.17	random
C3	$1080 \times 240 \times 240$	100	4.17	0
C4	$1080 \times 240 \times 480$	100	2.08	random
C5	$1600 \times 320 \times 240$	30	1.25	random

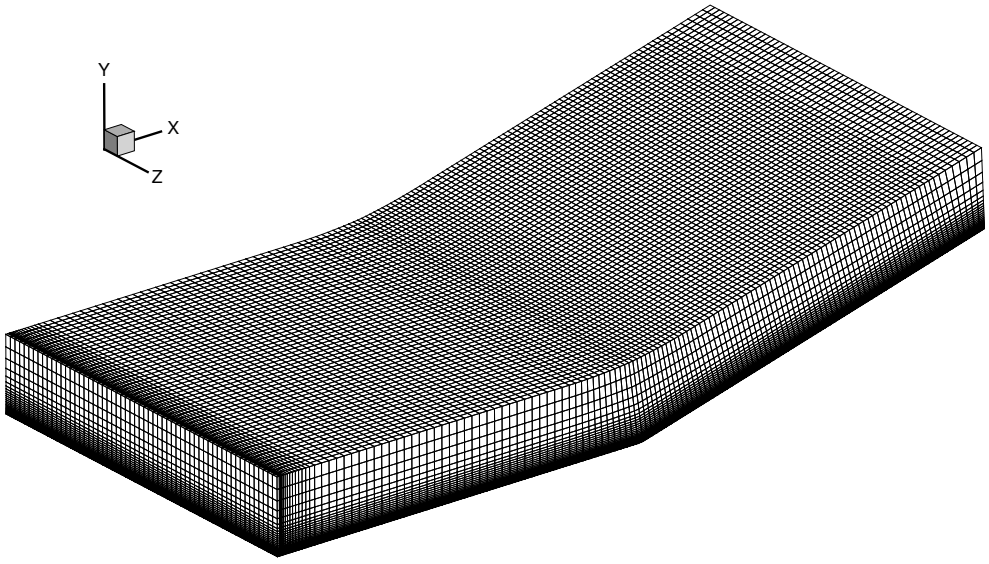


Figure 3.12: Mesh distribution for case C4 (each 8th point is shown).

In the following, the temporal evolution of the 3-D compression ramp flows is discussed. The development of three-dimensionality can be detected by monitoring the surface heat flux. For example, figure 3.13 presents the instantaneous wall Stanton number distribution at six instants of time for case C4. It is noted that the solid lines highlight the position

where the skin friction coefficient is zero. Therefore, the separation and reattachment positions can be identified in the figure. At $\bar{t} = 0$, the initial flow field is a simple extrapolation in spanwise direction of the two-dimensional converged solution. At $\bar{t} = 9$, three-dimensionality occurs inside and downstream of the separation bubble. Streamwise heat flux streaks are visible near the peak heating position downstream of reattachment. At $\bar{t} = 21$, the magnitude of the spanwise variation of the wall Stanton number becomes larger, and the reattachment line becomes meandering. The streamwise streaks at $\bar{t} = 45$, 60 and 120 appear to have similar magnitude and wavelength. But the generally different wall Stanton number distributions at different instants of time indicate that the flow is unsteady.

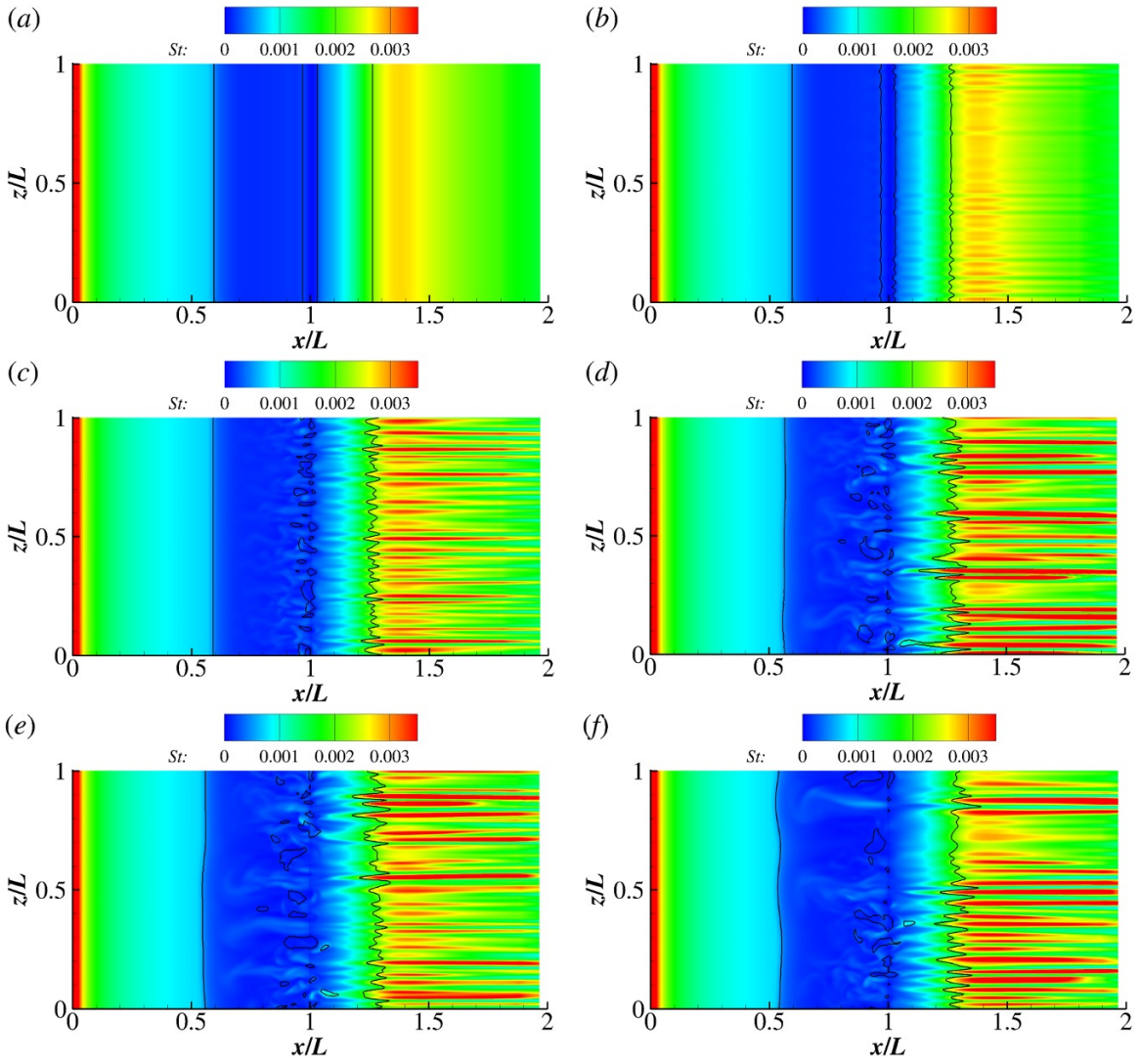


Figure 3.13: Wall Stanton number distribution (top view) for case C4 at different instants of time, a)-f) correspond to $\bar{t} = 0$, 9, 21, 45, 60, 120. Solid lines denote iso-lines of zero skin friction coefficient. Flow from left to right.

The unsteady surface heat flux distribution is demonstrated by showing the temporal history of the wall Stanton number at $x/L = 1.5$ and $z/L = 0.5$ in figure 3.14. An obvious fluctuation is apparent from $\bar{t} = 12$ on. Furthermore, the unsteadiness seems to cover several frequencies which are relatively low compared to the typical frequencies in a transitional or turbulent flow. The flow unsteadiness for this compression ramp flow is investigated in depth in Chapter 5.

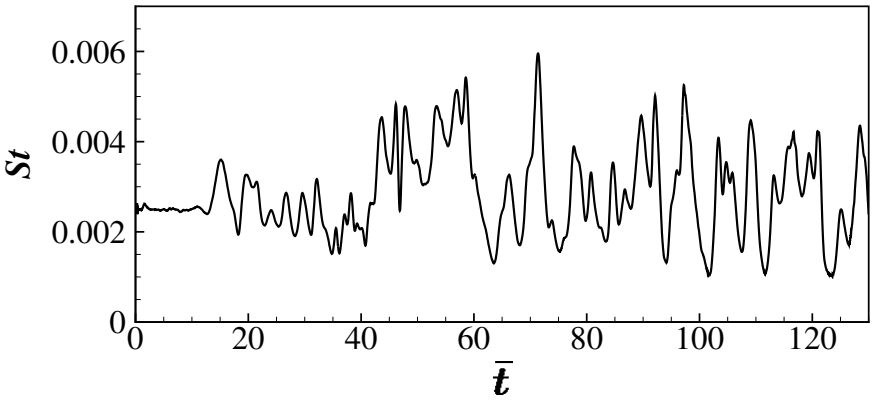


Figure 3.14: Temporal history of the wall Stanton number at $x/L = 1.5$ and $z/L = 0.5$ for case C4.

In order to identify the growth of three-dimensionality in the flow field, two relevant parameters are analysed. The first one measures the standard variation of the spanwise variation of the wall Stanton number at a certain streamwise position:

$$\sigma_{St} = \sqrt{\frac{1}{N_z} \sum_{k=1}^{N_z} (St_k - St_z)^2}, \tag{3.8}$$

where N_z denotes the number of grid points in spanwise direction, and St_z is the spanwise-averaged wall Stanton number at a streamwise position. The streamwise position $x/L = 1.5$ is exemplarily chosen to show the temporal growth of the spanwise heat flux variation downstream of reattachment (see figure 3.13 for the position). The temporal evolution of σ_{St} at $x/L = 1.5$ is presented in figure 3.15. After an initial adaption, the spanwise variation of the wall Stanton number experiences a rapid increase until about $\bar{t} = 14$ which is followed by a progressive growth up to about $\bar{t} = 50$. For the subsequent temporal evolution, the standard deviation is nearly constant.

The second parameter measures the absolute value of the nondimensionalised spanwise velocity in a y-z plane:

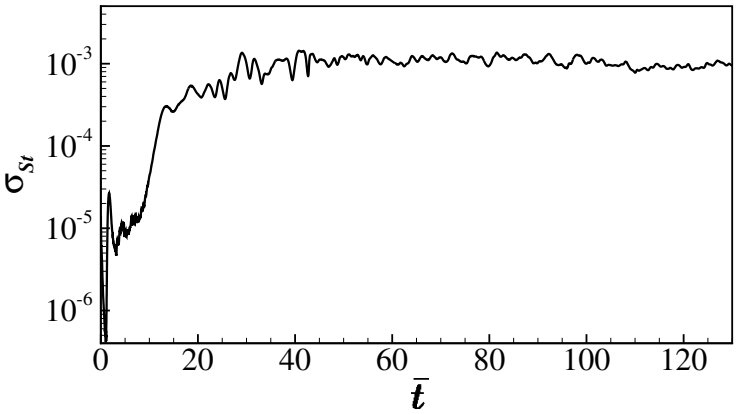


Figure 3.15: Temporal growth of the standard deviation of the spanwise Stanton number variation (Eq. 3.8) at $x/L = 1.5$ for case C4.

$$\sigma_w = \sqrt{\frac{1}{N_y N_z} \sum_{j=1}^{N_y} \sum_{k=1}^{N_z} (w/u_\infty)^2_{j,k}}, \tag{3.9}$$

where N_y is the number of grid points in wall-normal direction. Figure 3.16 shows the temporal evolution of σ_w at $x/L = 1.04$. As seen, the initialised random value of $\sigma_w = 5 \times 10^{-5}$ damps to 1×10^{-5} at the very beginning. Then, an exponential growth stage takes place which ends at about $tu_\infty/L = 12$. Subsequently, the spanwise velocity grows progressively until reaching the asymptotic level at about $tu_\infty/L = 50 \sim 60$. The reason of showing σ_w at $x/L = 1.04$ is given as follows.

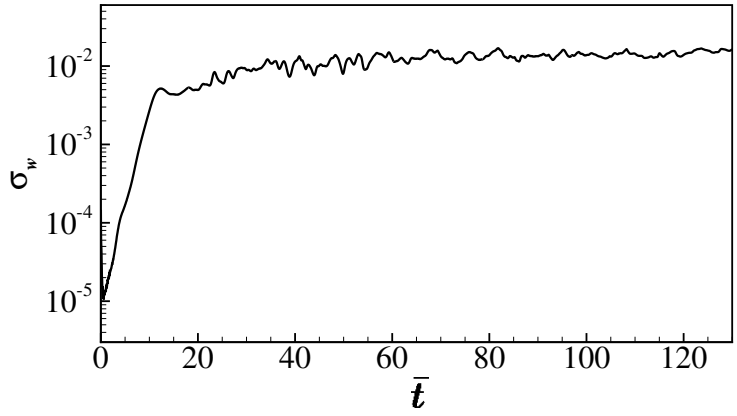


Figure 3.16: Temporal growth of the spanwise velocity (Eq. 3.9) at $x/L = 1.04$ for case C4.

By examining σ_w at all x positions, it is found that the largest quantity occurs at $x/L = 1.04$ during the exponential growth stage. The streamwise distribution of σ_w at $tu_\infty/L =$

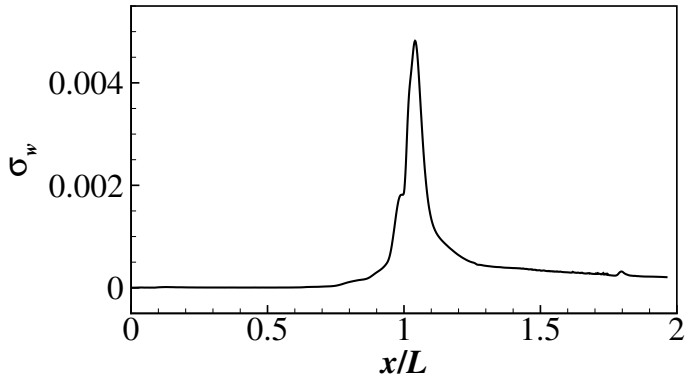


Figure 3.17: Streamwise distribution of the spanwise velocity (Eq. 3.9) at $\bar{t} = 9$ for case C4.

9 is presented in figure 3.17, where this instant of time has been chosen exemplarily for the exponential growth stage. Note that the separation bubble is located at $0.59 < x/L < 1.26$. Therefore, the three-dimensionality is mainly confined in the separation bubble at this instant of time. On the basis of the above discussions about the temporal evolution (figures 3.14-3.16), it can be concluded that for case C4, the three-dimensional flow is fully established prior to $\bar{t} = 60$.

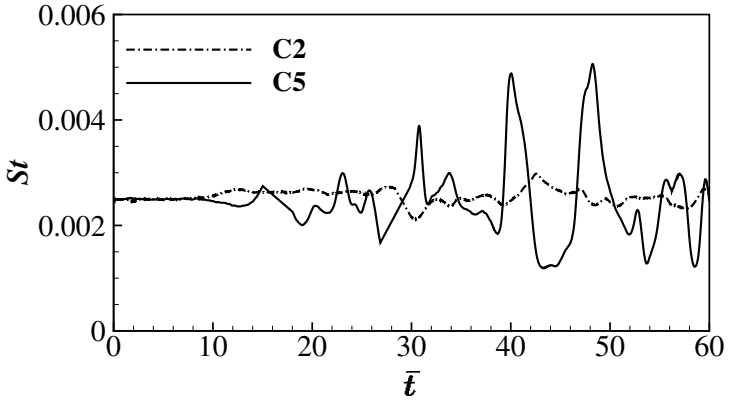


Figure 3.18: Temporal history of the wall Stanton number at $x/L = 1.5$ and $z/L = 0.5$ for case C2 and $x/L = 1.5$ and $z/L = 0.15$ for case C5.

The temporal convergence to a quasi-steady state for other cases is briefly discussed in the following. For grid C1, the results show that the flow reaches a steady state at $\bar{t} = 15$, and the spanwise variation of the surface heat flux is very weak, as shown later. This is due to the insufficient mesh resolution in spanwise direction. Figure 3.18 shows the temporal evolution of the wall Stanton number for cases C2 and C5. It is seen that the flow is also unsteady. After about $\bar{t} = 30$, distinct fluctuations are observed for both cases although the amplitude for case C2 is much lower than that for case C5. The difference in the amplitude is attributed to the different mesh resolution, which is discussed below.

To conclude, the simulated time period ensures the flow establishment for the considered cases. The corresponding total simulated time for cases C1-C5 amounts to $\bar{t} = 30$, 60, 60, 130, 60. Note that the long-period simulation performed for case C4 enables the analysis of the flow unsteadiness in Chapter 5.

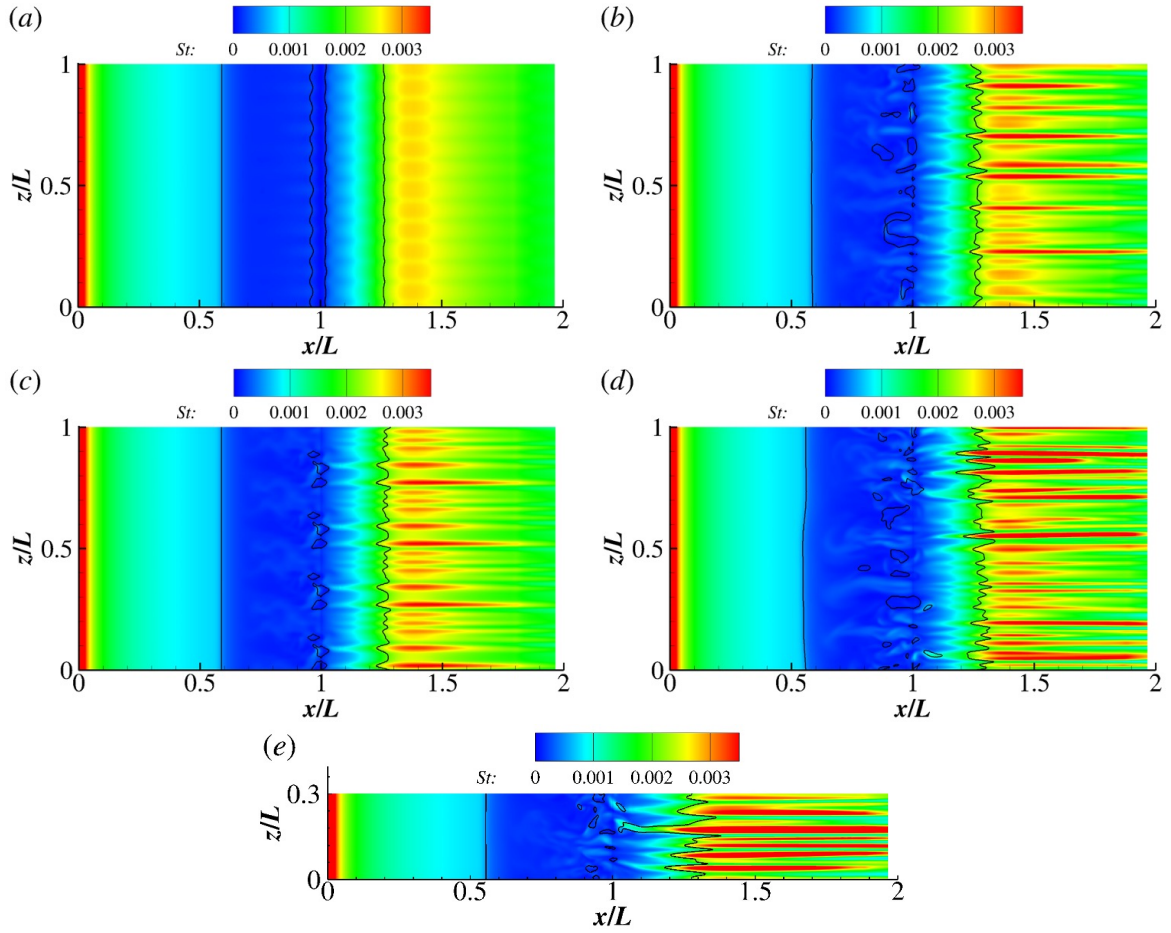


Figure 3.19: Wall Stanton number distributions (top view) for case C1 at $\bar{t} = 30$ and cases C2-C5 at $\bar{t} = 60$. a)-e) correspond to cases C1, C2, C3, C4 and C5. Solid lines denote iso-lines of zero skin friction coefficient. Flow from left to right.

Figure 3.19 illustrates the wall Stanton number distribution at $\bar{t} = 30$ for case C1 and $\bar{t} = 60$ for cases C2-C5. Firstly, the influence of the spanwise mesh resolution is analysed by considering cases C1, C2, and C4, for which the spanwise length of the compression ramp is 100 mm. Compared to cases C2 and C4, there is no distinct spanwise heat flux variation for case C1, which means its spanwise mesh is too coarse to resolve the streamwise vortices. Note that a very weak variation can be observed for case C1 due to an established three-dimensional flow in the separation bubble. By further increasing the spanwise mesh resolution for cases C2 and C4, considerable spanwise heat flux variations are clearly seen (figures 3.19(b) and 3.19(d)). The wavelength of the heat flux streaks is approximately 5 mm, which is consistent with the experimental results [16, 17]. However,

the overall amplitude of the Stanton number for case C2 is smaller than for case C4, which can be seen in figure 3.20, where the spanwise variation of the wall Stanton number at a exemplary streamwise position is shown for cases C1-C5. It indicates that the utilised mesh for case C2 cannot fully resolve the three-dimensionality in the flow field. In fact, the number of spanwise grid points per wavelength is estimated at about 12 for case C2 and 24 for case C4. Next, case C5 of the highest mesh resolution in all directions is employed to examine the grid independence. As shown by figure 3.19(e), the wavelength of the heat flux streaks for case C5 is found to be consistent with cases C2 and C4, although the number of spanwise grid points per wavelength is much higher (about 40). Furthermore, as shown in figure 3.20, the amplitudes of the spanwise variations for cases C4 and C5 are also comparable. Therefore, it can be concluded that the grid independence for the considered compression ramp flow is achieved for the mesh resolution of case C4. In addition, by comparing cases C4 and C5, the wavelength appears to be independent of the spanwise length of the compression ramp when periodic boundary conditions are applied in spanwise direction.

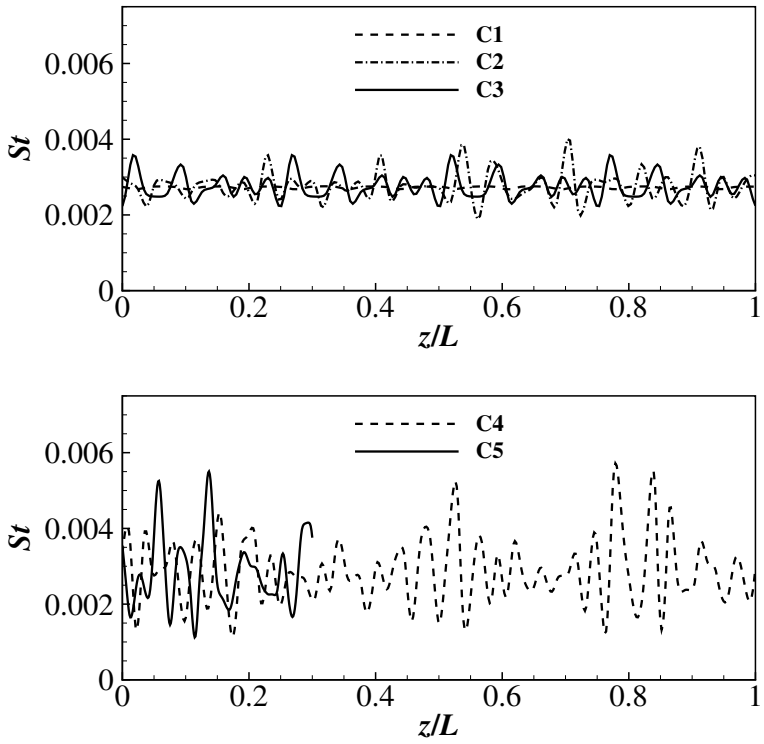


Figure 3.20: Spanwise wall Stanton number distributions for cases C1-C5 at $x/L = 1.4$ and the same instants of time as in figure 3.19.

The influence of introducing an initial spanwise velocity distribution is discussed in the following. Because the initial spanwise velocity is set to zero for case C3, the growth of the disturbances provided by the numerical round-off error is weaker than that for case C2. As a result, it takes more time for case C3 to achieve the same state as case

C2. For instance, the results show that distinct surface heat flux variations (the streaks) can be observed at about $\bar{t} = 30$ for case C2, whereas for case C3 this occurs later at about $\bar{t} = 50$. As shown in figure 3.19(c), a similar heat flux variation to case C2 can be observed for case C3. The wavelength and mean amplitude are also comparable for both cases. It has to be mentioned that the flow especially on the ramp is highly unsteady and therefore for the considered instant of time the agreement is more qualitative. Another important observation is that for case C3 the flow shows a large scale periodicity (more strictly, four periods) in spanwise direction, which does not occur for case 2. The reason is as follows. In spanwise direction, four mesh blocks are utilised for parallel computing. The numerical round-off error is identical at all corresponding points in the four blocks. Hence, the flow field is repeatedly simulated fourfold. In order to avoid this behaviour, one should either use one block in spanwise direction or impose a random initial disturbance as for the other four cases. Nevertheless, it is shown that three-dimensionality can arise in a two-dimensional initial flow field without imposing any initial disturbances in the third dimension. Hence, it can be concluded that after a sufficiently long period of time, the final quasi-steady state of the flow field is independent of the initial distribution of the spanwise velocity component.

3.4 High Reynolds number condition

In the experiments, except for the main condition (Condition I) considered above, an additional flow condition with a higher free-stream unit Reynolds number of 8.6×10^6 m^{-1} (Condition XI) was also considered [78], (see Table 3.6). The higher Reynolds number is achieved by increasing the stagnation pressure. To carry out the mesh study for this case, two mesh resolutions are considered. As listed in Table 3.7, a similar mesh resolution to case C4 is used for case D1. Grid refinement is then made in all three dimensions for case D2. The spanwise length of the compression ramp for cases D1 and D2 amounts to 100 mm and 30 mm respectively. Periodic boundary conditions are applied in spanwise direction. The same random initial distribution for the spanwise velocity component as for case C4 is employed for cases D1 and D2. In the following, the temporal and spatial convergence in terms of the 2-D simulation is firstly analysed. Subsequently, the establishment of three-dimensional flow and the grid independence of the concerning flow phenomena are discussed in detail.

Table 3.6: Flow conditions: Condition XI at the shock tunnel TH2 [78].

M_∞	Re_∞ (m^{-1})	h_0 (MJ/kg)	T_∞ (K)	p_∞ (Pa)	u_∞ (m/s)	T_w (K)
7.7	8.6×10^6	1.7	125	1550	1726	293

Figure 3.21 presents the temporal evolution of the separation and reattachment positions for the 2-D simulation of case D1. Note that the 2-D simulation provides an initial flow

Table 3.7: Cases for the mesh study of Condition XI.

Case	Mesh	$\Delta y_w/L(\times 10^{-5})$	L_z (mm)	$\Delta z/L(\times 10^{-3})$	Initial w
D1	$1152 \times 256 \times 512$	8	100	1.95	random
D2	$1600 \times 320 \times 360$	5	30	0.83	random

field for the 3-D simulation, and hence it is regarded as a part of case D1. It is obvious that the temporal convergence is achieved before $\bar{t} = 200$. The converged separation and reattachment positions are located at $x/L = 0.49$ and $x/L = 1.26$, respectively. Moreover, the converged 2-D results for cases D1 and D2 are compared in figure 3.22. As seen, the skin friction coefficient and wall Stanton number distributions are almost identical for the two cases. In addition, the skin friction coefficient on the flat plate upstream of separation agrees well with the theoretical prediction (Eq. 3.3). Therefore, it can be concluded that the mesh resolution in streamwise and wall-normal directions for case D1 is sufficient to capture the flow separation and surface heat transfer.

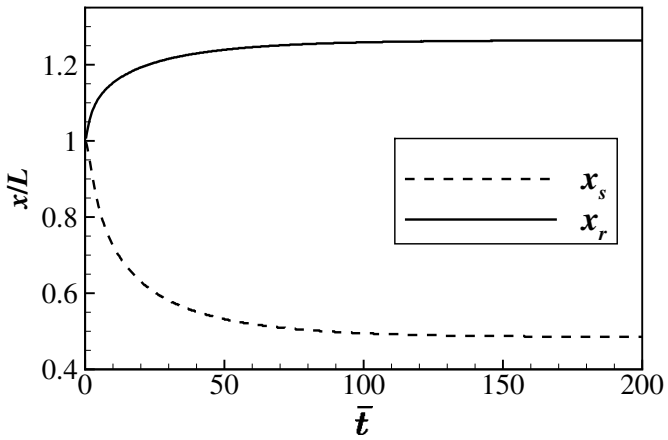


Figure 3.21: Temporal evolution of the separation and reattachment positions for the 2-D simulation of case D1.

For the 3-D simulations, streamwise vortices occur near reattachment associated with streamwise heat flux streaks on the wall. Figure 3.23 presents the wall Stanton number distribution at four instants of time for case D1. The initial flow field is generated at $\bar{t} = 0$ by duplicating the 2-D converged solution in spanwise direction. The three-dimensionality develops quickly, and distinct surface heat flux streaks are observed at $\bar{t} = 10$. The wall Stanton number distribution looks similar at $\bar{t} = 20$ and 50, implying the accomplishment of flow establishment and also the presence of an unsteady flow. In addition, the occurrence of a meandering reattachment line and the slight increase in the separation bubble length after a sufficient simulation period are consistent with case C4. However, the general spanwise wavelength of the heat flux streaks for case D1 is smaller than that

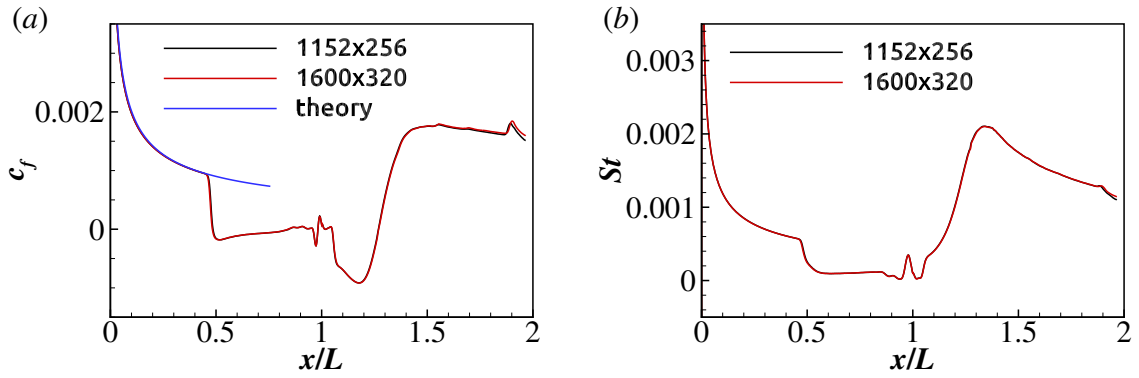


Figure 3.22: Streamwise distribution of (a) the skin friction coefficient and (b) the wall Stanton number for the converged 2-D results of cases D1 and D2. The theoretical value is calculated based on Eq. 3.3.

for case C4, which is discussed in detail in Chapter 4. Subsequently, the temporal history of the wall Stanton number at $x/L = 1.45$ and $z/L = 0.5$ is exemplarily shown in figure 3.24. It is apparent that the wall Stanton number starts to fluctuate from $\bar{t} = 5$ on. The fluctuation for case D1 occurs earlier than that for case C4 (see figure 3.14), which indicates that the three-dimensionality develops faster for case D1.

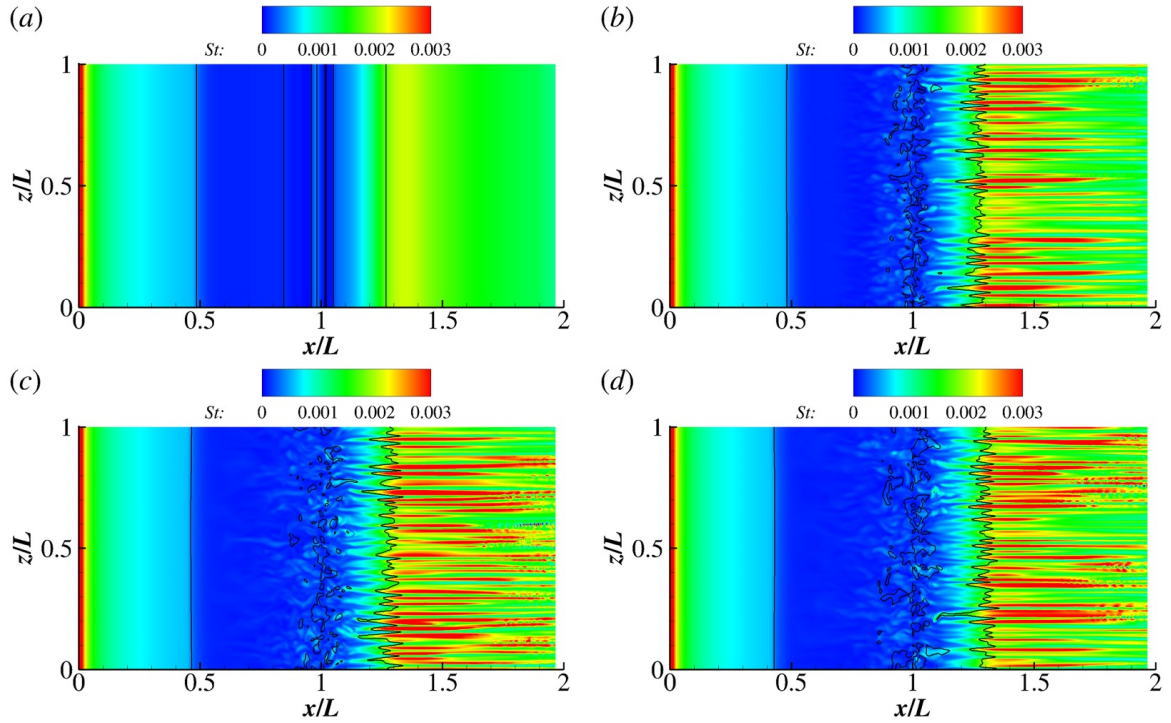


Figure 3.23: Wall Stanton number distribution (top view) for case D1 at different instants of time, a)-d) correspond to $\bar{t} = 0$, 10, 20, 50. Solid lines denote iso-lines of zero skin friction coefficient. Flow from left to right.

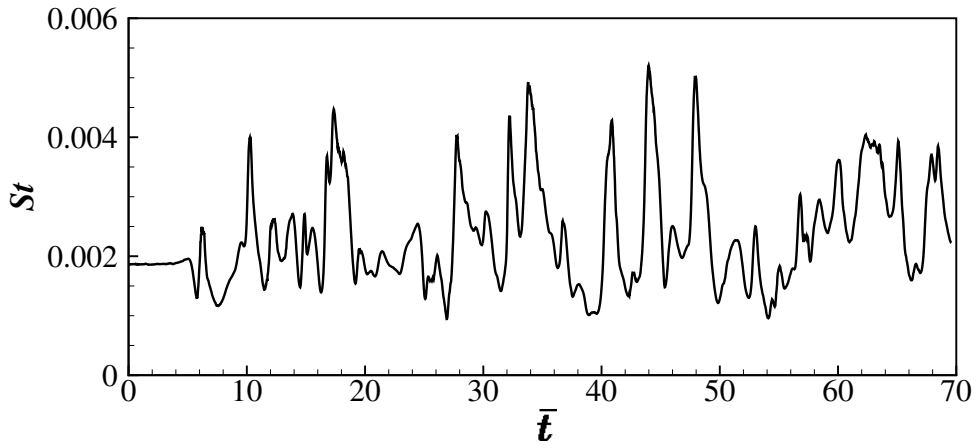


Figure 3.24: Temporal history of the wall Stanton number at $x/L = 1.45$ and $z/L = 0.5$ for case D1.

In order to further identify the temporal convergence to a quasi-steady state of the 3-D simulation, the temporal growth of σ_{St} (Eq. 3.8) and σ_w (Eq. 3.9) is analysed for case D1. Figure 3.25 shows the temporal growth of σ_{St} at $x/L = 1.45$. Similar to case C4, σ_{St} grows rapidly to its asymptotic level after an initial adaption. However, the required time period for this growth is shorter than that for case C4. It is seen that σ_{St} reaches its asymptotic level at about $\bar{t} = 15$. Next, the temporal growth of the spanwise velocity (σ_w) at $x/L = 1.05$ is shown in figure 3.26. The initial evolution is also characterised by an exponential growth, which ends at $\bar{t} = 6$. Note that σ_w has the largest quantity at $x/L = 1.05$ at the exponential growth stage. On the basis of the above discussions, it can be concluded that for case D1, the flow reaches the quasi-steady state prior to $\bar{t} = 20$.

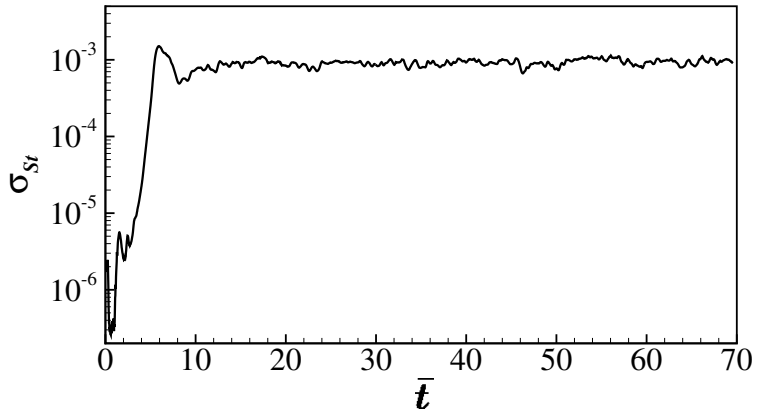


Figure 3.25: Temporal growth of the standard deviation of the spanwise Stanton number variation (Eq. 3.8) at $x/L = 1.45$ for case D1.

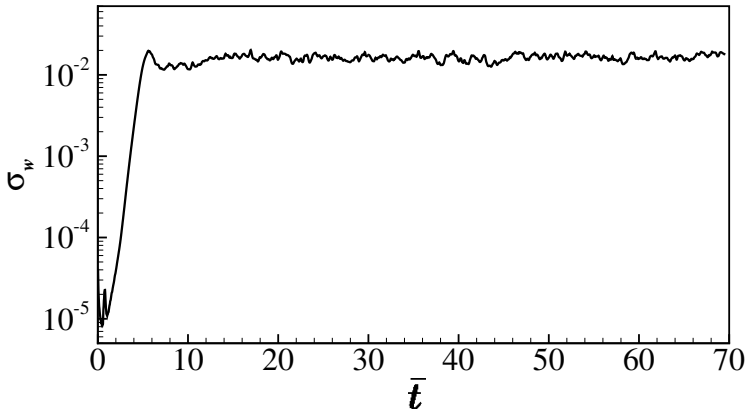


Figure 3.26: Temporal growth of the spanwise velocity (Eq. 3.9) at $x/L = 1.04$ for case D1.

The grid independence of the 3-D simulation for a certain instant of time is subsequently discussed. Figure 3.27(a) shows the wall Stanton number distribution at $\bar{t} = 10$ for case D2. On average, the spanwise wavelength of the heat flux streaks is 3 mm, which is consistent with case D1 (see figure 3.23) and comparable with the experimental observations ($3 \sim 5$ mm [78]). Figure 3.27(b) compares the spanwise variation of the wall Stanton number at $x/L = 1.45$ for cases D1 and D2. Note that the number of spanwise grid points per wavelength for cases D1 and D2 is approximately 17 and 36 respectively. The comparable amplitude and wavelength indicate that the mesh resolution for case D1 is sufficient to resolve the three-dimensionality. In summary, the temporal convergence and grid independence are demonstrated for the high Reynolds number case, for which a long-period simulation is also performed in order to further analyse the flow details (see Chapter 5).

3.5 Finite-span effects

In hypersonic experiments, the spanwise length of the model is usually limited by the size of facilities. For the flow on a compression ramp with a finite span, there is a flow leakage heading outwards in spanwise direction due to a favourable lateral pressure gradient [88–92]. As a result, finite-span effects lead to decreases in the separation bubble length and the peak pressure and heat flux [90, 92]. To reduce or avoid this leakage effect, one may introduce sidewalls or use a model with a large aspect ratio. Holden [88] proposed that a nominally two-dimensional compression ramp flow is achieved when a further increase in model span or adding sidewalls have no influences on the centre-line flow properties. In 3-D numerical simulations, using periodic boundary conditions in spanwise direction is generally equivalent to applying an infinite span. This could result in a discrepancy of the separation bubble size between the numerical results and experimental data due to

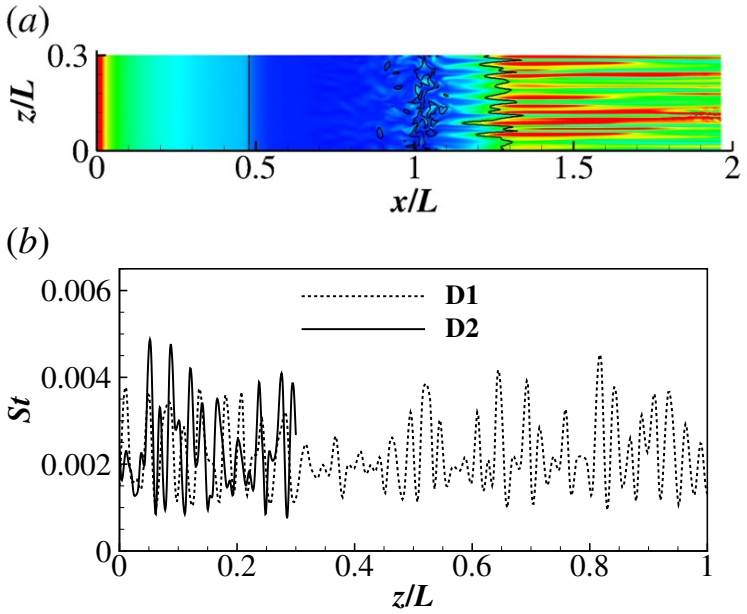


Figure 3.27: (a) Wall Stanton number distribution at $\bar{t} = 10$ for case D2. (b) Spanwise distribution of the wall Stanton number at $x/L = 1.45$ and $\bar{t} = 10$ for cases D1 and D2.

finite-span effects in experiments, as shown by Rudy et al. [89] and Grasso and Marini [90]. However, Rudy et al. [89] showed that by including the finite-span effects in the simulations, a good agreement with experimental data is obtained not only in terms of the extent of separation, but also the time required to establish the steady separated flow in this case.

To study whether experimental results are significantly influenced by finite-span effects, one may firstly compare the 2-D numerical solution of the compression ramp flow with experimental data. As shown in the previous section, when using periodic boundary conditions in spanwise direction, the separation bubble length for 3-D simulation does not deviate from the 2-D solution too much. Therefore, if the experimental results are not significantly affected by finite-span effects, they should be comparable to the 2-D simulation results. If not, then one may examine the finite-span effects by setting a similar boundary condition as suggested by Rudy et al. [89] at the sides of the compression ramp to allow a lateral spillage. This boundary condition is achieved as follows in the present thesis. On both sides of the compression ramp a buffer layer of five percent width is added allowing an interaction between the flow on the compression ramp and the free-stream. Outside the buffer layer, the free-stream flow conditions are prescribed on the spanwise ghost grid.

In the following, the experimental data obtained from Condition I and Condition XI [16, 78] are compared with the present DNS results, in an attempt to examine the finite-span

effects. Firstly, the streamwise distributions of the surface pressure coefficient and wall Stanton number for cases C4 and D1 (for which the ramp angle is 15°) are compared with experimental data in figures 3.28 and 3.29. Note that both c_p and St are time-averaged and taken on the symmetry plane in experiments and numerical simulations. It is obvious that the separation bubble size resulting from 3-D numerical simulations is in good agreement with that obtained in experiments. The pressure and heat flux levels also match well with the experimental results. It should be mentioned that the pressure induced by the viscous interaction from the leading edge compares well with the prediction of Eq. (3.2). Therefore, the deviation of the pressure coefficient upstream of separation may result from a limited lower resolution of the installed pressure transducers in the experiments because the pressure magnitude is very low. For the numerical simulation, although the physical domain has a spanwise length of 100 mm, the applied periodic boundary conditions mimic a model with an infinite span. In fact, the separation bubble length is not significantly affected by the spanwise length of the physical domain, as shown for cases C4 and C5. However, the width of the model used in experiments amounts to 200 mm, which is finite and two times of the flat plate length. Therefore, the favourable agreements shown in figures 3.28 and 3.29 indicate that finite-span effects have no significant influence on the flow field at least near the model centre plane for these two cases in the experiments.

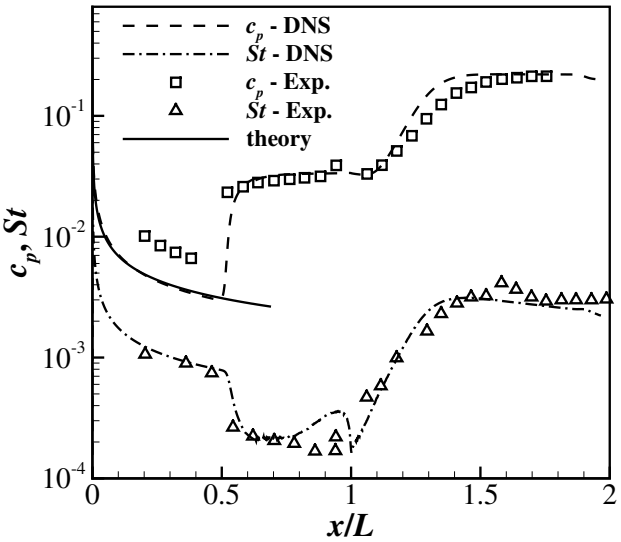


Figure 3.28: Streamwise distribution of the surface pressure coefficient and wall Stanton number on the symmetry plane for case C4 in comparison with the experimental data [16].

Next, a hypersonic compression ramp flow with a larger separation bubble than for the previous two cases is considered. This flow is achieved by using the same flow conditions as for case C4 (i.e., Condition I) but increasing the ramp angle to 20°. The ramp-induced shock creates a higher pressure rise which then causes a stronger flow separation. By

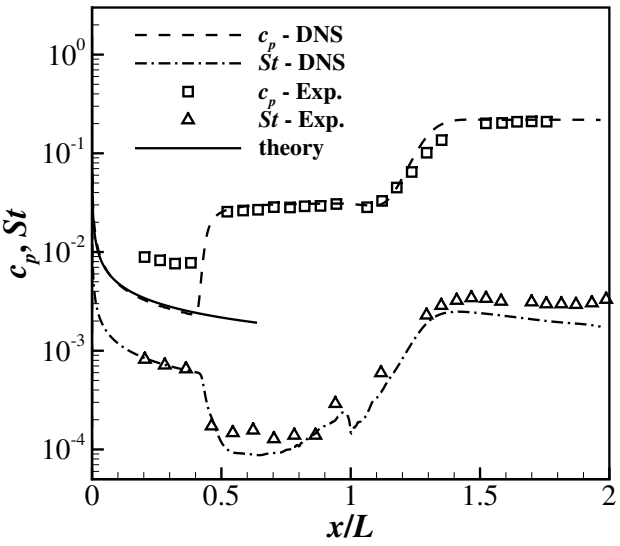


Figure 3.29: Streamwise distribution of the surface pressure coefficient and wall Stanton number on the symmetry plane for case D1 in comparison with the experimental data [78].

comparing the 2-D DNS results with experimental data [16] in figure 3.30, it can be seen that the separation bubble length observed in the experiments is smaller than that obtained by the 2-D numerical simulation. Note that the model width in experiments still amounts to 200 mm. Therefore, it is possible that the experimentally studied compression ramp flow was considerably affected by finite-span effects. To prove this, a 3-D DNS has been performed. For the boundary conditions in spanwise direction, one side of the computational domain represents a symmetry plane. The other side employs the same condition mentioned above to include finite-span effects. The spanwise length of the physical domain amounts to 100 mm. In this way, the total width is equivalent to the experimental model. The 3-D simulation covers 1.5 ms ($\bar{t} = 26$) in physical time during which corresponding to the numerical results a quasi-steady state is established. The comparison of the 3-D DNS results with experimental data is also shown in figure 3.30. Note that the data is taken on the symmetry plane for the time-averaged flowfield. It is apparent that by including finite-span effects in the numerical simulation, the separation bubble length is reduced when compared to the 2-D solution. The surface pressure and heat flux are in excellent agreement with experimental results. Therefore, it is proved that in the experiment performed for the present case, finite-span effects lead to a considerable lateral leakage and hence cause a notable decrease in the separation bubble size. In terms of the heat flux streaks downstream of reattachment, as shown in figure 3.31, their wavelength is approximately 5 mm, which agrees with experimental observations [16].

These studies demonstrate that for the considered flow conditions in the experiments the utilised model width (200 mm) is sufficient to ensures weak finite-span effects for a

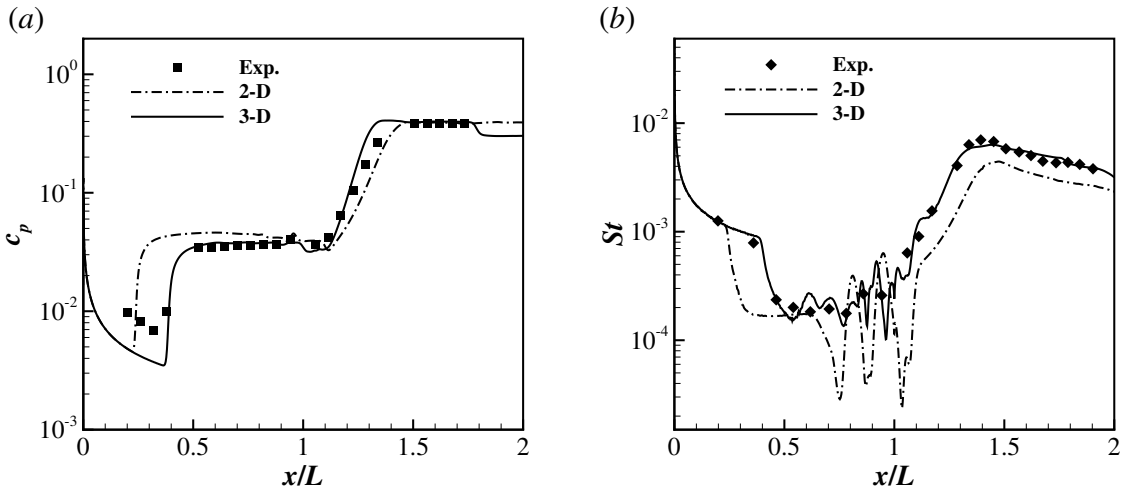


Figure 3.30: Streamwise distribution of the surface pressure coefficient and wall Stanton number for the validation case: Condition I, ramp angle = 20°, experimental data [16].

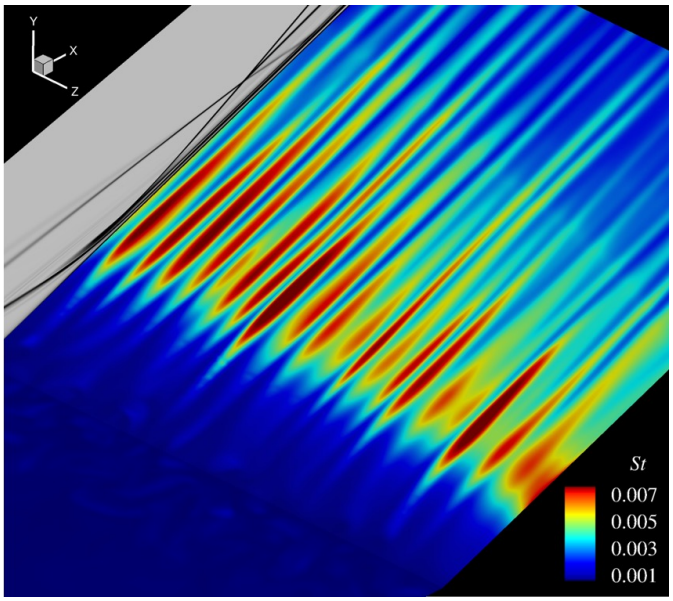


Figure 3.31: Surface Stanton number distribution for the validation case: Condition I, ramp angle = 20°.

deflection angle of 15°. But when the ramp angle is increased to 20 °, finite-span effects become important, which change the separation bubble size significantly. It is finally noted that the studies conducted in this section only aim to examine finite-span effects in experiments. For the main studies in the present thesis, we focus on the DNS results obtained by employing periodic boundary conditions in spanwise direction, which avoids the three-dimensional effects induced by lateral leakage.

3.6 Summary

In this chapter, a comprehensive mesh study is performed for a flat plate laminar boundary layer flow and several hypersonic compression ramp flows associated with shock wave/boundary layer interaction and streamwise vortices. Grid independence for the flat plate laminar boundary layer flow, the 2-D compression ramp flow, i.e., distributions of the skin friction coefficient, surface pressure coefficient and wall Stanton number and the streamwise vortices or the associated streamwise surface heat flux streaks (the wavelength and amplitude) is achieved. Temporal convergence is demonstrated for the 2-D (steady state) and 3-D (quasi-steady state) solutions. The numerical results agree well with not only documented experimental and numerical data but also theoretical predictions. Special emphasis is put on finite-span effects for the experimentally studied compression ramp flows. It is demonstrated that for cases C4 and D1, finite-span effects are weak, namely, the model width is sufficient to maintain a quasi-two dimensional flow. But for the case with a ramp angle of 20 ° (Condition I), finite-span effects lead to a considerable reduction in the separation bubble length due to lateral spillage effects.

4 Streamwise vortices in hypersonic compression ramp flows

This chapter discusses the occurrence of streamwise vortices in hypersonic compression ramp flows. The basic characteristics such as vortex structure are firstly shown for cases C4 and D1. Then, the surface heat transfer enhancement due to the presence of streamwise streaks is analysed in detail for the time-averaged flowfield. Subsequently, the wavelength of the surface heat flux streaks is further discussed. In addition to the comparison for cases C4 and D1, which have different Reynolds number, the effects of ramp angle are also briefly studied. Finally, an improved flow topology for the three-dimensional reattachment is proposed.

4.1 Basic characteristics

Figure 4.1 shows instantaneous compression ramp flows for cases C4 and D1. The separation bubble is highlighted by iso-lines of zero skin friction coefficient ($c_f = 0$). Note that multiple secondary separated bubbles are present near the corner for both cases, which are also indicated by the iso-lines of $c_f = 0$. The density gradient is shown at $z/L = 0$ to visualise the shock system and shear layer. The wall Stanton number distribution clearly visualises the streamwise streaks near and downstream of reattachment. Unlike the long streaks for case C4, some of the streaks for case D1 do not persist until the end of the ramp. They tend to break at the rear part of the ramp, indicating the presence of a transitional flow for the high Reynolds number case D1. It is noted that if the length of the ramp is long enough, the streamwise streaks will eventually breakdown to turbulence, as demonstrated in experiments [15, 16].

To characterise the vortex structure, figures 4.2 and 4.3 provide in-plane streamlines for a y-z plane for cases C4 and D1, respectively. The streamwise velocity contour is also shown to indicate the position of local boundary layer. Note that this plane is normal to the wall and its streamwise position is marked in figure 4.1. In the context of this thesis, y_n/L represents the normal distance to the wall. Counter-rotating vortex pairs can be observed above the wall. These vortices are oriented in streamwise direction. Due to the similar flow pattern to the classical Görtler vortices [26] and the presence of a streamline curvature near reattachment, these streamwise vortices are historically referred to as Görtler-like vortices [13, 15, 16, 52].

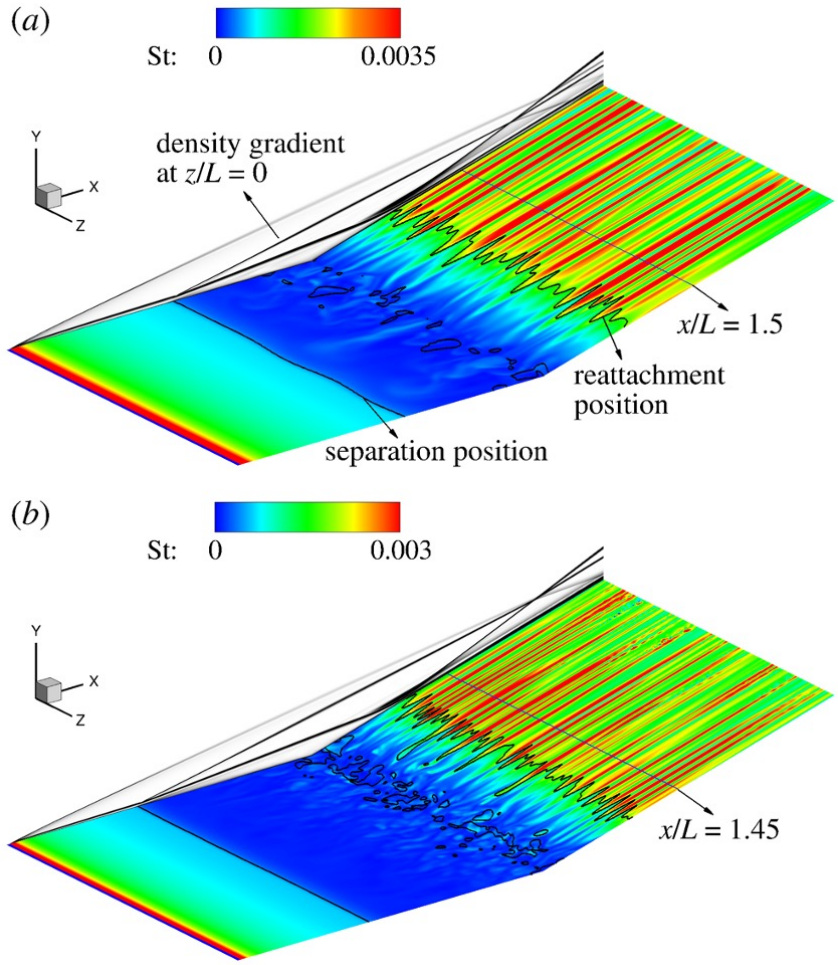


Figure 4.1: Instantaneous hypersonic compression ramp flow: (a) $M_\infty = 7.7$, $Re_{\infty,L} = 4.2 \times 10^5$, $\bar{t} = 100$ (case C4); (b) $M_\infty = 7.7$, $Re_{\infty,L} = 8.6 \times 10^5$, $\bar{t} = 60$ (case D1).

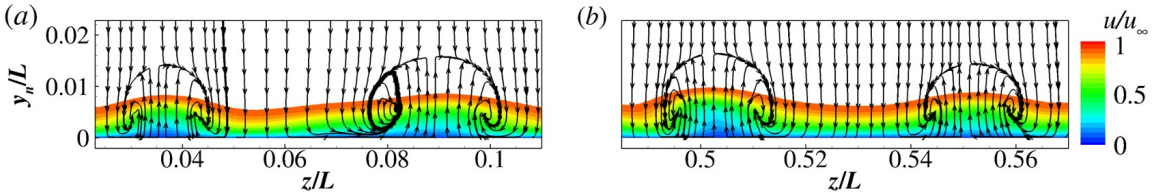


Figure 4.2: Vortex structure visualised by in-plane streamlines at $x/L = 1.5$ (case C4). Streamwise velocity contour u/u_∞ coloured for levels below 0.95 is also shown.

Several features of the vortices can be concluded from figures 4.2 and 4.3. First, the distance between two adjacent vortex pairs corresponds to the wavelength of the vortices. The shown vortices in figure 4.2(a, b) have a typical wavelength of 5.5 mm and 5.0 mm, respectively. In figure 4.3, the wavelength for the contiguous vortex pairs amounts to 3.8 mm, 3.5 mm and 3.3 mm, from left to right. Second, the height of the vortices is

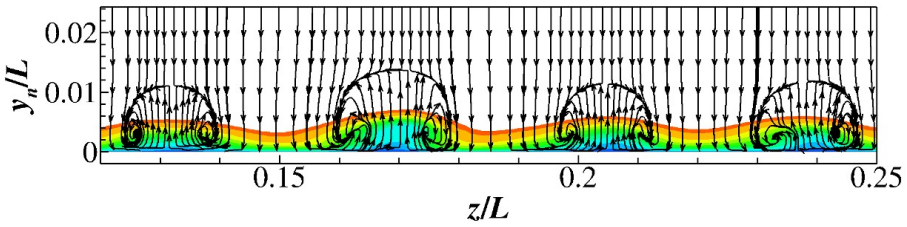


Figure 4.3: Vortex structure visualised by in-plane streamlines at $x/L = 1.45$ (case D1). Streamwise velocity contour u/u_∞ coloured for levels below 0.92 is also shown.

approximately 1.5 mm for case C4 and 1.2 mm for case D1, which is nearly twice of the local boundary layer thickness. It is noted that the edge of the boundary layer is identified by the criterion of $u = 0.99u_{\text{local}}$, where u_{local} is the local streamwise velocity outside the boundary layer, for instance, the value at $y_n/L = 0.02$. This criterion results in the boundary layer edge being at $u = 0.95u_\infty$ and $0.92u_\infty$ for cases C4 and D1, respectively. Third, the vortex structure can also be used to interpret the surface heat flux streaks, as discussed in Chapter 1. At the centre of a vortex pair, the flow is moving away from the wall, resulting in a lift-up of the boundary layer. Thus, the surface heat flux drops here (cold region). By contrast, in the region between two vortex pairs, the flow is impinging on the wall, leading to a thinning of the boundary layer and consequently a high surface heat flux region (hot region). Therefore, the spanwise heat flux variation is associated with the distribution of the streamwise Görtler-like vortices.

Last, the relatively irregular shape and the unequal spanwise wavelength of the vortices indicate a nonuniform distribution of the vortices in spanwise direction. The spanwise distribution of the surface heat flux streaks also clearly shows the nonuniformity (see figure 4.1). This nonuniformity has been often observed in experiments [13–17, 52] but rarely reported in numerical simulations. In the present study, as the numerically constructed leading edge is exactly sharp and straight in spanwise direction, the nonuniformity is thought to be independent of the leading edge geometry, which is also experimentally demonstrated by Matsumura et al. [53] and Roghelia et al. [16]. In fact, the flow upstream of separation is purely a 2-D flow. Therefore, this nonuniformity is supposed to originate from the separation bubble flow. As shown in Chapter 3, the fully developed separation bubble flow is unsteady, which might be responsible for the nonuniformity. The flow unsteadiness is extensively discussed in Chapter 5. In the present chapter, the time-averaged flow features are analysed in depth and compared to the instantaneous flow if necessary.

4.2 Surface heat transfer enhancement

Figure 4.4 shows the time-averaged compression ramp flow (obtained between $\bar{t} = 60 \sim 130$) for case C4. Compared to the instantaneous flow (see figure 4.1(a)), a decrease in the intensity of the surface heat flux is observed. Though the reattachment line is still meandering, its spanwise undulation is significantly weakened. These differences in the instantaneous and time-averaged behaviour indicate the presence of a strong flow unsteadiness. A comparison of the wall Stanton number for the instantaneous ($\bar{t} = 100$) and time-averaged flow is shown in figure 4.5, where the spanwise variation of the Stanton number at $x/L = 1.5$ is presented. It is apparent that the spanwise variation of the Stanton number for the instantaneous flow is much stronger than that of the time-averaged flow. In particular, the standard deviation (std) for the spanwise variation amounts to 8.9×10^{-4} for the instantaneous flow and 2.1×10^{-4} for the time-averaged flow. Note however, that the spanwise-averaged value is nearly the same for the instantaneous and time-averaged flow. As a result, the ratio of the standard deviation to the spanwise-averaged value amounts to 32.2% for the instantaneous flow and 7.6% for the time-averaged flow.

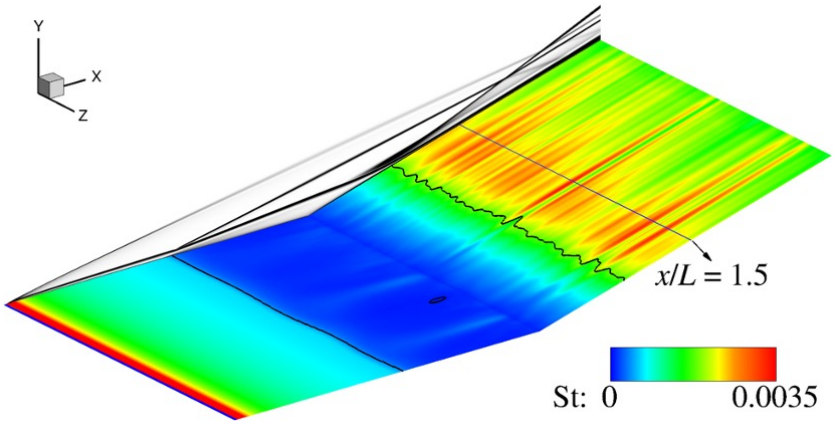


Figure 4.4: Time-averaged flow field for case C4. Wall Stanton number and density gradient is shown.

Figure 4.6 presents the streamwise distribution of the standard deviation for the spanwise Stanton number variation around the spanwise-averaged value. It is seen that compared to the time-averaged flow, a larger value of the standard deviation for the instantaneous flow holds both inside and downstream of the separation region. Downstream of the peak heating position, the magnitude of the standard deviation maintains nearly invariant in streamwise direction for both cases. This is expected as the streamwise streaks persist for a long distance on the ramp surface.

In terms of the heat transfer enhancement with respect to the 2-D solution, figure 4.7 compares the streamwise distribution of the spanwise-averaged wall Stanton number for the instantaneous and time-averaged flow with the 2-D flow. As aforementioned, the

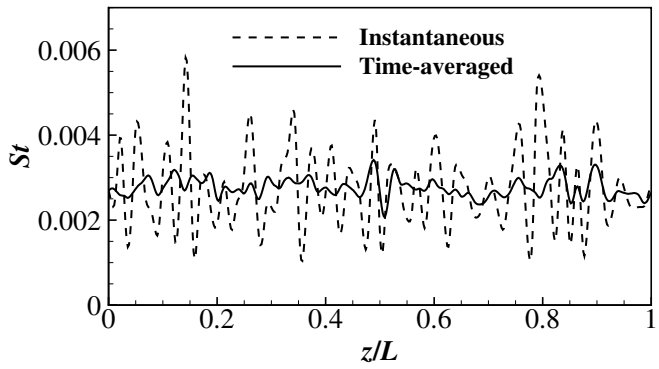


Figure 4.5: Spanwise variation of the wall Stanton number at $x/L = 1.5$ for the instantaneous and time-averaged flows (case C4).

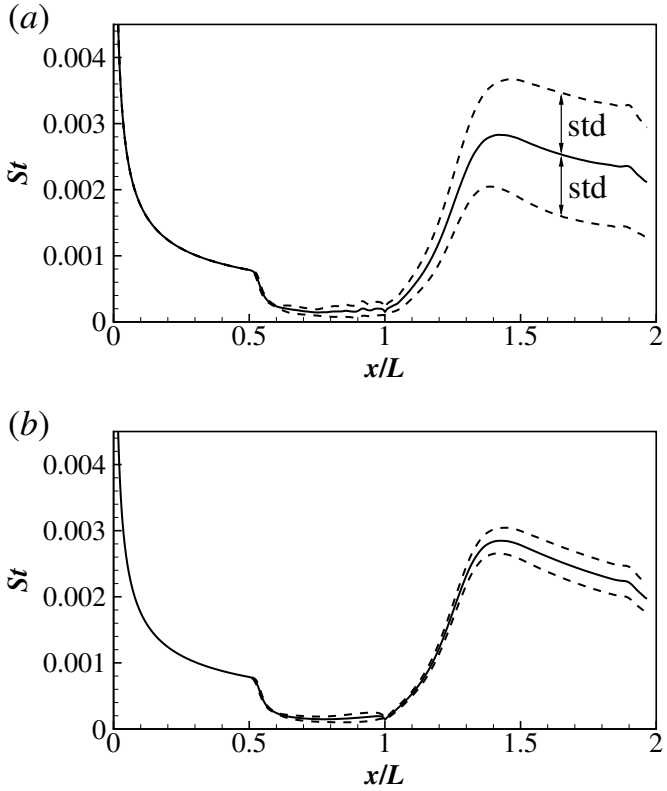


Figure 4.6: Streamwise distribution of the spanwise-averaged wall Stanton number (solid line) and the standard deviation of the spanwise variation (dashed lines) for (a) the instantaneous flow ($\bar{t} = 100$) and (b) time-averaged flow.

spanwise-averaged value is nearly the same for the instantaneous and time-averaged flow. However, the 3-D DNS solution yields a higher surface heat transfer downstream of reattachment than for the 2-D solution. For instance, the time-averaged quantity at $x/L = 1.9$ increases by 30% in comparison to the 2-D result. The discrepancy between the 2-D and

3-D solutions often leads to a failure in explaining experimental results on the basis of 2-D solutions especially when streamwise streaks are observed [15]. Moreover, the separation bubble length obtained from 3-D DNS slightly differs from that of the 2-D solution. Therefore, it is suggested that using a 2-D solution to study the compression ramp flow may cause significant deviations from the real situation.

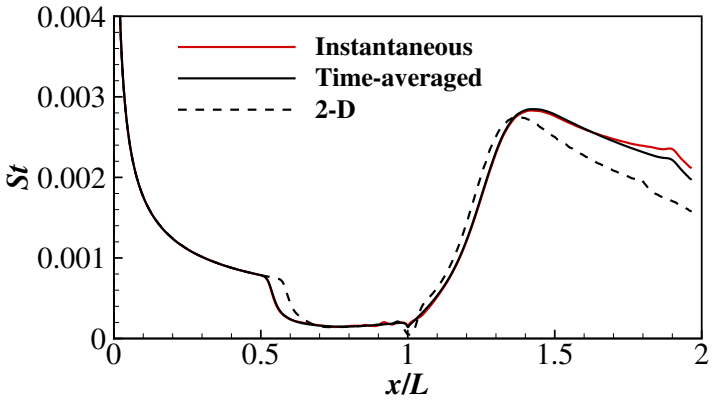


Figure 4.7: Streamwise distribution of the spanwise-averaged Stanton number for instantaneous and time-averaged flow in comparison with the 2-D solution (case C4).

Similar results can be found for the high Reynolds number case D1. The time-averaged flow ($\bar{t} = 30 \sim 70$) for case D1 is shown in figure 4.8, which also shows a lower heating level compared to the instantaneous flow (see figure 4.1(b)). The spanwise variation of the wall Stanton number at $x/L = 1.45$ is exemplarily shown in figure 4.9. The standard deviation for the instantaneous and time-averaged flow amounts to 8.2×10^{-4} and 1.8×10^{-4}, respectively. The ratio of the standard deviation to the spanwise-averaged value amounts to 34.7% for the instantaneous flow and 7.4% for the time-averaged flow. The streamwise distribution of the standard deviation is similar to that of case C4 (see figure 4.6) and is therefore not shown.

Figure 4.10 presents the heat transfer enhancement with respect to the 2-D solution for case D1. Similarly, the 3-D solution yields a larger separation bubble length and a stronger surface heat transfer downstream of reattachment, in comparison to the 2-D solution. For instance, the spanwise-averaged quantity at $x/L = 1.9$ for the time-averaged flow increases by 45% compared to the 2-D result, which means a stronger heat transfer enhancement than for case C4.

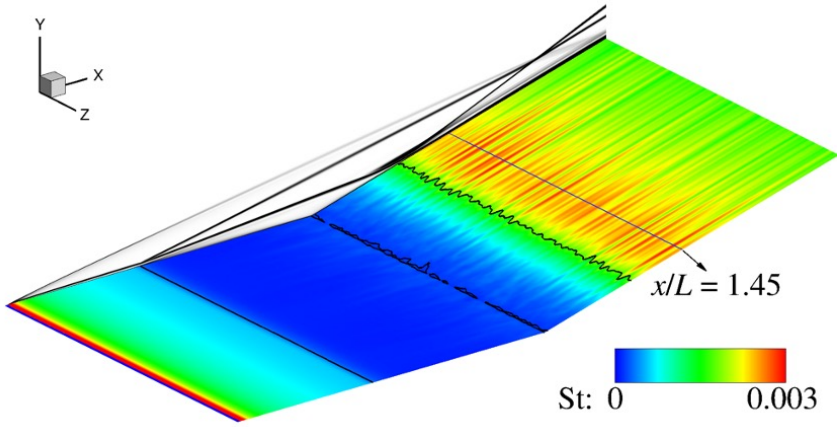


Figure 4.8: Time-averaged flow field for case D1, wall Stanton number and density gradient.

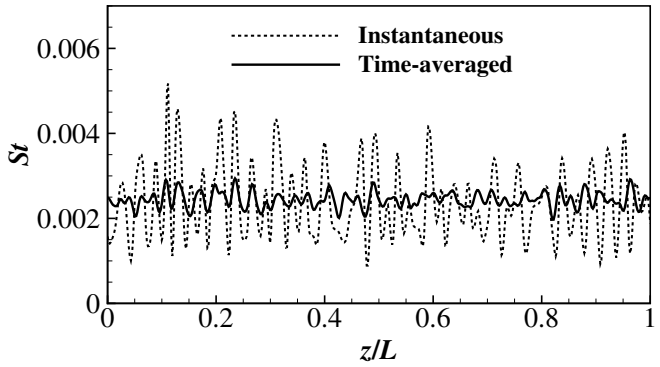


Figure 4.9: Spanwise variation of the wall Stanton number at $x/L = 1.45$ for the instantaneous and time-averaged flows (case D1).

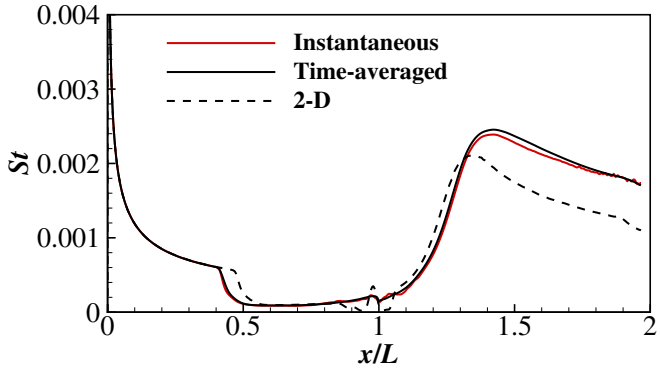


Figure 4.10: Streamwise distribution of the spanwise-averaged Stanton number for instantaneous and time-averaged flow in comparison with the 2-D solution (case D1).

4.3 Further remarks on the wavelength of the streamwise streaks

For the time-averaged flow (see, for example, figure 4.4), it seems that the wavelength of the streamwise heat flux streaks involves several length-scales. Instead of counting the number of streaks so as to estimate the average wavelength, a more exact wavelength can be found by performing a fast Fourier transform (FFT) of the wall Stanton number in spanwise direction. Firstly, the spanwise variation shown in figure 4.5 for the time-averaged flow is considered. The resulting power spectra density (PSD) as a function of the spanwise wavelength is shown in figure 4.11. The dominating wavelength is 5.9 mm. A second peak is located at 3.7 mm. These two wavelengths are close to the average wavelength for the instantaneous flow (4.2 mm) shown in figure 4.1(a) and are consistent with the experimental observations [16]. Apart from the small-wavelength components, two energetic components are present in the large-wavelength region. The associated wavelengths are 25 mm and 34 mm.

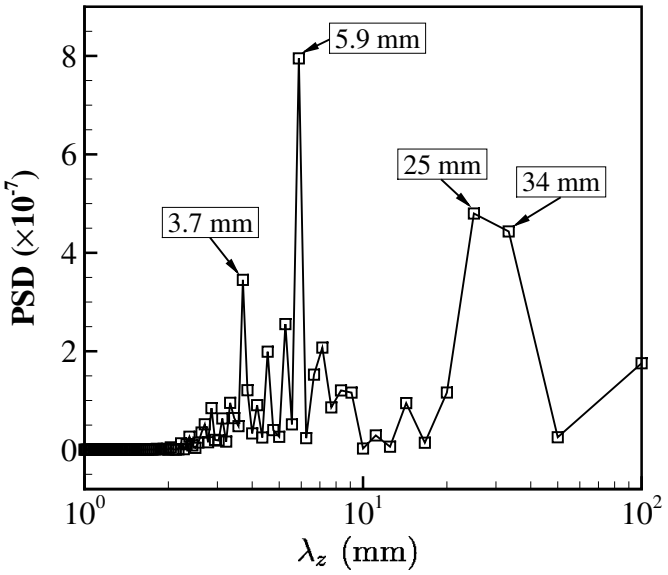


Figure 4.11: Power spectra density as a function of wavelength for the spanwise variation of the wall Stanton number at $x/L = 1.5$ for the time-averaged flow (case C4).

To understand the reason of the occurrence of the large wavelengths, the distribution of the spanwise velocity field in the time-averaged flow is shown in figure 4.12. It is apparent that large-scale spanwise periodicity exists in the separation bubble flow. This flow structure is typical of vortical cells moving flow away from the wall at the centre of a vortex pair (upwash) or towards the wall at the position between two vortex pairs (downwash). Their wavelengths can be estimated from figure 4.12(b), which are 26 mm,

42 mm and 32 mm from left to right. Therefore, the large wavelengths identified by FFT for the downstream heat flux streaks match the wavelength for the first and third vortical cells in the separation bubble, which indicates that the large-scale periodic structure in the separation bubble flow has an influence on the formation of the downstream heat flux streaks. It is noted that the flow structure shown in figure 4.12 resembles the shape of the global unstable mode found by Sidharth et al. [44] for a separated flow over a double wedge. It is therefore possible that the large-scale structure found in the separation bubble originates from its intrinsic instability. By performing a global stability analysis for the 2-D base flow of case C4, Cao et al. [93] found a stationary unstable mode with a wavelength of 34 mm in the separation bubble. Its wavelength agrees well with the average wavelength of the three vortical cells in the separation bubble. This agreement reveals that the instability in the separation bubble flow contributes to the formation of downstream streaks. It should be noted that the low wavelengths for the streaks may also be influenced by the instability of the separation bubble flow, and the centrifugal instability may amplify the disturbances generated in the separation bubble flow. It is hard to separate the effects of different mechanisms for the present flow. Therefore, the wavelength selection mechanism is still an open question.

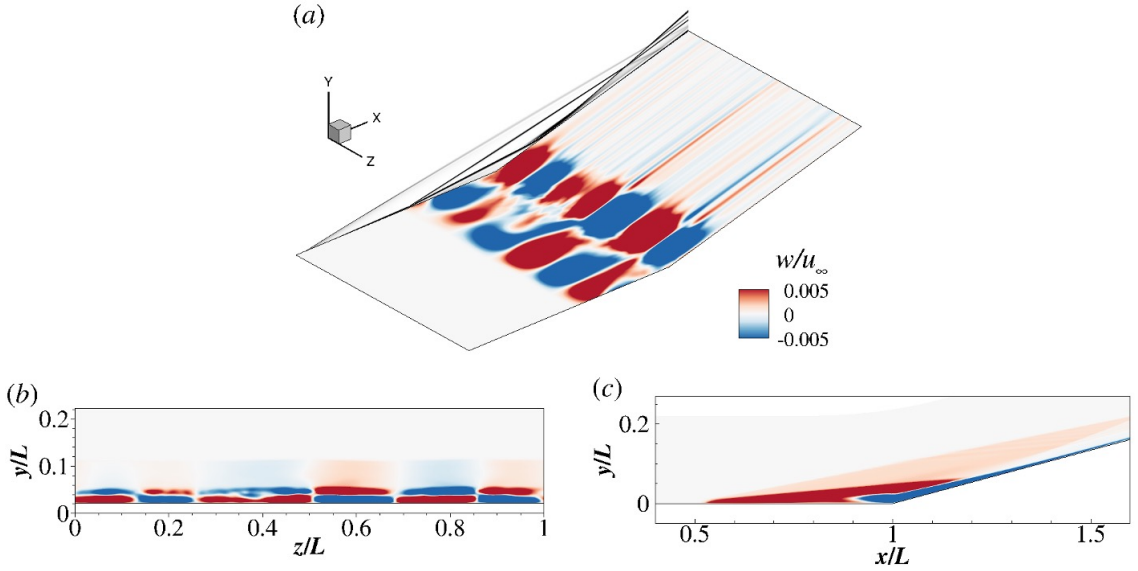


Figure 4.12: Time-averaged distribution of the spanwise velocity field on different planes (case C4): (a) wall-parallel plane at $y_n/L = 0.009$. (b) z-y plane at $x/L = 1.04$. (c) x-y plane at $z/L = 0.6$. The density gradient at $z/L = 0$ is shown in (a) to highlight the position of the separation bubble.

For the high Reynolds number case D1, figure 4.13 shows the results of FFT for the spanwise variation of the wall Stanton number at $x/L = 1.45$ for the time-averaged flow (see figure 4.9). It is seen that the dominating wavelengths concentrate on a small-wavelength region, ranging from 2.6 mm to 4.0 mm, which agrees well with the experimental results [78] ($3 \sim 5$ mm). Unlike case C4, large-wavelength components seem to be absent in this

case. To verify the influence of the separation bubble flow, the spanwise velocity field on the y-z plane at $x/L = 1.04$ for the time-averaged flow is shown in figure 4.14. In contrast to figure 4.12(b), there is no distinct spanwise periodic structure in the separation bubble flow. In general, the wavelength of the streamwise heat flux streaks for case D1 is smaller than that of case C4 both for the instantaneous and time-averaged flow, which means that an increase in the free-stream unit Reynolds number leads to a decrease in the wavelength.

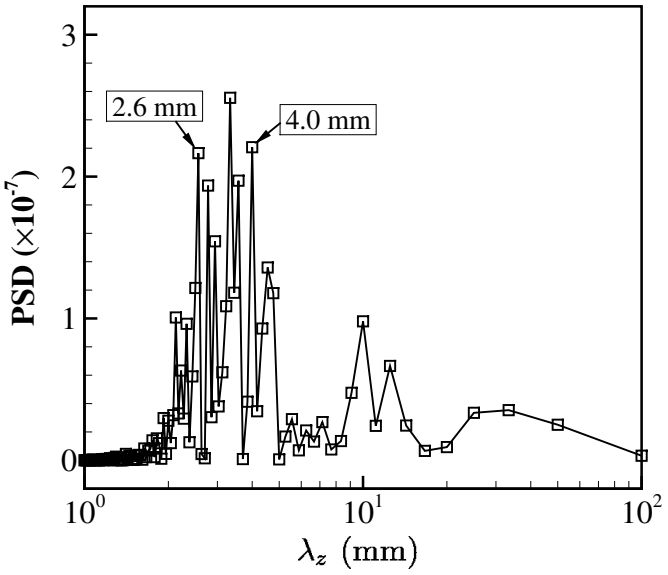


Figure 4.13: Power spectra density as a function of wavelength for the spanwise variation of the wall Stanton number at $x/L = 1.45$ for the time-averaged flow (case D1).

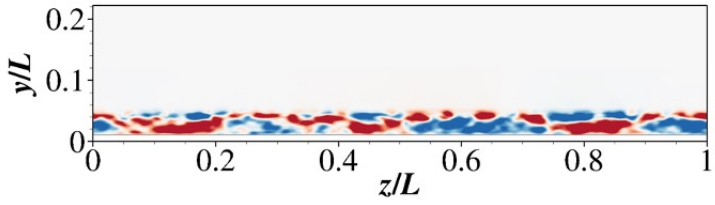


Figure 4.14: Time-averaged distribution of the spanwise velocity field on the z-y plane at $x/L = 1.04$ (case D1). The same legend as figure 4.12 is used here.

4.4 Effects of ramp angle

To investigate the influence of the ramp angle, two cases (D3 and D4) involving the same flow conditions as case D1 (i.e., Condition XI) but different ramp angles are considered,

Table 4.1: Cases for investigating the effects of ramp angle.

Case	Mesh	M_∞	$Re_{\infty,L}$	Ramp angle	L_z (mm)	Spanwise BC
D3	$1152 \times 256 \times 512$	7.7	8.6×10^5	20°	100	Periodic
D4	$1152 \times 256 \times 512$	7.7	8.6×10^5	25°	100	Periodic

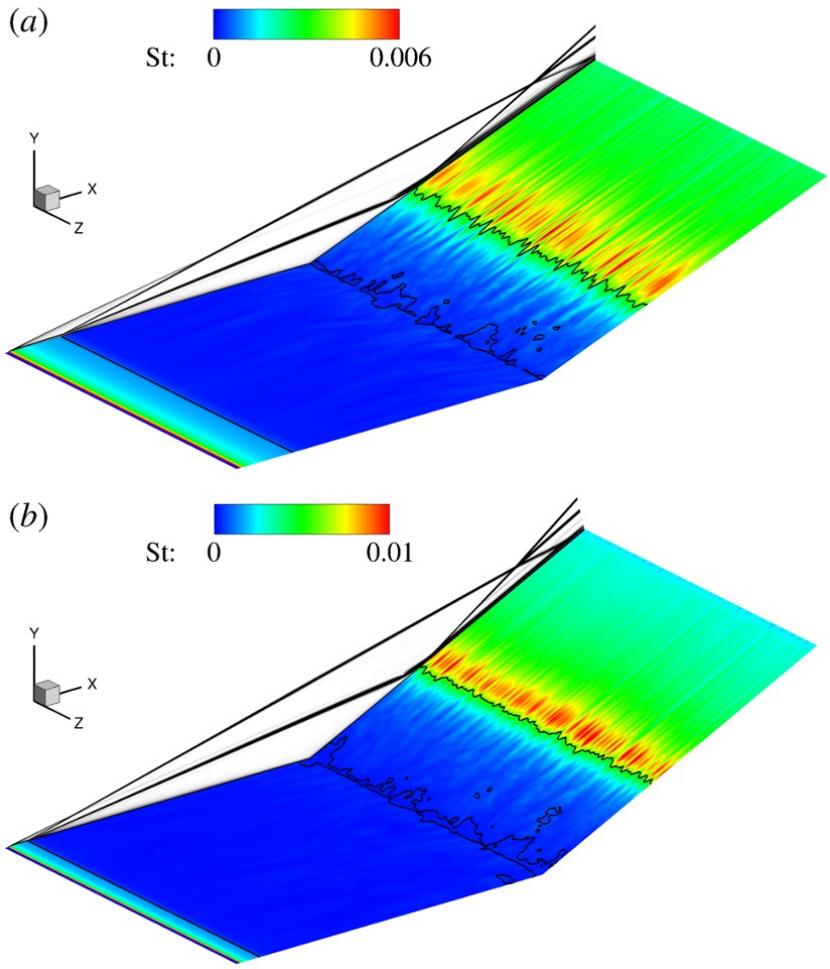


Figure 4.15: Time-averaged flow field for (a) case D3 and (b) case D4. The density gradient is shown for the plane at $z/L = 0$. Solid lines on the surface correspond to $c_f = 0$.

as shown in Table 4.1. The ramp angle for cases D3 and D4 is 20°and 25°, respectively. The chosen ramp angles have been considered in experiments [78]. Though the width of the compression ramp model used in experiments amounts to 200 mm, the physical domain for the numerical simulation has a width of 100 mm. Note however, that periodic boundary conditions are applied in spanwise direction, which is necessary in order to make

a direct comparison with case D1. On the other hand, using periodic boundary conditions exclude the finite-span effects that may appear in experiments.

The increase in the ramp angle leads to a stronger SWBLI, inducing a very large separation bubble. Figure 4.15 presents the time-averaged flow fields for cases D3 and D4. It is noted that the temporal development of three-dimensionality for the two cases is very fast, and the flow reaches a quasi-steady state at about $\bar{t} = 20$. The time-averaging is processed between $\bar{t} = 20 \sim 30$. This time period enables a qualitative comparison of the time-averaged flow behaviour with case D1 because it covers several cycles of the unsteady flow. As an example, a temporal history of the wall Stanton number at $x/L = 1.45$ and $z/L = 0.5$ for case D4 is shown in figure 4.16.

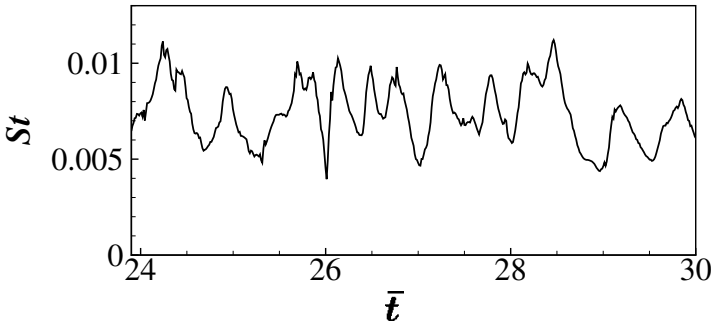


Figure 4.16: Temporal history of the wall Stanton number at $x/L = 1.45$ and $z/L = 0.5$ for case D4.

The comparisons of the time- and spanwise-averaged skin friction coefficient and wall Stanton number for cases D1, D3 and D4 are presented in figure 4.17. Compared to case D1, the separation bubble length increases by 37% for case D3 and 52% for case D4. Immediately downstream of reattachment, both the skin friction coefficient and wall Stanton number increase with ramp angle. In comparison with case D1, the peak heating level rises by 94% for case D3 and 249% for case D4. This is mainly due to the increase in the flow deflection angle at the reattachment as well as the heating enhancement associated with the streamwise vortices, as shown below.

Figure 4.18 presents the spanwise variation of the wall Stanton number at the peak heating position ($x/L = 1.4$) for cases D3 and D4. The instantaneous value is taken at $\bar{t} = 30$. For case D3, the ratio of the standard deviation to the spanwise-averaged value amounts to 30.2% for the instantaneous flow and 11.8% for the time-averaged flow. For case D4, the ratio of the standard deviation to the spanwise-averaged value amounts to 30.6% for the instantaneous flow and 9.8% for the time-averaged flow. Concerning the spanwise heat flux variation in the time-averaged flow for the considered cases (i.e., C4, D1, D3 and D4), the relative standard deviation of the Stanton number varies from 7% to 12% in the vicinity of the peak heating location. These values are consistent with the experimental measurements [78].

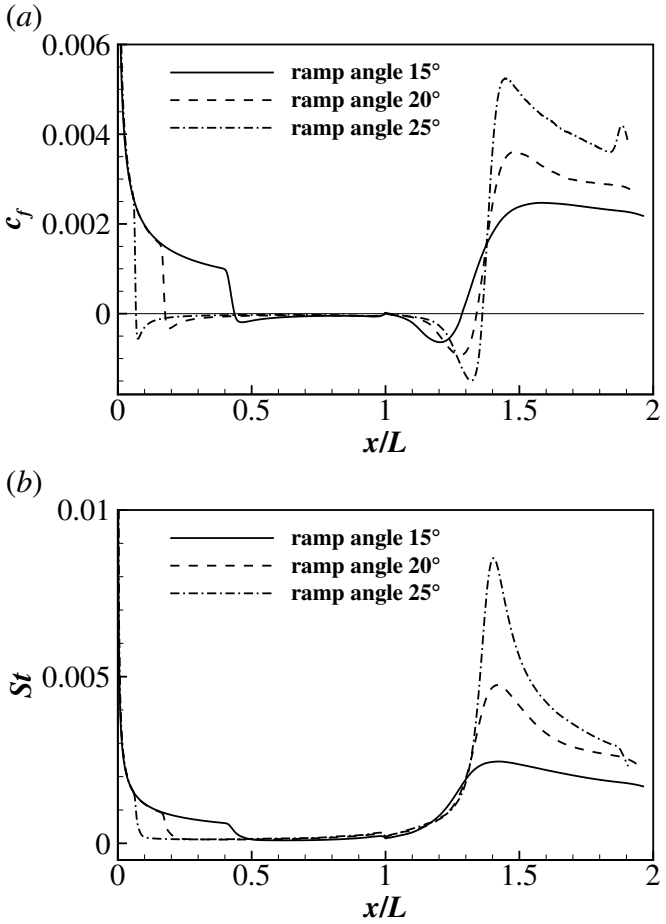


Figure 4.17: Streamwise distribution of the time- and spanwise-averaged (a) skin friction coefficient and (b) wall Stanton number for cases D1, D3 and D4.

The heat transfer enhancement with respect to the 2-D flow is subsequently discussed. Figure 4.19 shows the streamwise distribution of the spanwise-averaged wall Stanton number for the instantaneous and time-averaged flows in comparison with the 2-D flow. For cases D3 and D4, the peak Stanton number for the time-averaged flow rises by 54% and 87% respectively, compared to the 2-D flow. In summary, for the considered cases, the wall Stanton number increment from 2-D to 3-D flow can reach up to 87% downstream of reattachment, and the increment goes up with increasing unit Reynolds number and ramp angle.

In terms of the wavelength of the surface heat flux streaks for the time-averaged flow, the resulting spectra from FFT shows that the dominant wavelength is about 2.8 mm both for cases D3 and D4. This value is close to the typical wavelengths for case D1 (see figure 4.13). It means that for the considered flow condition (Condition XI), the wavelength of the streamwise vortices is insensitive to the selected ramp angles. This is also consistent with the experimental observations [16, 78].

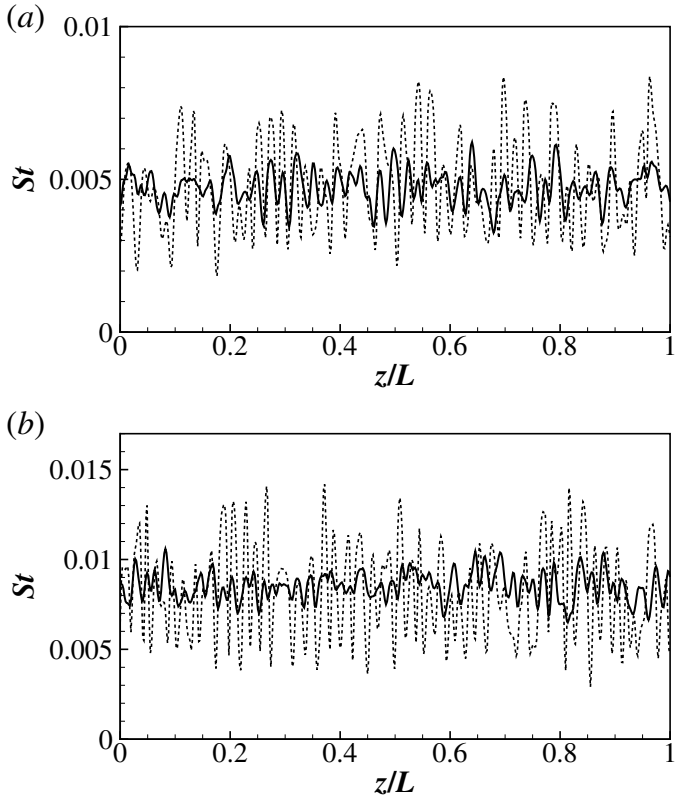


Figure 4.18: Spanwise distribution of the wall Stanton number at $x/L = 1.4$ for (a) case D3 and (b) case D4. Dashed line corresponds to the instantaneous flow ($\bar{t} = 30$) and solid line to the time-averaged flow.

4.5 Three-dimensionality near reattachment

Three-dimensional flow reattachment is often encountered in compression ramp flows. Ginoux [12] and Inger [94] proposed a typical topology of the reattaching flow, as shown in figure 4.20(a). A straight line normal to the streamwise direction represents the reattachment line, along which a series of singularities (nodes and saddle points) are evenly distributed. All streamlines originate from nodes moving towards saddle points. However, for the compression ramp flows considered here, the reattachment line is not straight, but meandering, as can be seen in figure 4.1. This is attributed to the spanwise undulation of the reattaching shear layer and the associated streamwise vortices. Figure 4.20(b) schematically illustrates the corresponding limiting streamlines in the reattachment region. The position of nodes (N) and saddle points (S) are shifted in streamwise direction, with saddle points located downstream of nodes. This configuration is confirmed by the surface streamline configuration shown in figure 4.20(c) and was also reported by Klioutchnikov and Olivier [54] and Kavun et al. [62].

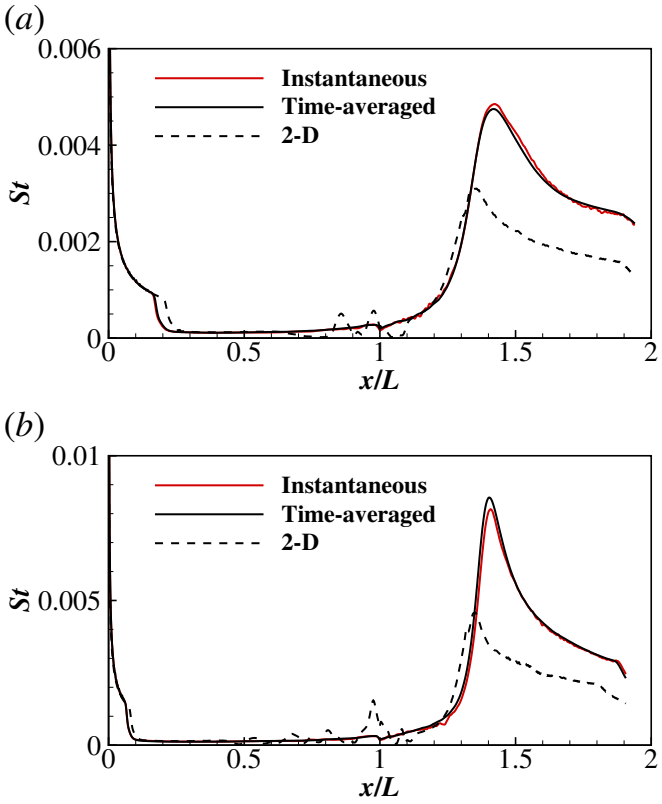


Figure 4.19: Streamwise distribution of the spanwise-averaged Stanton number for the instantaneous ($\bar{t} = 30$) and time-averaged flow in comparison with the 2-D solution for (a) case D3 and (b) case D4.

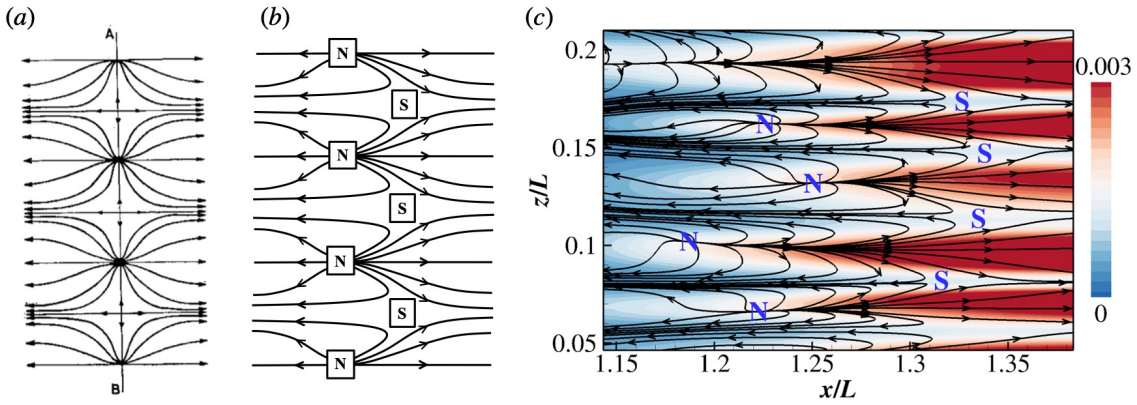


Figure 4.20: Schematic configuration of local streamlines in the reattachment region proposed by (a) Ginoux [12] and (b) the present thesis. (c) Streamlines on a near-wall plane ($y_n/L = 0.0008$) embedded in the wall Stanton number contour for case D1. N and S denote nodes and saddle points, respectively.

Due to this type of reattachment, the downstream evolution of the vortices and the heat flux streaks are enhanced. For instance, downstream of a saddle point, the flow is

forced to coalesce, resulting in a lift-up effect of the attached boundary layer. Thus, a cold region forms immediately downstream of this saddle point, as clearly seen in figure 4.20(c). Meanwhile, a hot region forms downstream of a node. This feature is present in all cases and at all instants of time. Therefore, it is proposed that the meandering flow reattachment enhances the evolution of the three-dimensional shear flows and the streamwise vortices over the compression ramp.

4.6 Summary

The basic characteristics of the streamwise vortices and streaks in hypersonic compression ramp flows are discussed in this chapter. For the considered cases, counter-rotating streamwise-oriented vortices occur downstream of reattachment and are more or less uniformly distributed in spanwise direction. The associated surface heat flux streaks are analysed in detail for the flows with different Reynolds numbers and ramp angles. For the time-averaged flows, the spanwise variation of the wall Stanton number with respect to the spanwise-averaged value varies from 7% to 12% in the vicinity of the peak heating location. However, the spanwise variation can reach up to 35% for the instantaneous flows. In addition, the heat transfer enhancement due to the 3-D effects is significant downstream of reattachment. With respect to the 2-D solution, the spanwise-averaged wall Stanton number reaches up to 87%, and the increment goes up with increasing free-stream unit Reynolds number and ramp angle.

In general, the wavelength of surface heat flux streaks for the high Reynolds number case is smaller than that of the low Reynolds number case. However, for the considered flow conditions, the wavelength of the streamwise streaks is insensitive to the selected ramp angles. Furthermore, the presence of the large-scale wavelengths in the time-averaged flow of case C4 suggests that the instability in the separation bubble flow contributes to the formation of the downstream streaks.

The three-dimensional flow reattachment is characterised by a meandering reattachment line long which saddle points are located downstream of nodes. This flow reattachment topology enhances the evolution of the three-dimensionality in the downstream attached flows.

5 Unsteady effects in laminar separated hypersonic compression ramp flows

In the experiments studying separated hypersonic compression ramp flows, streamwise streaks are often observed downstream of reattachment. However, the utilised flow visualisation techniques in the experiments (e.g. oil flow visualisation, infrared imaging, temperature sensitive paint) usually captures the time-averaged behaviour of the flow, and thus instantaneous flow features are omitted. The numerical simulations performed in the present thesis demonstrate a highly unsteady flow field for the considered compression ramp flows. In this chapter the unsteady effects in the compression ramp flow for cases C4 and D1 are analysed. The spatio-temporal distribution of the surface heat flux is firstly studied, followed by an analysis of the unsteady flow features near reattachment. Subsequently, the unsteady separated flow is examined by using dynamic mode decomposition in an attempt to find out the origin of the flow unsteadiness.

5.1 Unsteady effects for a low Reynolds number case

5.1.1 Spatio-temporal distribution of the surface heat flux

As shown in Chapter 3, a quasi-steady state is achieved at about $\bar{t} = 50 \sim 60$ for case C4, and the fully established flow is unsteady both inside and downstream of the separation bubble. In the following, statistical analyses are carried out to characterise the unsteady behaviour of the surface heat flux downstream of reattachment. As an example, figure 5.1 shows the temporal history of the wall Stanton number between $\bar{t} = 60 \sim 130$ for case C4, which is adapted from figure 3.14.

Considering the temporal fluctuation of the surface heat flux at a certain position, its relative standard deviation (RSD) can be determined as follows:

$$\widehat{St} = \frac{\sqrt{\frac{1}{N}\sum_{i=1}^{N}(St_i - \overline{St})^2}}{\overline{St}} \tag{5.1}$$

where $\overline{St}$ denotes the time-averaged value for the considered position, and N is the number of sampling points. The relative standard deviation $\widehat{St}$ for all spanwise positions at $x/L = 1.5$ is presented in figure 5.2. It is clear that $\widehat{St}$ is not constant in spanwise

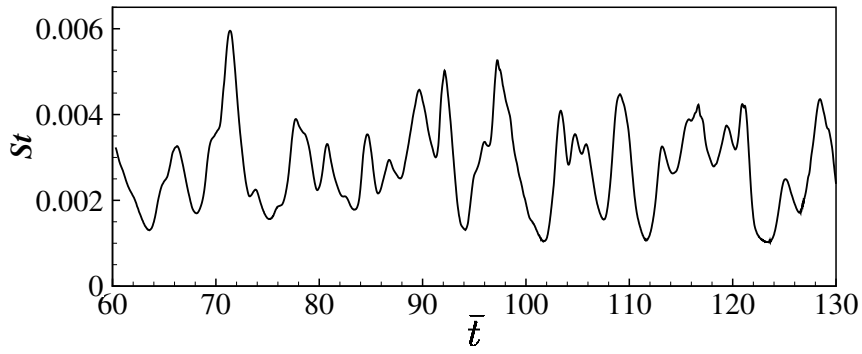


Figure 5.1: Temporal history of the wall Stanton number at $x/L = 1.5$ and $z/L = 0.5$ (case C4).

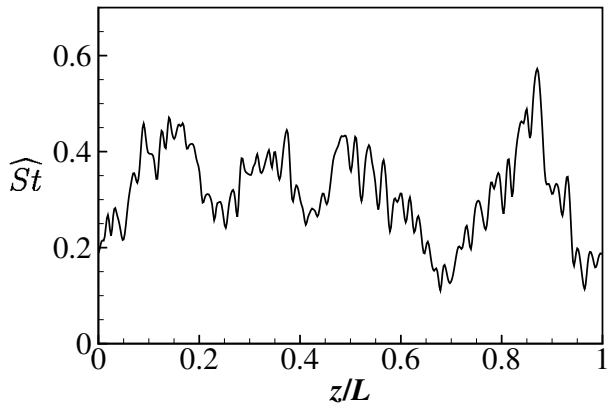


Figure 5.2: Relative standard deviation of the wall Stanton number for all spanwise positions at $x/L = 1.5$ (case C4).

direction. It is noted that this spanwise variation is related to the coherent structure shown in figure 4.12. For example, the strongest fluctuation has a $\widehat{St}$-value of 57% and is located at $z/L = 0.87$, corresponding to the upwash position in a vortex pair. However, the lowest $\widehat{St}$ is found at $z/L = 0.68$, corresponding to the downwash position between two vortex pairs (see figure 4.12(b)). This result indicates a direct influence of the separation bubble flow on the downstream heat flux fluctuation, which suggests that the unsteadiness in the reattached flow may be traced back to the separation bubble.

To identify a possible transport direction of the flow unsteadiness, a two-point spatio-temporal correlation is employed to evaluate the fluctuation quantities of the wall Stanton number ($St' = St - \overline{St}$):

$$R_{nm}(\tau) = \frac{\overline{St'_n(t) \cdot St'_m(t+\tau)}}{\sqrt{\overline{St'^2_n}} \cdot \sqrt{\overline{St'^2_m}}}, \tag{5.2}$$

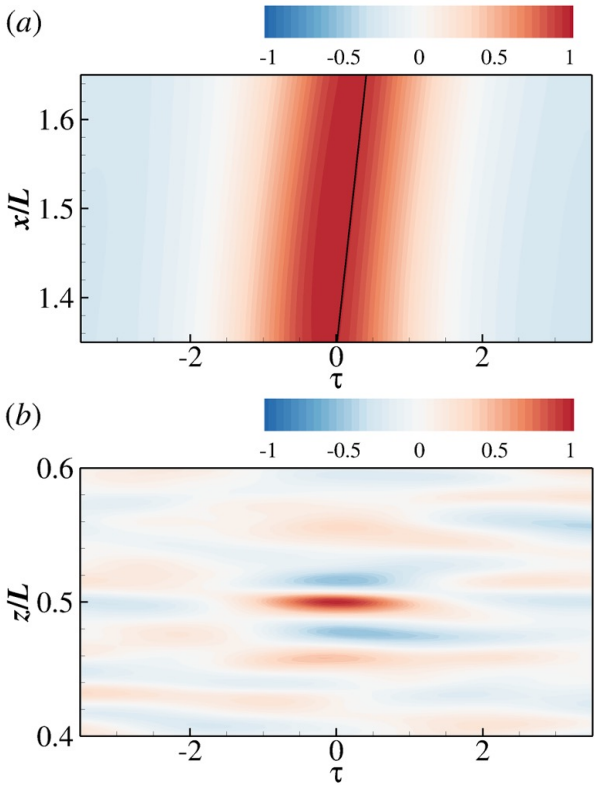


Figure 5.3: Two-point temporal correlation maps for the wall Stanton number in (a) streamwise direction and (b) spanwise direction. Reference point is located at $x/L = 1.5$, $z/L = 0.5$ (case C4).

where the subscript n denotes the reference point: $x/L = 1.5$, $z/L = 0.5$; m corresponds to the position varying in streamwise or spanwise direction, and τ is the time delay.

Figure 5.3 shows the calculated correlation maps. It is apparent that a strong correlation exists in streamwise direction, whereas the correlation in spanwise direction is quite weak. It means that the primary propagation direction of the unsteadiness is in streamwise direction. The linear slope of the main structure shown in figure 5.3(a) by the solid black line indicates the travelling speed of the unsteadiness, which is evaluated approximately by $0.7u_\infty$.

In terms of the fluctuation frequency, the power spectra density of the wall Stanton number signal shown in figure 5.1 is firstly considered. Welch's method [95] is employed for the spectral estimation with seven segments and 50% overlap. A Hamming window is used for weighting the data on each segment prior to FFT processing. The above setting yields the length of an individual segment being $17.5L/u_\infty$. The resulting PSD is shown in figure 5.4(a). It is seen that the surface heat flux signal has a broadband low-frequency feature, and the dominant nondimensional frequencies (fL/u_∞) are lower than 1 and approximately centred at $fL/u_\infty = 0.15$.

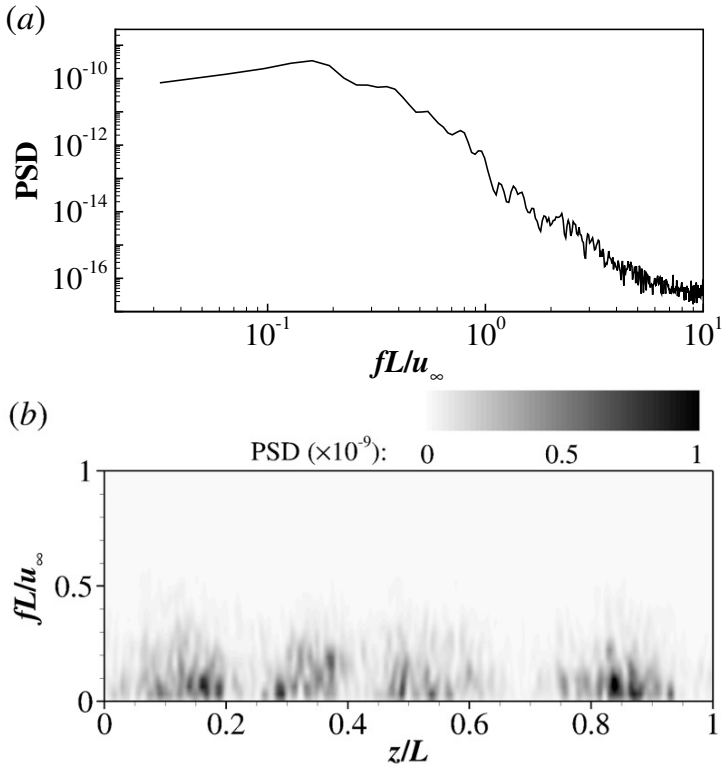


Figure 5.4: (a) Power spectra density of the wall Stanton number signal at $x/L = 1.5$ and $z/L = 0.5$. (b) Power spectra density map for all spanwise positions at $x/L = 1.5$.

Figure 5.4(b) provides the PSD contour for the wall Stanton number by considering all spanwise positions. The low-frequency characteristic holds at all spanwise positions, though a spanwise variation of amplitude exists. In general, groups of high amplitude are present at certain spanwise positions. This is consistent with the spanwise variation of the relative standard deviation shown in figure 5.2.

5.1.2 Unsteady features at flow reattachment

Since the unsteadiness propagates in streamwise direction, it is necessary to study the unsteadiness at flow reattachment. Figure 5.5 shows the temporal history of the spanwise-averaged reattachment position and the particular reattachment position on the symmetry-plane ($z/L = 0.5$), in comparison with the wall Stanton number signal. Unlike the pulsation of the reattachment point at $z/L = 0.5$, the spanwise-averaged reattachment point is nearly invariant, indicating a steady sate for the spanwise-averaged separation bubble. It should be mentioned that the spanwise-averaged separation position also maintains temporarily invariant. Therefore, the well-known breathing of the separation

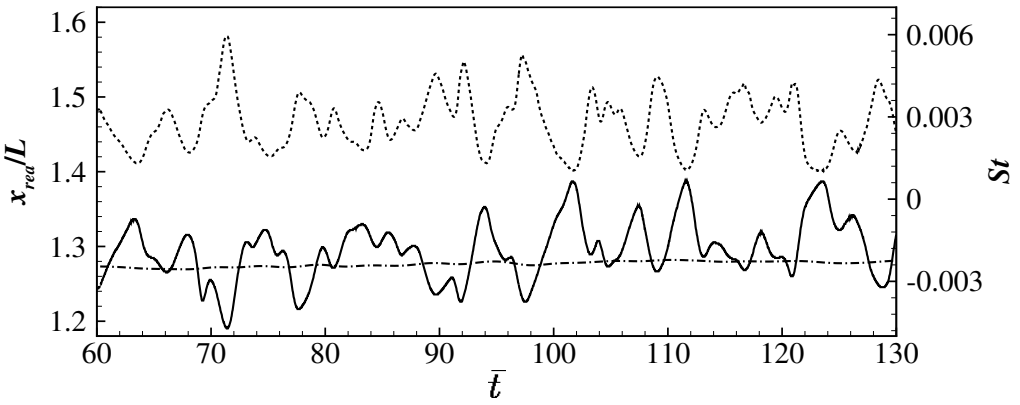


Figure 5.5: Temporal history of reattachment positions in comparison with wall Stanton number. Black solid line corresponds to the reattachment position for the symmetry-plane ($z/L = 0.5$) and dash dot line to the spanwise-averaged reattachment position. Dashed line represents the wall Stanton number signal shown in figure 5.1.

bubble in turbulent SWBLI [5, 6, 32] is absent here. Note however, that the separation bubble size in the present case is much larger than those in the turbulent flow.

By comparing the temporal distribution of the reattachment position at $z/L = 0.5$ and the downstream wall Stanton number, a generally opposite trend is apparent in figure 5.5; when the reattachment position moves downstream, the Stanton number decreases, and vice versa. This is consistent with the flow reattachment topology proposed in Chapter 4 (see figure 4.20), namely, a hot region is always located downstream of a node and a cold region downstream of a saddle point. Therefore, the pulsation of the reattachment position is accompanied by a variation of the downstream surface heat flux. In addition, the spectra of the reattachment position signal are the same as that of the wall Stanton number due to its opposite behaviour.

The above analyses reveal the unsteady behaviour of the streamwise heat flux streaks and their origin to the flow reattachment. In particular, the unsteady heat flux streaks are directly coupled with the pulsation of the reattachment line, oscillating at relatively low frequencies. The unsteadiness propagates in streamwise direction at a speed of $0.7u_\infty$. These results suggest that the unsteadiness might originate from the three-dimensional separation bubble flow as no external disturbances are introduced. In what follows, the separation bubble flow is examined in an attempt to uncover its unsteady structure.

5.1.3 Dynamic mode decomposition of the separation bubble flow

In the following analysis, dynamic mode decomposition (DMD) is employed to characterise the dynamic behaviour of the fully-developed separation bubble flow. Dynamic mode

decomposition, developed by Schmid [96], is a data processing algorithm that extracts coherent spatial structures sharing the same temporal frequency. The extracted dynamic modes are reduced-order representation of the underlying flow field. As a post processing procedure for DMD mode and eigenvalue selection, sparsity-promoting dynamic mode decomposition (SPDMD) has recently been developed by Jovanović et al. [97] to achieve a desirable tradeoff between the quality of approximation and the number of modes that are used to approximate the given flow fields. It facilitates the selection of the dynamically most important modes of the underlying flow field. A brief outline of processing the mode decomposition and selection is given below. For the detailed algorithm of the procedure please refer to Schmid [96] and Jovanović et al. [97].

The first step is collecting a sequence of snapshots which are equi-spaced in time, that is, $X_0^N = \{\psi_0, \psi_1, ..., \psi_N\} \in \mathbb{R}$, where each ψ_i is a column vector including the data (e.g. velocities or vorticities) in one snapshot. The subscript and superscript of X denote the first and last snapshot, respectively. Then, two snapshot matrices are formed:

$$X_0^{N-1} = [\psi_0, \psi_1, \ldots, \psi_{N-1}], \quad X_1^N = [\psi_1, \psi_2, \ldots, \psi_N]. \tag{5.3}$$

A linear time-invariant mapping is assumed to connect two consecutive snapshots:

$$\psi_{i+1} = A\psi_i. \tag{5.4}$$

The objective of DMD is to determine a low-order representation of the matrix A that captures the dynamics inherent in the data sequence. Using the linear relation (5.4), the two snapshot matrices in (5.3) can be connected as $X_1^N = AX_0^{N-1}$. An optimal representation of the mapping matrix A can be obtained using a singular value decomposition (SVD) based approach:

$$F_{dmd} = U^* X_1^N V \Sigma^{-1}. \tag{5.5}$$

Here, U, V, and Σ are the outputs of the SVD of X_0^{N-1}, i.e. $X_0^{N-1} = U\Sigma V^*$ (the superscript $*$ denotes the complex-conjugate transpose). Finally, the individual DMD modes $\Phi_i \in \mathbb{C}$ are obtained by performing eigenvalue decomposition for F_{dmd} and given as follows:

$$\Phi_i = U y_i, \tag{5.6}$$

where $y_i \in \mathbb{C}$ is the eigenvector of F_{dmd}, i.e. $F_{dmd}\, y_i = \mu_i\, y_i$, with $\mu_i \in \mathbb{C}$ being the eigenvalue, which encodes the temporal frequency and growth/decay rate of the individual mode. Therefore, the flow field snapshots can be approximated by a linear combination of the DMD modes:

$$X_0^{N-1} \approx \underbrace{[\Phi_1\ \Phi_2\ \ldots\ \Phi_N]}_{\Phi} \underbrace{\begin{bmatrix} \alpha_1 & & & \\ & \alpha_2 & & \\ & & \ddots & \\ & & & \alpha_N \end{bmatrix}}_{D_\alpha} \underbrace{\begin{bmatrix} 1 & \mu_1 & \ldots & \mu_1^{N-1} \\ 1 & \mu_2 & \ldots & \mu_2^{N-1} \\ \vdots & \vdots & \ddots & \vdots \\ 1 & \mu_N & \ldots & \mu_N^{N-1} \end{bmatrix}}_{V_{and}}, \tag{5.7}$$

where the diagonal matrix D_α can be interpreted as the amplitude of the DMD modes, and V_{and} means a Vandermonde matrix. One possible determination of the amplitude α_i is given by Jovanović et al. [97] through solving the following optimisation problem:

$$\underset{\alpha}{\text{minimise}} \quad \|X_0^{N-1} - \Phi D_\alpha V_{and}\|_F^2, \tag{5.8}$$

where $\|\cdot\|_F$ denotes the Frobenius norm.

As aforementioned, SPDMD is employed to select a subset of DMD modes that have the most substantial influence on the quality of approximation of the snapshot sequence. This algorithm augments the optimisation problem (5.8) with an additional term that penalises the ℓ_1-norm of the vector of amplitudes α_i:

$$\underset{\alpha}{\text{minimise}} \quad \|X_0^{N-1} - \Phi D_\alpha V_{and}\|_F^2 + \gamma \sum_{i=1}^{N-1} |\alpha_i|, \tag{5.9}$$

where γ is a positive regularisation parameter that the larger its value the more zero elements exist in the amplitude vector. A detailed description about the algorithm of solving this convex optimisation problem can be found in the study of Jovanović et al. [97].

Subsequently, the DMD analysis is performed for the separation bubble flow. In particular, the instantaneous distribution of the spanwise velocity component in the x-y plane at $z/L = 0.5$ is decomposed. The database, extracted from $\bar{t} = 100 \sim 130$, includes 1000 snapshots which are equi-spaced by a time interval of $\Delta\bar{t} = 0.03$. This yields a frequency resolution of $0.033 \leq fL/u_\infty \leq 16.7$. The spectrum of the eigenvalues obtained from the standard DMD algorithm is shown in figure 5.6. The resulting modes are symmetric about the real axis due to the real-valued input data. It is apparent that almost all eigenvalues reside on the unit circle. This is expected for a statistically stationary system as the growth/decay rate is nearly zero. The red triangles correspond to the modes selected by SPDMD for a subset of $N_{sp} = 9$. These modes yield the strongest contribution to the dynamics of the flow field. They are located in the low-frequency region, which is in line with the PSD analysis for the downstream wall Stanton number (see figure 5.4). It has to be noted that these five most energetic modes cover 20% of the total energy. To reduce

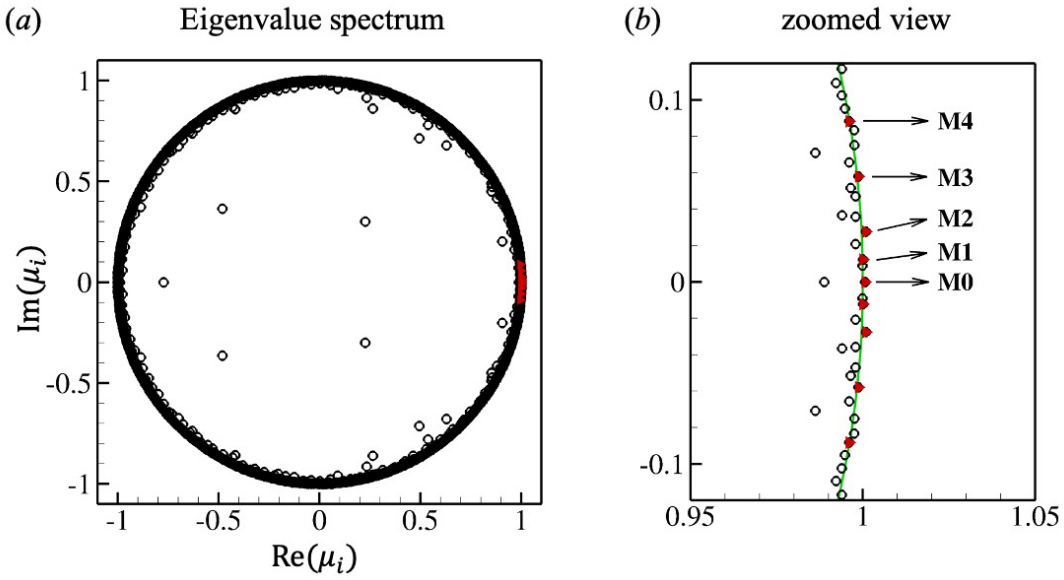


Figure 5.6: (a) Spectrum of the eigenvalues obtained from the standard DMD (circle) and the modes selected by SPDMD (red triangle) for a subset of $N_{sp} = 9$. (b) A zoomed view for the selected modes. Green line is the unit circle.

the energetic loss to 16%, a subset of $N_{sp} = 36$ modes has to be included. These modes nearly cover all the modes in the low-frequency region, and the associated frequencies (fL/u_∞) range from 0 to 1.6. This result indicates that the considered unsteady flow in the separation bubble has a broadband spectra, which is consistent with the PSD analysis for the downstream flow. After post-processing all the 36 modes, it is found that they share similar flow structures. Therefore, the five most energetic modes are selected as a representative subset. They are labelled as M0, M1, M2, M3 and M4, as shown in figure 5.6(b). The associated frequencies are $fL/u_\infty = 0$, 0.07, 0.15, 0.30 and 0.47, respectively (see also figure 5.4(a) for typical frequency range).

Figure 5.7 presents the real part of the modes M0, M1, M3 and M4. The mode M0 has a zero frequency and hence is related to the time-averaged flow. For the other modes, the shown contours represent the fluctuations w'/u_∞ associated with a particular frequency. It is apparent that a certain streamwise periodicity exists in the separation bubble flow. Furthermore, the streamwise length-scale of the periodic structure decreases with increasing frequency. It is noted that these structures are mainly located at the upstream half of the recirculation bubble. The revealed flow structure is consistent with the shape of the unstable oscillatory mode found by Sidharth et al. [44] (figure 5.8(a)). By performing a similar global stability analysis for the 2-D base flow of the present case, Cao et al. [93] identified a similar flow structure (i.e., streamwise periodicity) for the global unstable modes (figure 5.8(b)).

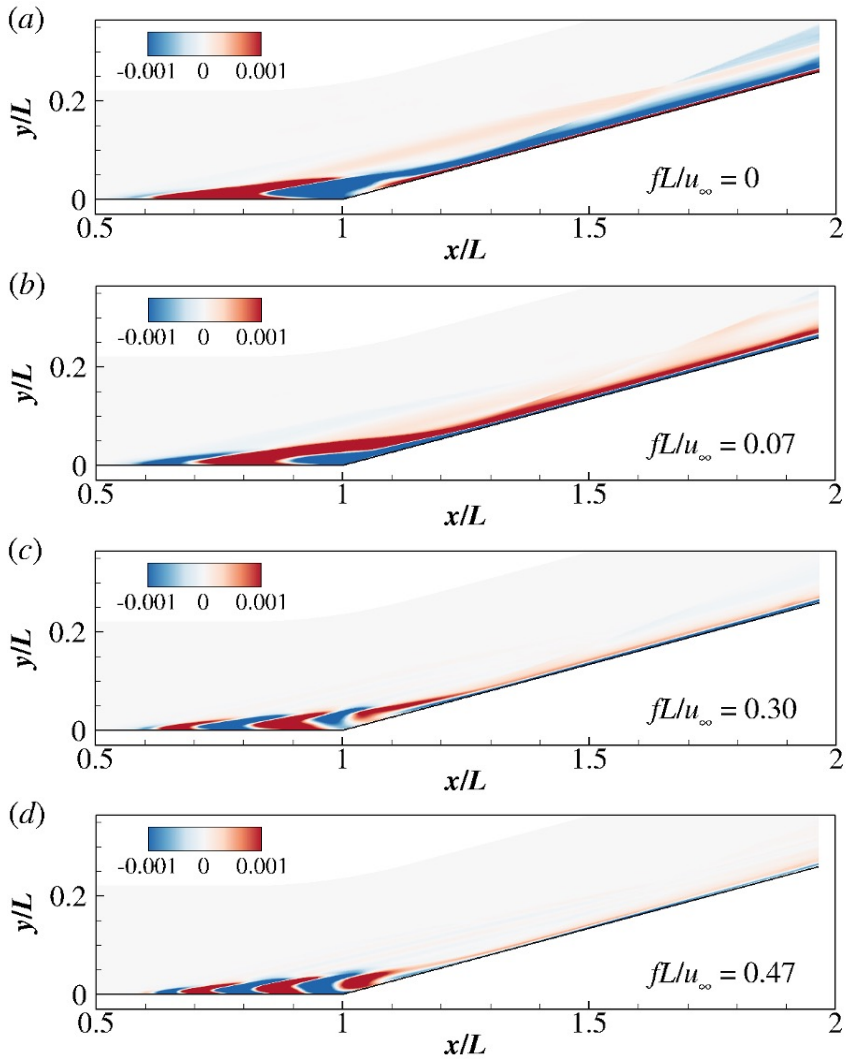


Figure 5.7: DMD modes visualised by contours of spanwise velocity component (w/u_∞). (a-d) correspond to the real part of modes M0, M1, M3 and M4.

As discussed in Chapter 4, coherent structures with spanwise periodicity exist in the time-averaged flow (see figure 4.12), and this stationary structure resembles the shape of the global stationary mode revealed by Sidharth et al. [44]. In combination with the oscillatory modes identified by DMD, it is suggested that the separation bubble flow is characterised by a superposition of several stationary and oscillatory unstable modes. The oscillatory modes are characterised by low-frequency unsteadiness and exhibit streamwise periodicity. Therefore, it is concluded that the intrinsic instability in the separation bubble is responsible for the unsteadiness of the considered compression ramp flow.

Furthermore, figure 5.9 illustrates the position of the periodic structure with respect to the free shear layer. Specifically, two iso-lines of the streamwise velocity component (u/u_∞ = 0.1 and 0.9) are utilised to cover the main part of the shear layer in figure 5.9(a). These two

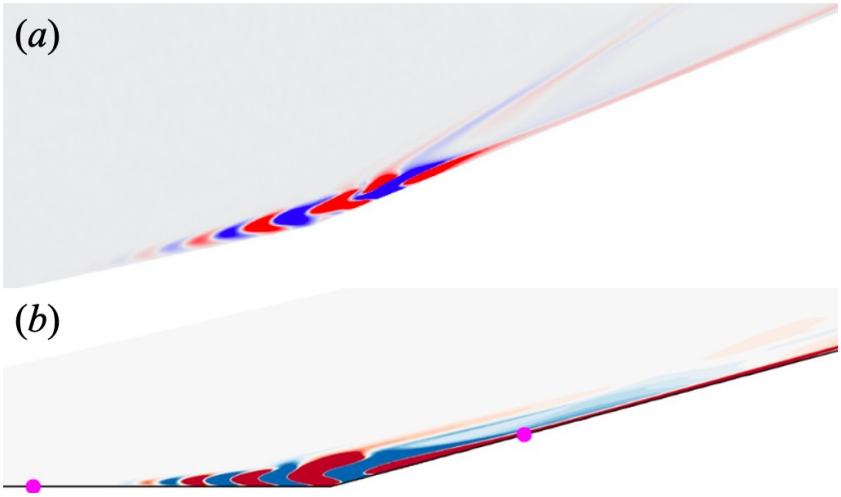


Figure 5.8: Flow structure of the oscillatory unstable modes revealed by the global stability analysis performed by (a) Sidharth et al. [44] and (b) Cao et al. [93].

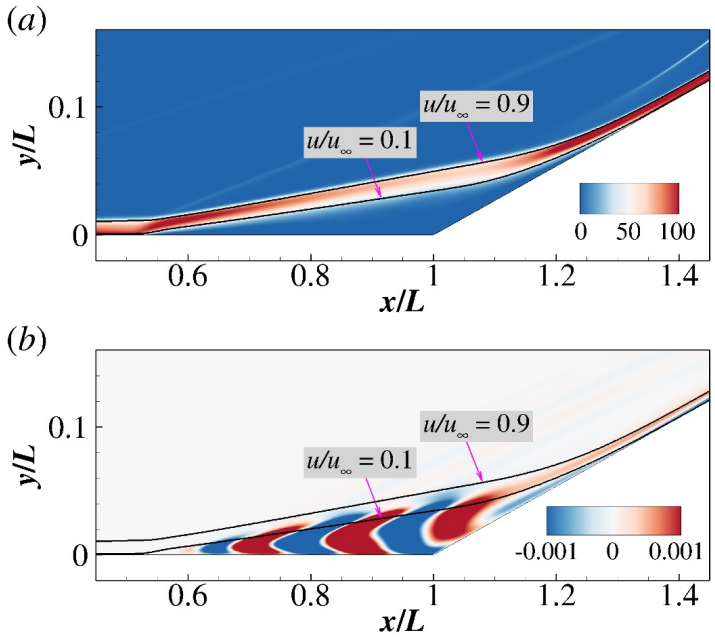


Figure 5.9: (a) Two iso-lines for $u/u_\infty = 0.1$ and $u/u_\infty = 0.9$ embedded in the contour of the dimensionless velocity gradient $\partial\bar{u}/\partial\bar{y}$ which highlights the shear layer. (b) The same iso-lines as in (a) embedded in the contour showing the real part of mode M4.

lines are embedded in the contour for mode M4, namely, in figure 5.7(d), as shown in figure 5.9(b). Mode M4 has been exmeplarily chosen in figure 5.9. The same behaviour holds for the other modes shown in figure 5.7. Note that for a better visualisation, the scales of the horizontal and vertical coordinates are set to be independent. It is clear that the shear layer is able to entrain the periodic structure downstream. This shear layer entrainment is

the key to transport the unsteadiness of the separation bubble flow to the reattached flow, causing the pulsation of the reattachment position and the surface heat flux fluctuation. In fact, figures 5.7 and 5.9 provide obvious evidence for the entrainment of the shear layer, where the spanwise velocity perturbation is persistently stretched downstream of reattachment.

5.2 Unsteady effects for a high Reynolds number case

In the following, the unsteady effects for the high Reynolds number case D1 is analysed, and emphasis is given to the difference with case C4. The analysis is conducted based on the time period of $t = 30 \sim 70$, for which the flow has been shown to be in the quasi-steady state in Chapter 3.

First, the relative standard deviation of the wall Stanton number ($\widehat{St}$) is calculated for all spanwise positions at $x/L = 1.45$, which is close to the peak heating location downstream of reattachment. The result is shown in figure 5.10. In contrast to case C4, the spanwise distribution exhibits no distinct large-scale variation. This relatively uniform distribution is in line with the previous wavelength analysis in Chapter 4. It confirms the absence of large-scale spanwise periodic structure in the time-averaged flow.

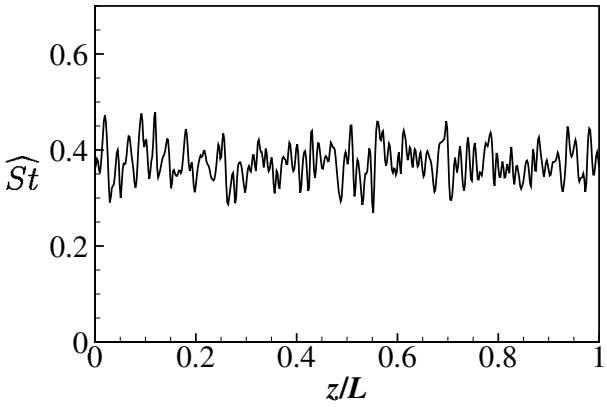


Figure 5.10: Relative standard deviation of the wall Stanton number for all spanwise positions at $x/L = 1.45$ (case D1).

Then, the two-point spatio-temporal correlation (Eq. 5.2) is considered for the wall Stanton number around the reference point: $x/L = 1.45$, $z/L = 0.5$. The resulting correlation maps are presented in figure 5.11. Similar to case C4, the primary propagation direction of the unsteadiness is in streamwise direction. The linear slope of the line shown in figure 5.11(a) gives the travelling speed of the unsteadiness, which is evaluated approximately by $0.6u_\infty$. A further examination of the temporal fluctuation of the reattachment position and wall Stanton number reveals the same opposite trend as case C4. These results

indicate that the flow unsteadiness downstream of reattachment can also be traced back to the separation bubble. On the other hand, the difference in Reynolds number for cases C4 and D1 yields different separation bubble flows, which may hold different unsteady features.

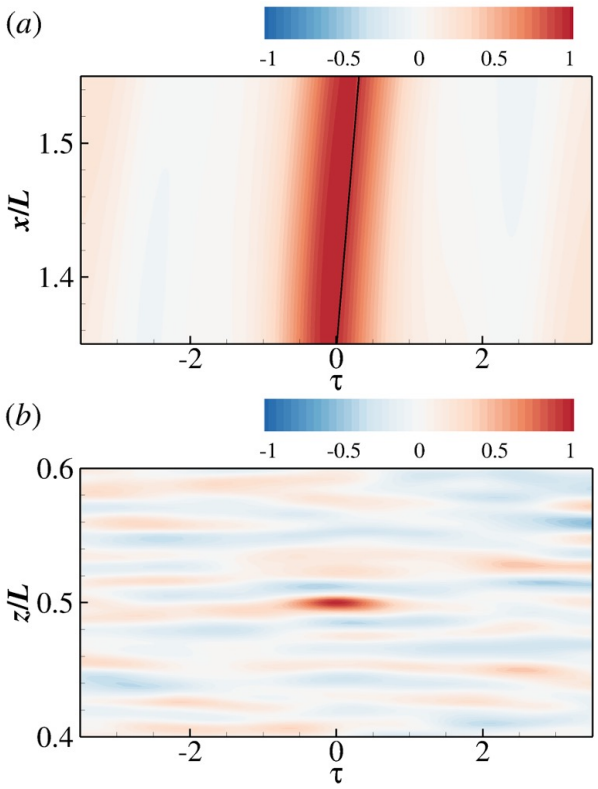


Figure 5.11: Two-point temporal correlation maps for the wall Stanton number in (a) streamwise direction and (b) spanwise direction. Reference point is located at $x/L = 1.45$, $z/L = 0.5$ (case D1).

Figure 5.12(a) provides the power spectra density contour for the wall Stanton number at all spanwise positions ($x/L = 1.45$). The broadband low-frequency feature is consistent with case C4. However, the spectra for case D1 covers a wider frequency range than case C4. Figure 5.12(b) compares the spanwise-averaged PSD as a function of the nondimensional frequency for cases C4 and D1. It is apparent that the spectra for case D1 involves more energetic components for the high frequency region. For example, the frequency range corresponding to a PSD value being larger than 10^{-13} is $fL/u_\infty < 1$ for case C4 and $fL/u_\infty < 2$ for case D1.

Subsequently, the DMD analysis is conducted for the instantaneous spanwise velocity fields in the x-y plane at $z/L = 0.5$. The database is extracted from $\bar{t} = 30 \sim 70$ and includes 800 snapshots which are equi-spaced by a time interval of $\Delta\bar{t} = 0.05$. The resolved frequency range is $0.025 \leq fL/u_\infty \leq 10$. Figure 5.13 presents the resulting spectrum of the eigenvalues. Similar to case C4, nearly all eigenvalues reside on the unit

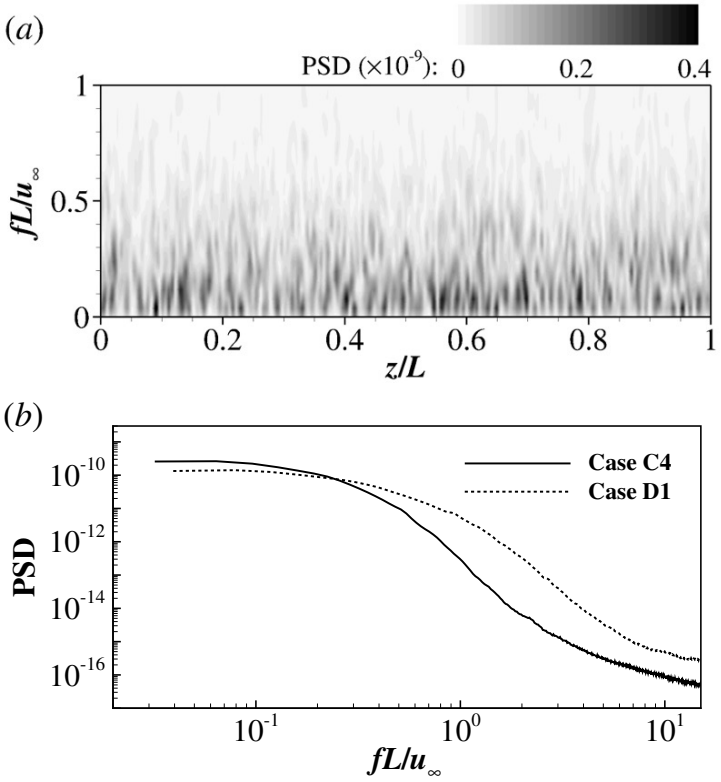


Figure 5.12: (a) Power spectra density map for all spanwise positions at $x/L = 1.45$ for case D1. (b) Spanwise-averaged PSD as a function of the nondimensional frequency for cases C4 ($x/L = 1.5$) and D1 ($x/L = 1.45$).

circle. To facilitate the mode selection, SPDMD algorithm is post-processed to identify the dynamically important modes. It is found that to cover 20% of the total energy, a subset of 12 DMD modes has to be considered, which are shown in figure 5.13(a). These modes are located in the low-frequency region with $0 \leq fL/u_\infty \leq 1$. It means that the separation bubble flow for case D1 covers a wider frequency range than for case C4. This is consistent with the former PSD analysis. By examining all the 12 modes selected by SPDMD, it is also found that they share similar flow structures. Therefore, four modes are exemplarily chosen from the subset, which are labelled as N2, N4, N9 and N10 (see figure 5.13(b)). The associated frequencies are $fL/u_\infty = 0.04$, 0.10, 0.35 and 0.57.

Figure 5.14 presents the real part of the four modes. In general, streamwise periodicity can still be observed for these modes, which is consistent with case C4. However, this periodic flow structure can only be distinguished at the upstream half of the separation bubble. At the downstream half of the separation bubble, the flow structure is relatively irregular. As demonstrated by Sidharth et al. [44], after increasing the deflection angle so as to increase the strength of SWBLI for a double wedge flow, the flow with larger deflection angle is characterised by more global unstable modes. The same effect may also occur for the present cases, because the strength of SWBLI is increased from case C4

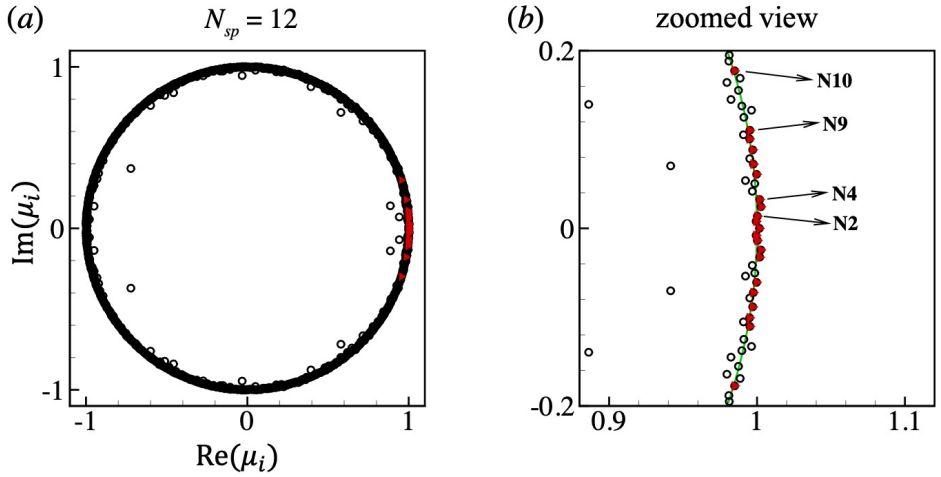


Figure 5.13: (a) Spectrum of the eigenvalues obtained from the standard DMD (circle) and the modes selected by SPDMD (red triangle) for a subset of $N_{sp} = 12$. (b) A zoomed view for the mode selection. Green line is the unit circle.

to case D1. It is therefore conjectured that for case D1, there exist more unstable modes in the separation bubble than for case C4. Nevertheless, the DMD analyses performed for cases C4 and D1 demonstrate the contribution of the instability in the separation bubble flow to the unsteadiness of a laminar separated compression ramp flow.

5.3 Summary

This chapter discusses unsteady effects in two laminar separated hypersonic compression ramp flows. The fully developed flow for cases C4 and D1 are considered. The surface heat flux exhibits a broadband low-frequency unsteadiness, which propagates in streamwise direction. Moreover, the fluctuation of the heat flux and therewith the unsteadiness of the heat flux streaks is coupled with a pulsation of the reattachment position. It is shown that the flow unsteadiness downstream of reattachment originates from the separation bubble. Compared to the low Reynolds number case C4, the surface heat flux fluctuation for the high Reynolds number case D1 involves a wider frequency range. In addition, the flow unsteadiness for case C4 is influenced by the stationary coherent structure in the separation bubble flow.

Dynamic mode decomposition (Standard DMD and SPDMD) is subsequently employed to analyse the oscillatory flow structure in the separation bubble flow. Both for cases C4 and D1, the identified modes having strongest influence on the given snapshot sequence exhibit a streamwise periodicity in the separation bubble. This flow structure is linked to the downstream reattached flow by the shear layer above the separation bubble. The revealed flow structure resembles the shape of the low-frequency oscillatory modes identified by

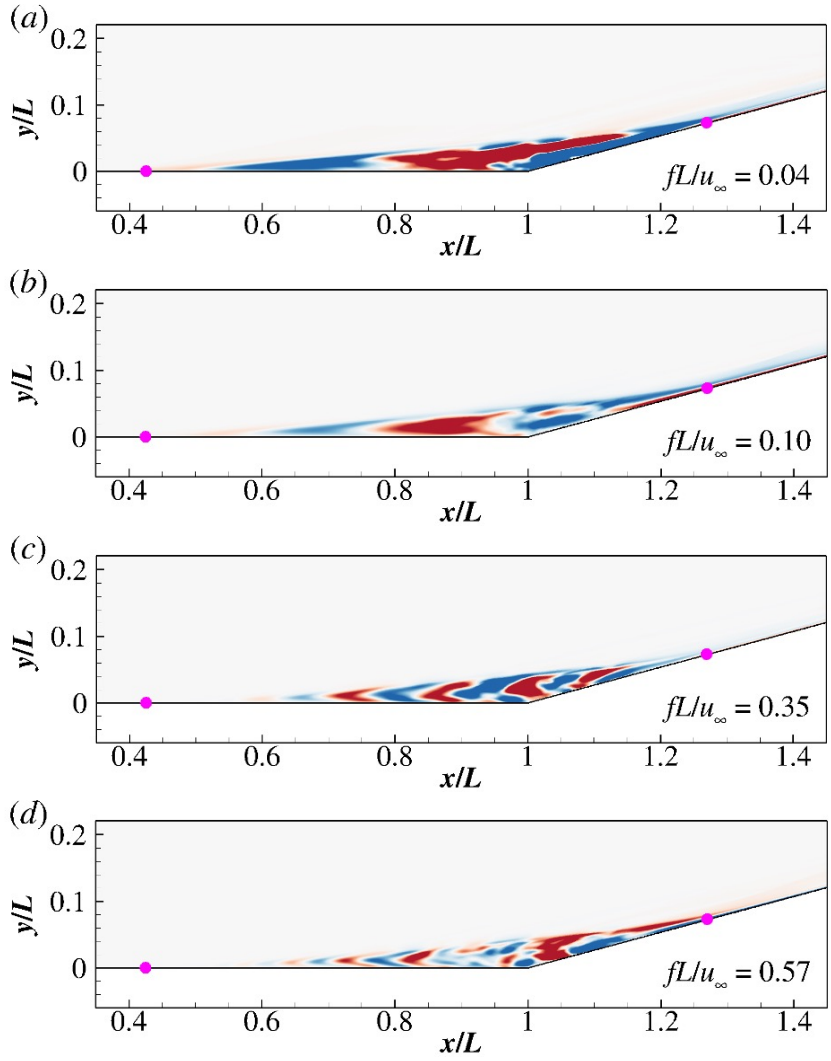


Figure 5.14: DMD modes visualised by contours of the spanwise velocity component. (a-d) correspond to the real part of modes N2, N4, N9 and N10. Circle dots denote the separation and reattachment positions.

the global stability analysis performed by Sidharth et al. [44] and Cao et al. [93] for two separated flows. Therefore, it is concluded that the intrinsic instability in the separation bubble flow is responsible for the unsteadiness of the considered compression ramp flows.

6 Görtler number evaluation for laminar separated compression ramp flow

Essentially, either the streamwise Görtler-like vortices are generated as a result of external disturbances (e.g., free-stream turbulence) or internal disturbances (e.g., instability in the separation bubble), streamline curvature always exists near reattachment. In other words, the centrifugal instability (i.e., Görtler instability) is always at work because it is able to amplify potential disturbances. Hence, an accurate determination of the Görtler number near reattachment could contribute to assess the centrifugal effects. In this chapter, two methods of determining the Görtler number are proposed and verified. A simplified method following from this is applied to the analysis of the Görtler number variation with flow conditions and ramp angle.

6.1 Determination of Görtler number

According to the original definition of the Görtler number, the free-stream unit Reynolds number, the local momentum thickness of the boundary layer and the radius of curvature of the wall have to be known in order to determine the Görtler number for the case of a boundary layer flow over a concave wall. However, for the case of a compression ramp flow, the estimation of the local streamline curvature near reattachment is challenging. In the following, two methods of estimating the streamline curvature near reattachment following determination of the Görtler number are proposed. Exemplarily, cases D1, D3 and D4 with different ramp angles are employed to assist the analysis.

6.1.1 Numerical approach

A numerical method is firstly introduced to determine the Görtler number. As an analogy of the classical concave wall case, the unit Reynolds number upstream of the local flow curvature is approximated by the unit Reynolds number behind the separation shock. This unit Reynolds number is directly determined by the density, velocity and temperature from the DNS data. Like the velocity gradient in the boundary layer on a concave wall, the velocity gradient normal to the concave shear layer is responsible for the centrifugal instability for a compression ramp flow. Here, the concave wall is replaced by the locally curved streamline in the shear layer, as shown in figure 6.1. However, the local streamline curvature varies both in streamwise and in normal direction. Besides, the streamlines

near reattachment do not strictly align to the shear layer characterised by the velocity gradient in normal direction, i.e., the streamlines may not stay within the shear layer for the whole streamwise range. To simplify, one streamline (labeled as 'streamline 1' in figure 6.1) is employed to represent the local curvature of the shear layer. This streamline originates upstream of separation and is located at $y_{x_s} = 0.01\delta_{x_s}$, which ensures that this streamline is within the shear layer. Here, δ_{x_s} is the boundary layer thickness at the separation position x_s.

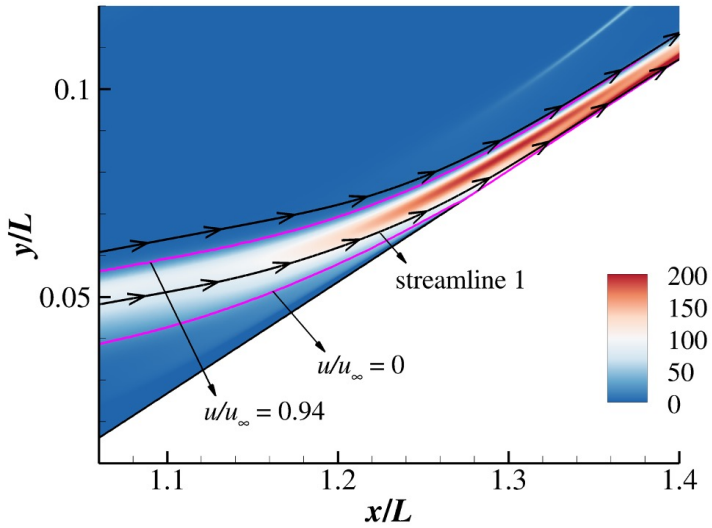


Figure 6.1: Enlarged view of the reattaching shear layer quantified by the velocity gradient $(\partial\bar{u}/\partial\bar{y})$. The shown streamlines originate upstream of separation. The flow field is averaged in time and in spanwise direction for case D1.

The distribution of the dimensionless curvature (L/R) of this streamline for cases D1, D3 and D4 is plotted in figure 6.2(a). As seen, the curvature firstly increases and then drops in streamwise direction. With rising ramp angle, the general curvature increases considerably, and the position of the maximum curvature shifts downstream owing to the rise of the separation bubble length. The momentum thickness of the free shear layer is calculated subsequently from the numerical data. Note that the velocity distribution in the free shear layer is related to the separation bubble and affected by compression waves near reattachment. The integration to determine the local momentum thickness is performed from the line $u/u_\infty = 0$ up to the line $u/u_\infty = 0.94$ (see figure 6.1). The lower border has been chosen because centrifugal instabilities could also be present below the dividing streamline in the reverse flow. Figure 6.2(b) shows the resulting momentum thickness distribution for the three cases. As expected, the momentum thickness drops while approaching the reattachment position.

With the parameters evaluated above, the Görtler number is determined along 'streamline 1' and presented in figure 6.3 for cases D1, D3 and D4. At $x/L = 1.08$, the streamline

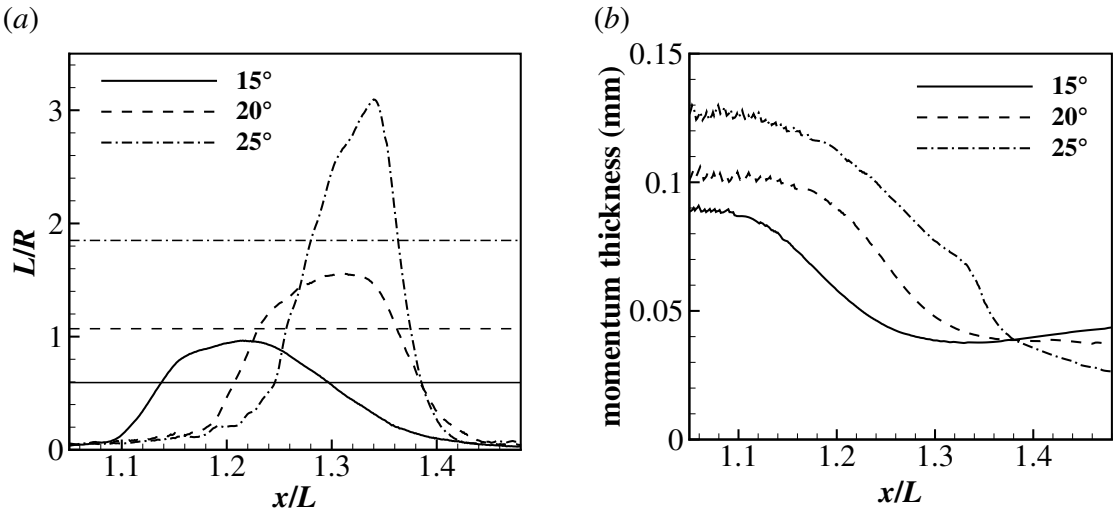


Figure 6.2: (a) Non-dimensional streamline curvature distribution near reattachment for cases D1, D3 and D4 with different ramp angles. Straight lines represent the constant values estimated by Eq. (6.3). (b) Momentum thickness of the free shear layer near reattachment.

curvature is very small ($L/R \approx 0.05$, see figure 6.2(a)), resulting in a Görtler number in the order of 8. Note that the largest momentum thickness is found here (see figure 6.2(b)). In the region where the streamline curvature is dominant the rise of the Görtler number (Eq. (1.3)) is considerable. All the maxima are located upstream of reattachment, being 22, 29 and 44 for cases D1, D3 and D4, respectively. At reattachment, the Görtler number drops quickly due to the decreasing momentum thickness and streamline curvature. Downstream of $x/L = 1.40$, the Görtler number drops to a low level because of the vanishing streamline curvature. As shown in figure 6.3(d), in general the Görtler number increases with rising ramp angle, which indicates that the reattaching shear layer is more centrifugally unstable for higher ramp angles. The estimated threshold for the occurrence of Görtler-like vortices is about 2.7 for the considered flow conditions (see details below). Hence, the Görtler numbers near reattachment are high enough to support the occurrence of Görtler-like vortices.

6.1.2 Simplified approach

The above approach for determining the Görtler number is only possible with the help of numerical simulations. Hence, in order to predict the Görtler number without expensive numerical simulations, a further method on the basis of a simple physical model is proposed. As suggested by Bushnell and Weinstein [98], the separated ramp flow can be idealised by a simple model (figure 6.4(a)). They postulated that peak heating occurs at a distance x_p downstream from reattachment which is proportional to the incoming shear layer thickness. At this position the thickness of the reattaching shear layer becomes

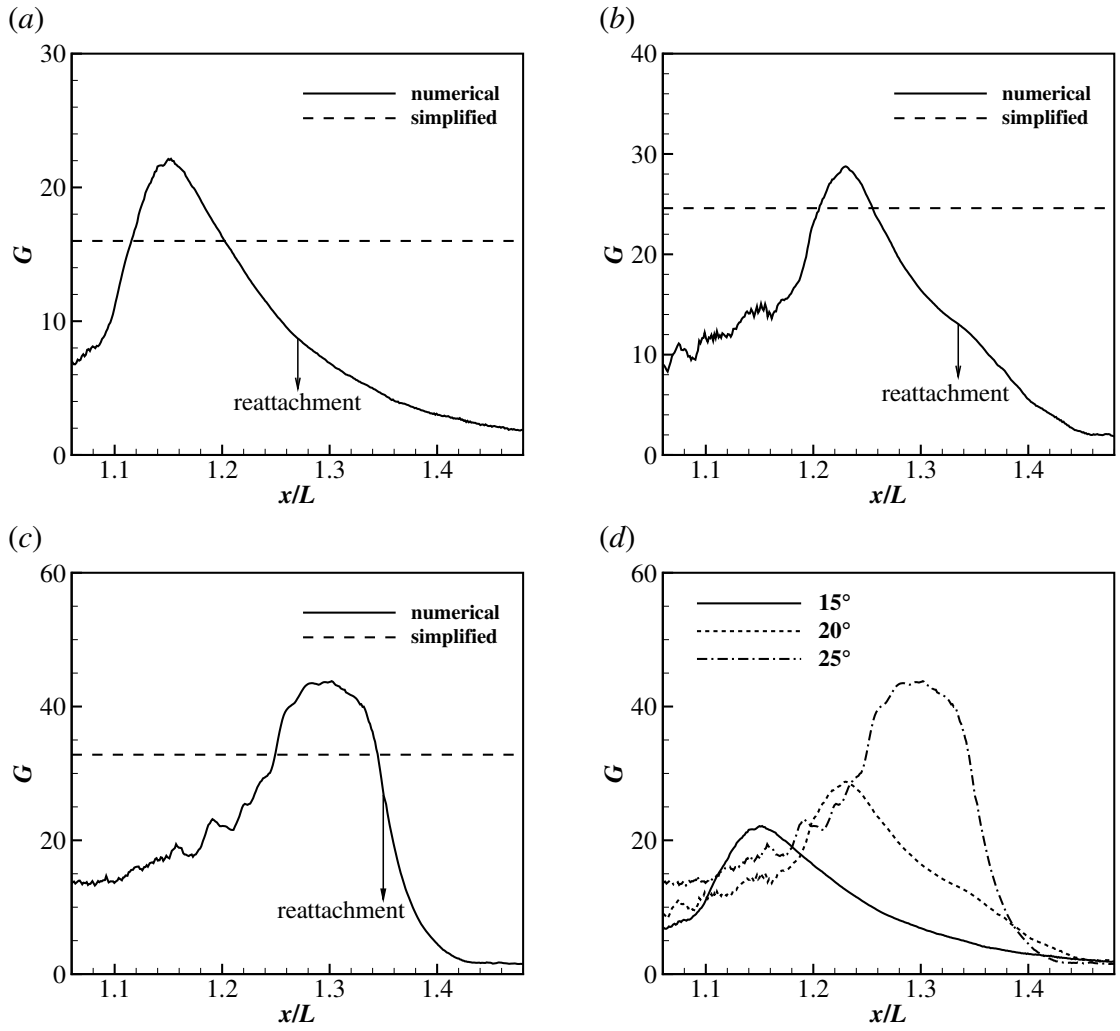


Figure 6.3: Görtler number distribution near reattachment for cases (a) D1, (b) D3, (c) D4 and (d) the three cases. Reattachment points are obtained from the time and spanwise averaged skin friction distributions. The straight lines are determined by Eq. (6.8) which is shown in the following.

minimum and therefore peak heating occurs. In this model, the reattachment point corresponds to the intersection of the dividing streamline (x_2) and the ramp wall. However, by examining the real reattaching process of the shear layer, there are some inconsistences with this model. The curving of the shear layer starts already upstream of the intersection (see figure 6.1). The reattachment point is located downstream of the intersection due to the curved shear layer. Nevertheless, the concept of Bushnell and Weinstein [98] provides a possible way to approximate the radius of curvature. To simplify, the reattaching streamline is approximated by a circular arc (see figure 6.4(b)), which is tangent to the dividing streamline at point 1 and tangent to the wall at point 3. Therefore, the arc angle (2α) is equal to the difference of the ramp angle θ_f and the separation angle

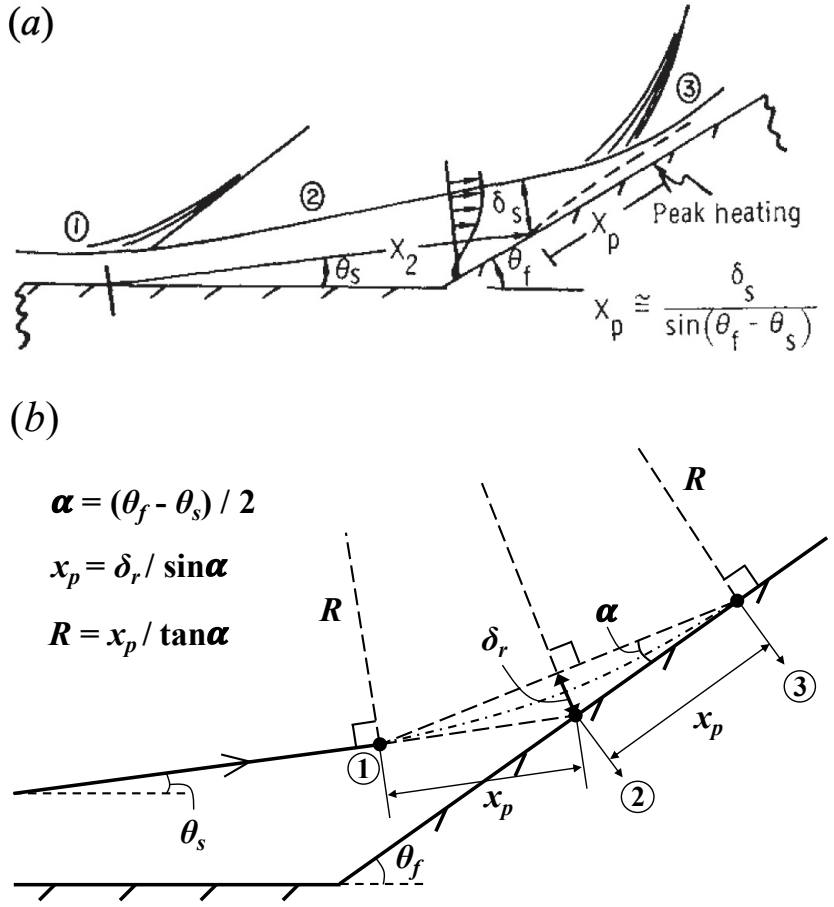


Figure 6.4: Geometrical model for Görtler number estimation, a) original model in reference [98], b) model proposed in the present thesis.

θ_s. By extending the dividing streamline up to the wall at point 2, it is obvious that the distance between point 1 and point 2 (x_p) is equal to that between point 2 and point 3. Similar to figure 6.4(a), this distance can be estimated as

$$x_p = \delta_r / \sin(\frac{\theta_f - \theta_s}{2}), \tag{6.1}$$

where δ_r is assumed as the shear layer thickness at reattachment, as done by Bushnell and Weinstein [98]. In addition, the relation between the radius of curvature R and the distance x_p is

$$R = x_p / \tan(\frac{\theta_f - \theta_s}{2}). \tag{6.2}$$

Therefore, a formula for the estimation of the radius of curvature is obtained based on the shear layer thickness, ramp angle and separation angle:

$$R = \delta_r / [\sin(\frac{\theta_f - \theta_s}{2}) \tan(\frac{\theta_f - \theta_s}{2})]. \tag{6.3}$$

Furthermore, Bushnell and Weinstein [98] assumed that the shear layer thickness is equal to the boundary layer thickness at the separation point plus the thickness of a free fictitious boundary layer which would grow from the separation to the reattachment point with zero initial thickness. However, the latter thickness is overestimated as the spatial growth rate of the shear layer along the separation bubble is smaller than that of the fictitious boundary layer. Actually, the shear layer thickness based on the summed-up boundary layer thickness is nearly 1.5 times than that of the numerical results. Therefore, in the present work, the shear layer thickness is assumed as the thickness of a fictitious flat plate boundary layer growing from the leading edge up to reattachment. To calculate the shear layer thickness, the formula for a flat plate laminar boundary layer [99] is given as follows:

$$\frac{\delta}{x}\sqrt{\frac{Re_{\infty,x}}{C^*}} = K + 2.21\frac{\gamma - 1}{2}M_\infty^2 + 1.93\frac{T_w - T_{aw}}{T_\infty}, \tag{6.4}$$

where $K = 5$ holds for the boundary layer thickness and $K = 1.72$ for the boundary layer displacement thickness. In addition, the momentum thickness is defined [100] as

$$\frac{\delta_2}{x}\sqrt{\frac{Re_{\infty,x}}{C^*}} = 0.664. \tag{6.5}$$

The running length needed for the calculation is the sum of the distance from the leading edge to the separation point x_s and the inclined shear layer length. In fact, these two lengths are not independent and can be determined as follows. Firstly, based on the free interaction theory (Chapman et al. [101]), for a given separation position (x_s), the plateau pressure coefficient is expressed as a function of the flow conditions immediately upstream of the interaction:

$$c_{p,\mathrm{pla}} = k[Re_{\infty,x_s}(M_\infty^2 - 1)]^{-0.25}, \tag{6.6}$$

where k is a constant given as 1.82 according to Chapman et al. [101]. In a first step, a separation position x_s is assumed. The plateau pressure together with the upstream flow conditions determine the separation shock. Hence, the separation angle and the parameters behind the separation shock, e.g. the unit Reynolds number, are obtained. Consequently, the inclined shear layer length as well as the separation bubble length L_b (i.e., the x-wise distance between the separation and reattachment positions) is obtained geometrically by the separation position and the separation angle. Finally, the separation

position is verified by comparing the separation bubble length available in literature. In this thesis, the correlation presented by Burggraf [102] is used:

$$L_p \sim \alpha^{3/2}, \tag{6.7}$$

where L_p is the length of the pressure plateau in the x-direction (for a large separation bubble L_p and L_b is equivalent) and α is a scaled angle. The detailed scaling law is given in the following section 6.1.3. Hence, if the two separation bubble lengths obtained from the assumed separation position and from Eq. (6.11) do not satisfactorily coincide, the separation position is varied and the procedure repeated. After certain iterations, a proper separation position is found.

With the determined separation angle from the plateau pressure, the unit Reynolds number behind the separation shock, the shear layer thickness at reattachment, and the momentum thickness from Eq. (6.5), the Görtler number defined by Eq. (1.3) can be expressed by the following formula:

$$G = K_\infty Re_{\delta_r}[\sin(\frac{\theta_f - \theta_s}{2})\tan(\frac{\theta_f - \theta_s}{2})]^{1/2}, \tag{6.8}$$

where

$$K_\infty = (\delta_2/\delta_r)^{3/2} = [0.664/(5 + 2.21\frac{\gamma - 1}{2}M_\infty^2 + 1.93\frac{T_w - T_{aw}}{T_\infty})]^{3/2} \tag{6.9}$$

denotes a constant dependent on the flow conditions. It is obvious that this method to determine the Görtler number is only dependent on the flow conditions and the geometry of the compression ramp.

Since the numerical method provides the local variation of the streamline curvature and Görtler number, it is interesting to compare them with the value determined by the simplified method described above. The curvatures estimated by Eq. (6.3) and the Görtler numbers determined by Eq. (6.8) are shown in figure 6.2 and figure 6.3, respectively. It is seen that the predicted curvature can quantitatively represent the mean curvature of the reattaching streamline. The Görtler numbers determined by the simplified method are smaller than the maximum values determined by the numerical method and provide an estimation of the dominant magnitude. Therefore, the simplified method predicts a reasonable Görtler number estimation near reattachment.

6.1.3 Verification of the separation bubble length and the simplified method

While several scaling laws regarding the length of the separation bubble are available in literature, a simple relation proposed by Burggraf [102] on the basis of asymptotic theory has been widely used and validated [86, 103]. Burggraf [102] showed that the separation bubble length linearly scales with $\alpha^{3/2}$, where α is a scaled angle given in [104]:

$$\alpha = \frac{\theta Re_{\infty,L}^{1/4}}{C^{1/4}\lambda^{1/2}(M_\infty^2 - 1)^{1/4}}. \tag{6.10}$$

Here, θ is typically a geometric angle such as the ramp angle for a compression ramp, $Re_{\infty,L}$ is the Reynolds number based on free-stream conditions and the flat plate length L, C is the Chapman-Rubesin parameter, λ is a shear constant (0.332 for a Blasius boundary layer), and M_∞ denotes the free-stream Mach number. As shown by Gai and Khraibut [86], the proposed scaling law exhibits a favourable linear relation, independent of the wall temperature and the modes of provoking separation within the framework of shock-wave/boundary-layer interaction.

In order to validate the scaling law and apply it for the calculation of the Görtler number, DNS is employed to study several well-separated hypersonic compression ramp flows. The flow conditions and geometry of the considered cases are listed in Table 6.1, where the scaled angle is given in the last column and T_w/T_0 denotes the wall-to-stagnation temperature ratio. Case 4 includes cases D1, D3 and D4 in the present thesis. Cases 2, 3, and 6 are well-documented concerning the Görtler-like vortices [13, 16, 24]. Cases 5a and 5b are used to study the influence of wall temperature. The same mesh resolution as for case B4 is used for the simulation of these cases.

Table 6.1: Selected cases for the verification of the separation bubble length

Case	M_∞	Re_∞ (m^{-1})	T_∞ (K)	T_w/T_0	L (mm)	θ_f (°)	α
1 [86]	9.1	3.3×10^6	160	0.11	85	16, 18, 24	3.82, 4.30, 5.73
2 [13]	8.0	7.4×10^6	55	0.39	50	15	4.03
3 [16]	7.7	4.2×10^6	125	0.18	100	15, 20, 25	4.31, 5.75, 7.19
4	7.7	8.6×10^6	125	0.18	100	15, 20, 25	5.15, 6.87, 8.59
5a, 5b	7.7	8.6×10^6	61, 125	0.37	100	15	5.10, 5.43
6 [24]	6.85	2.5×10^6	58	0.50	155	15	4.43

Subsequently, the separation bubble length L_b is measured in x-direction for all cases from the separation point to the reattachment point on the basis of the DNS results. Figure 6.5 shows the separation bubble length (normalised by the boundary layer thickness immediately upstream of separation δ_s taken from the DNS data) against $\alpha^{3/2}$. Consistent

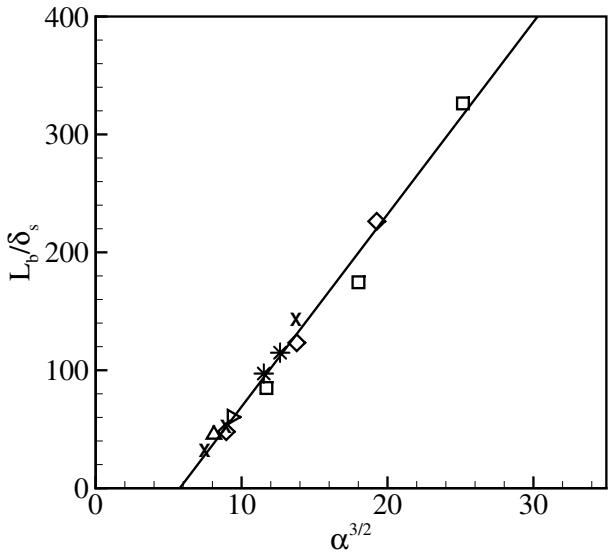


Figure 6.5: Variation of the normalised separation bubble length with the scaled angle α. case 1 (cross); case 2 (triangle); case 3 (diamond); case 4 (square); case 5 (asterisk); case 6 (arrow).

with the results of Korolev et al. [103] and Gai and Khraibut [86], a linear relation is found for the current considered cases. The relationship also appears to be independent of the wall-to-stagnation temperature ratio (see Table 6.1). From figure 6.5, this linear relation can be expressed by

$$L_b/\delta_s = 16.3 \cdot \alpha^{3/2} - 94, \tag{6.11}$$

which is used to determine the separation bubble length and therewith the Görtler number in Eq. (6.8) with the proposed simplified method.

The capability of the simplified method is subsequently assessed by employing a number of experimental [13, 16] and numerical [24, 37] data. Table 6.2 lists the flow conditions of the selected ramp flow cases and the corresponding wavelengths of the surface heat flux streaks. All the Görtler numbers determined by Eq. (6.8) are presented in a Görtler stability diagram (figure 6.6). The figure also shows the neutral curve given by El Hady and Verma [105] for Mach 5 and the dimensionless wavelength parameter

$$\Lambda = Re_\lambda(\lambda/R)^{1/2}, \tag{6.12}$$

which allows to express the Görtler number as

$$G = (2\pi)^{-3/2}\Lambda\beta^{3/2}, \tag{6.13}$$

Table 6.2: Selected cases for the verification of the simplified approach

Case	M_∞	$Re_{\infty,L}$	θ_f (°)	T_∞ (K)	T_w/T_0	λ (mm)
Roghelia [16]	7.7	4.2×10^5	15, 20, 25	125.0	0.18	5.0
Chuvakhov [13]	8.0	3.7×10^5	15, 25	55.1	0.39	3.3
Navarro-Martinez [24]	6.85	3.8×10^5	15	57.8	0.50	4.8
Ohmichi [37]	7.0	1.12×10^5	30	46.3	0.60	1.0

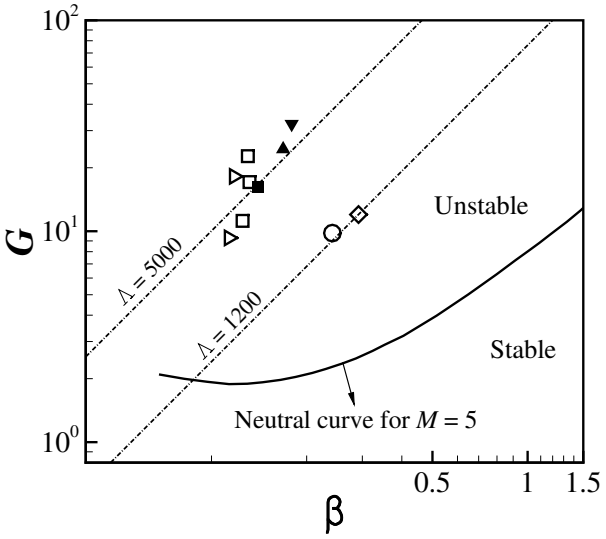


Figure 6.6: Görtler stability diagram for different cases. Present thesis: ■ - E1, ▲ - E2, ▼ - E3; □ - Roghelia [16]; ▷ - Chuvakhov [13]; ◯ - Navarro-Martinez [24]; ◊ - Ohmichi [37]; Neutral curve - El-Hady and Verma [105].

where β denotes the non-dimensional wavenumber ($\beta = 2\pi\delta_2/\lambda$) and λ the spanwise wavelength of the Görtler-like vortices. Hence, in a logarithmic scale, lines of constant Λ representing the wavelength of the Görtler-like vortices for a given flowfield have a slope of 3/2. As seen in figure 6.6, the cases of Navarro-Martinez [24] and Ohmichi [37] correspond approximately to $\Lambda = 1200$, and the other cases to about $\Lambda = 5000$. This is reasonable because these two groups correspond to two different sets of flowfield which involve different Mach numbers, i.e. $M \approx 8$ and 7. It has to be mentioned that for experimental as well as numerical data it is hard to exactly determine the wavelength of the spanwise heat flux distribution because of a nonuniform streak pattern and its unsteadiness. Therefore, the non-dimensional wavenumber in figure 6.6 also has some uncertainty. These and other reasons only allow qualitative conclusions from the data shown in figure 6.6. On the other hand, the shown neutral curve which has been determined for compressible boundary layer flow and a constant radius of curvature varies with Mach number. According to El Hady

and Verma [105] and Hall and Fu [106], the critical Görtler number, which is given by the minimum of the neutral curve, increases with Mach number and scales with $(log(M^2))^{3/2}$. Therefore, based on the result for $M = 5$, the critical Görtler number can be estimated as 2.5 and 2.8 for Mach number 7 and 8, respectively. Hence, all the data points in figure 6.6 are expected to be in the unstable region where centrifugal disturbances are amplified and Görtler-like vortices should occur. Finally, it should be noted that unlike the case of a concave wall, the dominant centrifugal excitation in the compression ramp flow only takes place between $x/L \approx 1.0$ and 1.4 (see figure 6.3). This excitation distance is much shorter than the total streamwise length of the vortices along the ramp. Also due to this, the classical stability analysis is not fully applicable to the compression ramp flow as the Görtler number rapidly decreases downstream of reattachment and the separation bubble flow may additionally affect the centrifugal instability. Based on the above discussion, it is concluded that the simplified method predicts a relatively realistic Görtler number near reattachment for compression ramp flows, which contributes to characterising the Görtler instability.

6.2 Görtler number variation in compression ramp flow

The simplified model enables the evaluation of the Görtler number variation related to the freestream parameters and ramp angles, which provides a view of the influence of the flow separation on the Görtler instability. Figure 6.7 shows the variation of Görtler number and streamline curvature at reattachment for different parameters. The reference case is E1 (i.e. $M_\infty = 7.7$, $Re_{\infty,L} = 8.6 \times 10^5$, $T_w/T_0 = 0.18$, and $\theta_f = 15°$). As shown in figure 6.7(a), the Görtler number increases linearly with increasing ramp angle, indicating a stronger Görtler instability for higher ramp angles. Referring to Eq. (6.8), it can be estimated that the Görtler number is approximately proportional to the ramp angle. In reality, the main effect of the ramp angle on the Görtler number is to change the streamline curvature by deflecting the flow at reattachment. Several experimental and numerical studies have been devoted to this influence of the ramp angle on the Görtler-like vortices [14, 16, 38].

Figure 6.7(b) shows that the Görtler number increases with unit free-stream Reynolds number. Note that the relation is not linear because a rise in Reynolds number also reduces the momentum thickness (for a laminar boundary layer, $\delta_2 \sim 1/\sqrt{Re}$). It should also be noted that the separation bubble length rises with Reynolds number. In this case the reattachment remains nearly at the same position, which leads to an increase in streamline curvature at reattachment, as shown in figure 6.7(b). Therefore, the overall effect of an increasing unit Reynolds number is to enhance the Görtler instability, which was confirmed by Klioutchnikov et al. [71].

Figure 6.7(c) shows an opposite trend for the free-stream Mach number, i.e. the Görtler number decreases with increasing Mach number. The reasons are twofold. First, it is

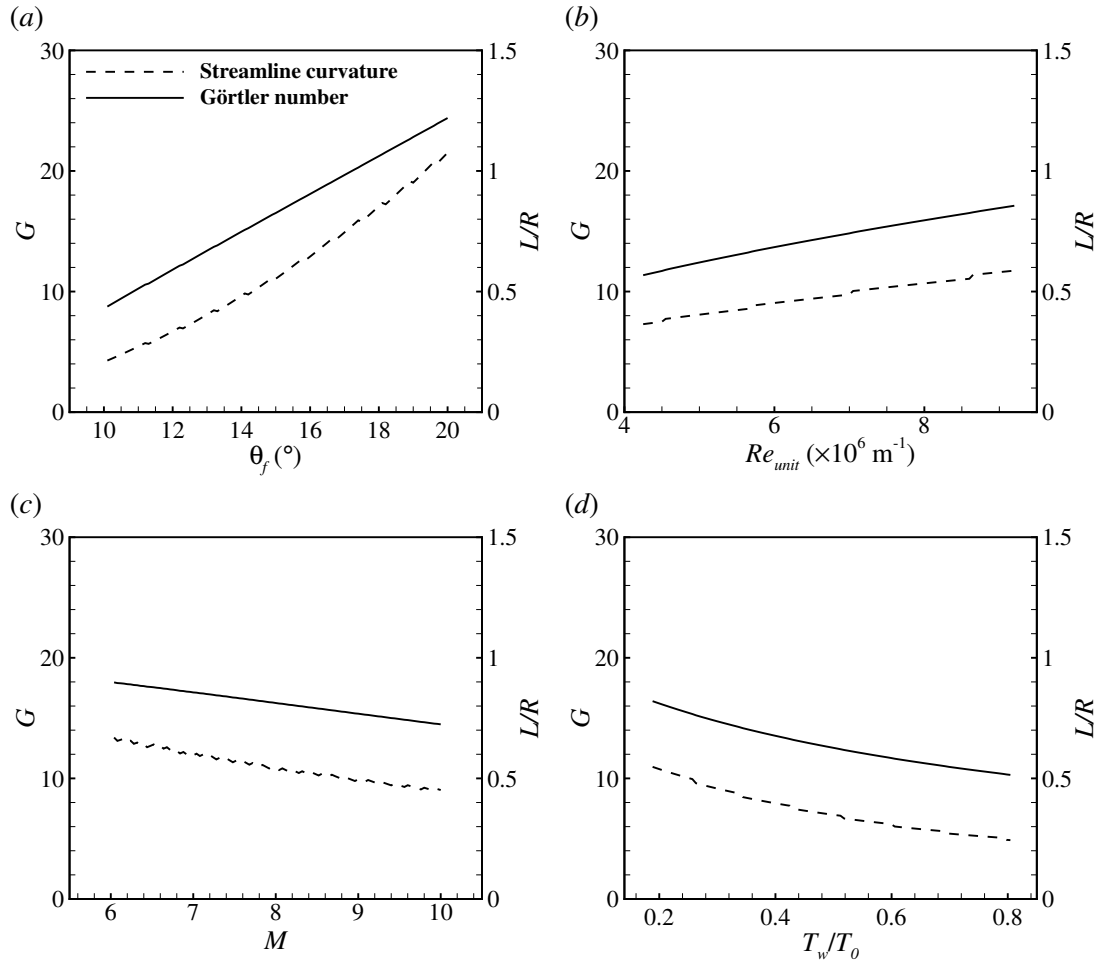


Figure 6.7: Variation of Görtler number and streamline curvature with (a) ramp angle, (b) unit Reynolds number, (c) Mach number, and (d) wall-to-stagnation temperature ratio.

known that the boundary layer momentum thickness decreases, although very slowly, with increasing Mach number. Second, as aforementioned, an increasing Mach number leads to a smaller separation bubble. The streamline curvature slightly drops, as seen in the figure 6.7(c). It should be mentioned that the considered Mach number herein is in the hypersonic regime, within which the variation of separation bubble length might be different to supersonic flow, depending on the flow conditions and ramp angle [2]. Nevertheless, for the considered cases, the influence of an increasing Mach number is to reduce the separation extent and the Görtler number.

The influence of wall temperature is also presented in figure 6.7(d). In particular, increasing the wall-to-stagnation temperature ratio results in a decrease in Görtler number. This result should not be confused with the trend of separation bubble length although wall heating usually leads to a growth of the separation bubble [10, 11]. As demonstrated by Bleilebens and Olivier [11], the change of the separation bubble length is associated with

the movement of both the separation and reattachment positions. For higher wall-to-stagnation temperature ratios, the reattachment position moves downstream to a certain degree. Consequently, the streamline curvature is reduced, which is shown in figure 6.7(d) and further discussed below. On the other hand, increasing wall temperature leads to a slight decrease in momentum thickness [16], although the boundary layer thickness rises. Therefore, the above facts account for the variation of Görtler number with wall temperature. Nevertheless, the effects of the Mach number and wall temperature on the Görtler-like vortices require more experimental and numerical evidence.

6.2.1 Further remarks on wall temperature influence

As aforementioned, the wall temperature affects both the separation bubble length and the Görtler number. Because the wall temperature itself does not account for the boundary layer behaviour, the wall-to-stagnation temperature ratio is considered herein (see Table 6.1). It is clear that there are two ways to increase the temperature ratio, i.e. increasing wall temperature or decreasing stagnation temperature. To identify the influence of these two ways, figure 6.8 shows the numerical schlieren for the cases 4 (15° ramp angle), 5a and 5b listed in Table 6.1. For case 4, the wall and stagnation temperature are 293 K and 1607 K, respectively. For case 5a, the wall and stagnation temperature are 293 K and 785 K, respectively, compared to 600 K and 1607 K for case 5b. It is observed that the extent of the separation bubble is nearly the same for the high temperature ratio cases 5a and 5b, irrespective of the way of achieving this ratio. In addition, the separation angle is slightly increased in comparison to case 4 (in figures. 6.8(a-c), $\theta_s \approx 4°$, 5° and 5°, respectively). Therefore, the increase in separation angle and shear layer thickness due to the higher wall-to-stagnation temperature ratio, according to Eq. (6.3), leads to a larger radius of curvature and consequently a drop in Görtler number.

6.3 Summary

Two methods of determining the Görtler number near reattachment are proposed. The first one gives the variation of the Görtler number on the basis of the DNS results. Additionally, based on a simplified model, a formula depending only on the flow conditions and the geometry of the compression ramp is deduced to predict the Görtler number. It is shown that the latter method can quantitatively predict the Görtler number near reattachment, and the predictions are in qualitative agreement with a theoretical stability analysis. Furthermore, it is found that the Görtler number increases with increasing ramp angle and unit Reynolds number, and decreases with increasing Mach number and wall temperature ratio. These findings contribute to the characterisation of the centrifugal instability near reattachment for a compression ramp flow.

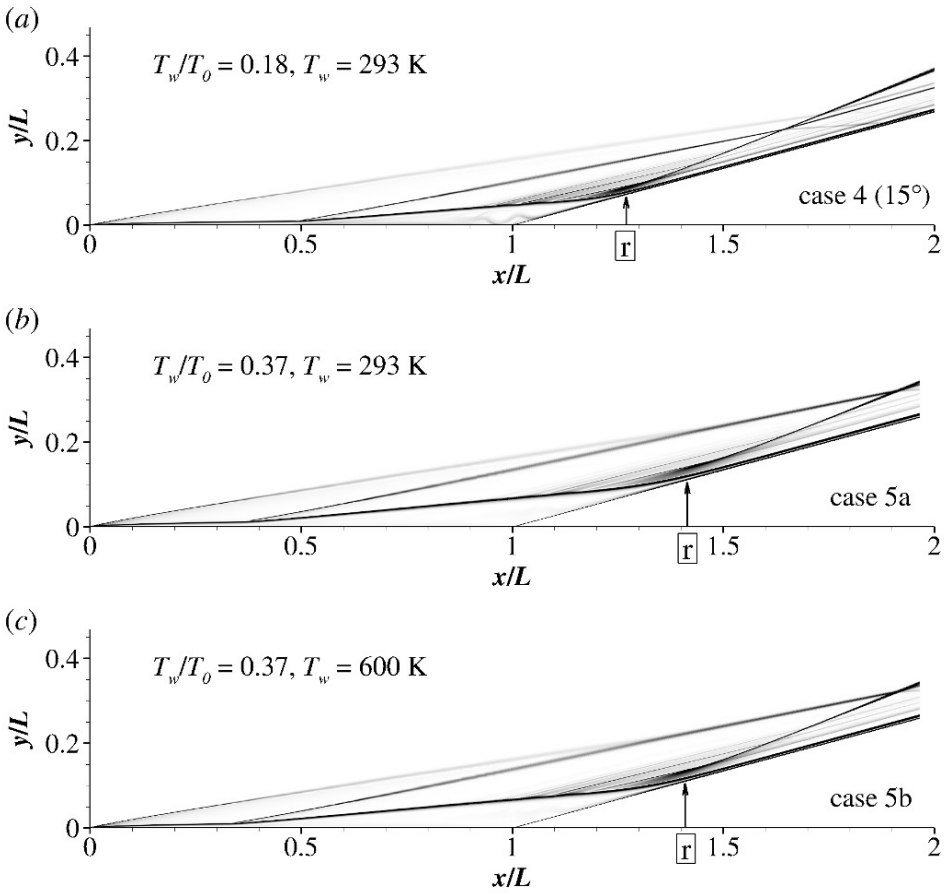


Figure 6.8: Numerical schlieren for three cases listed in Table 6.1 with different wall and stagnation temperatures. The reattachment point is highlighted.

7 Conclusion

The aim of this thesis was to study the shock wave/boundary layer interaction over a compression ramp and obtain an improved understanding of the physics of hypersonic compression ramp flow, which contributes to predicting and controlling the internal and external flow around a high-speed vehicle. In the present thesis, compression ramp flows with a free-stream Mach number of 7.7 were numerically studied to complement the experimental campaign carried out in the hypersonic shock tunnel TH2 at the Shock Wave Laboratory of RWTH Aachen University.

This work focused on laminar SWBLI with a moderate separation. Two flow conditions with different free-stream Reynolds numbers [78] were considered for a two-dimensional compression ramp configuration with different deflection angles. Direct numerical simulations were performed to investigate the behaviour of streamwise vortices and surface heat flux streaks occurring in the compression ramp flow. A comprehensive mesh study was first conducted to demonstrate the grid convergence for the flow phenomena of interest. Subsequently, the DNS results were validated by comparing to experimental data as well as theoretical predictions. Excellent agreement was achieved concerning the viscous interaction at the leading edge, the laminar boundary layer upstream of separation, the wall pressure and heat flux data, the wavelength of the surface heat flux streaks, etc. Special emphasis was put on the finite-span effects encountered in experiments. It was shown that for both flow conditions, the experimentally considered aspect ratio of the compression ramp model was sufficient to maintain flow properties near the model centre corresponding to an infinite span flow when the ramp angle is 15°. However, for the compression ramp with a deflection angle of 20°, finite-span effects led to a considerable reduction in the separation bubble size.

Consistent with the experimental observations, the DNS results presented in this thesis demonstrated the presence of streamwise vortices and heat flux streaks in the compression ramp flow. The basic characteristics of the vortices and streaks were analysed and compared with the experimental data [16, 17, 78]. In terms of the time-averaged flows, the spanwise variation of the wall Stanton number with respect to the spanwise-averaged value varies from 7% to 12% in the vicinity of the peak heating location for the considered cases, which agrees with experimental measurements. In addition, the heat transfer enhancement with respect to the 2-D solution reaches up to 87% downstream of reattachment, and the increment goes up with increasing free-stream Reynolds number and ramp angle. In general, the wavelength of streamwise vortices and streaks for the high Reynolds number case is smaller than that for the low Reynolds number case. However, for the considered

flow conditions, the wavelength of the streamwise streaks is insensitive to the selected ramp angles, which is consistent with the experimental results.

The agreement between experimental and numerical results implies similar physical mechanisms underlying the formation and the development of streamwise vortices and streaks in experiments and simulations. It should be noted that no external artificial disturbances were introduced in the numerical simulations. However, external disturbances were inevitably encountered in the experiments. Therefore, it seems that the occurrence of three-dimensionality in the considered flows is triggered by the inherent instability of the fluid dynamic system. In fact, hints implying the influence of the separation bubble flow on the downstream heat flux streaks were observed in the DNS data. This is in line with the results of Sidharth et al. [44] and Cao et al. [93], who showed that the intrinsic instability in the separation bubble flow contributes to the formation of streamwise streaks.

It was shown that the instability in the separation bubble flow also affects the flow unsteadiness. In the fully developed flow, the surface heat flux downstream of reattachment exhibits a broadband low-frequency unsteadiness, which propagates in streamwise direction. Moreover, the fluctuation of the heat flux and therewith the unsteadiness of the heat flux streaks is coupled with a pulsation of the reattachment position. Compared to the low Reynolds number case, the surface heat flux fluctuation for the high Reynolds number case involves a wider frequency range. In addition, the flow unsteadiness for the low Reynolds number case is influenced by the stationary coherent structure in the separation bubble flow. The downstream flow unsteadiness was shown to originate from the separation bubble.

By conducting a dynamic mode decomposition analysis, several oscillatory modes, characterised by streamwise low-frequency periodicity, were revealed in the separation bubble flow. This flow structure is linked to the downstream reattached flow by the shear layer above the separation bubble. The revealed flow structure resembles the shape of the low-frequency oscillatory modes identified by the global stability analysis performed by Sidharth et al. [44] and Cao et al. [93] for two separated flows. Therefore, it is concluded that the intrinsic instability in the separation bubble flow is responsible for the unsteadiness of the considered compression ramp flows.

Besides the instability in the separation bubble flow, centrifugal instability resulting from the local streamline curvature near reattachment was examined by determining the Görtler number by different methods. The first one gives the variation of the Görtler number on the basis of the DNS data. Additionally, based on a simplified model, a formula depending only on the flow conditions and the geometry of compression ramp was deduced to predict the Görtler number. It was shown that the latter method can quantitatively predict the Görtler number near reattachment, and the predictions are in qualitative agreement with a theoretical stability analysis. Furthermore, it was found that the Görtler number increases with increasing ramp angle and unit Reynolds number, and it decreases with increasing

Mach number and wall-to-stagnation temperature ratio. These findings contribute to characterising the centrifugal instability near reattachment for a compression ramp flow.

It is finally noted that the formation and evolution of streamwise vortices in a compression ramp flow is governed by several mechanisms and affected by several factors such as the form and magnitude of external disturbances, the instabilities in the separation bubble, the baroclinic effects and centrifugal effects, etc. The individual role of these mechanisms in the occurrence and wavelength selection of the streamwise vortices should be further studied. The following studies are therefore worthy of consideration.

- The contribution of external disturbances to the formation and evolution of the streamwise vortices, both in globally stable and unstable flows.
- The individual role of the separation bubble instability and centrifugal instability in the evolution and wavelength selection of the streamwise vortices and streaks. The present thesis addressed the importance of the separation bubble instability and centrifugal instability. But their individual role is still unclear.
- From a practical point of view, the main goals of studying the physics of hypersonic compression ramp flow is to understand the flow unsteadiness and predict the subsequent boundary layer transition process. Since this thesis focuses on the early stage of laminar-turbulent transition, one may take the effort to uncover the mechanisms responsible for the transition downstream of reattachment.

Bibliography

[1] D. S. Dolling. 'Fifty years of shock-wave/boundary-layer interaction research: what next?' *AIAA Journal* 39.8 (2001), pp. 1517–1531. DOI: 10.2514/2.1476.

[2] H. Babinsky and J. K. Harvey. *Shock wave-boundary-layer interactions*. Vol. 32. Cambridge University Press, 2011.

[3] D. V. Gaitonde. 'Progress in shock wave/boundary layer interactions'. *Progress in Aerospace Sciences* 72 (2015), pp. 80–99. DOI: 10.1016/j.paerosci.2014.09.002.

[4] J. J. Ginoux. *On some properties of reattaching laminar and transitional high speed flows.* Tech. rep. von Karman Institute for Fluid Dynamics, Belgium, 1969.

[5] N. T. Clemens and V. Narayanaswamy. 'Low-frequency unsteadiness of shock wave/turbulent boundary layer interactions'. *Annual Review of Fluid Mechanics* 46 (2014), pp. 469–492. DOI: 10.1146/annurev-fluid-010313-141346.

[6] S. Priebe and M. P. Martín. 'Low-frequency unsteadiness in shock wave–turbulent boundary layer interaction'. *Journal of Fluid Mechanics* 699 (2012), pp. 1–49. DOI: 10.1017/jfm.2011.560.

[7] J. Délery, J. G. Marvin and E. Reshotko. *Shock-wave boundary layer interactions.* Tech. rep. ADVISORY GROUP FOR AEROSPACE RESEARCH and DEVELOPMENT NEUILLY-SUR-SEINE (FRANCE), 1986.

[8] D. A. Needham. 'Laminar separation in hypersonic flow'. PhD thesis. Imperial College London, 1965.

[9] B. Edney. *Anomalous Heat Transfer and Pressure Distributions on Blunt Bodies at Hypersonic Speeds in the Presence of an Impinging Shock.* Tech. rep. Flygtekniska Forsoksanstalten, Stockholm (Sweden), 1968.

[10] J. E. Lewis, T. Kubota and L. Lees. 'Experimental investigation of supersonic laminar, two-dimensional boundary-layer separation in a compression corner with and without cooling.' *AIAA Journal* 6.1 (1968), pp. 7–14. DOI: 10.2514/3.4434.

[11] M. Bleilebens and H. Olivier. 'On the influence of elevated surface temperatures on hypersonic shock wave/boundary layer interaction at a heated ramp model'. *Shock Waves* 15.5 (2006), pp. 301–312. DOI: 10.1007/s00193-006-0025-2.

[12] J. J. Ginoux. 'Streamwise vortices in reattaching high-speed flows-A suggested approach'. *AIAA Journal* 9.4 (1971), pp. 759–760.

[13] P. Chuvakhov, V. Y. Borovoy, I. Egorov, V. Radchenko, H. Olivier and A. Roghelia. 'Effect of small bluntness on formation of Görtler vortices in a supersonic compression corner flow'. *Journal of Applied Mechanics and Technical Physics* 58.6 (2017), pp. 975–989. DOI: 10.1134/S0021894417060037.

[14] L. de Luca, G. Cardone, D. A. de la Chevalerie and A. Fonteneau. 'Viscous interaction phenomena in hypersonic wedge flow'. *AIAA Journal* 33.12 (1995), pp. 2293–2298. DOI: 10.2514/3.12982.

[15] G. Simeonides and W. Haase. 'Experimental and computational investigations of hypersonic flow about compression ramps'. *Journal of Fluid Mechanics* 283 (1995), pp. 17–42. DOI: 10.1017/S0022112095002229.

[16] A. Roghelia, H. Olivier, I. Egorov and P. Chuvakhov. 'Experimental investigation of Görtler vortices in hypersonic ramp flows'. *Experiments in Fluids* 58.10 (2017), p. 139. DOI: 10.1007/s00348-017-2422-y.

[17] A. Roghelia, P. V. Chuvakhov, H. Olivier and I. Egorov. 'Experimental investigation of Görtler vortices in hypersonic ramp flows behind sharp and blunt leading edges'. In: *47th AIAA Fluid Dynamics Conference*. 2017, p. 3463. DOI: 10.2514/6.2017-3463.

[18] R. Benay, B. Chanetz, B. Mangin, L. Vandomme and J. Perraud. 'Shock wave/transitional boundary-layer interactions in hypersonic flow'. *AIAA Journal* 44.6 (2006), pp. 1243–1254.

[19] L. Brown, R. Boyce, N. Mudford and S. O'Byrne. 'Intrinsic three-dimensionality of laminar hypersonic shock wave/boundary layer interactions'. In: *16th AIAA/DLR/DGLR International Space Planes and Hypersonic Systems and Technologies Conference*. 2009, p. 7205.

[20] L. Yang, H. Zare-Behtash, E. Erdem and K. Kontis. 'Investigation of the double ramp in hypersonic flow using luminescent measurement systems'. *Experimental thermal and fluid science* 40 (2012), pp. 50–56. DOI: 10.1016/j.expthermflusci.2012.01.032.

[21] S. Willems, A. Gülhan and J. Steelant. 'Experiments on the effect of laminar–turbulent transition on the SWBLI in H2K at Mach 6'. *Experiments in Fluids* 56.3 (2015), p. 49. DOI: 10.1007/s00348-015-1904-z.

[22] J. Floryan. 'On the Görtler instability of boundary layers'. *Progress in Aerospace Sciences* 28.3 (1991), pp. 235–271. DOI: 10.1016/0376-0421(91)90006-P.

[23] W. S. Saric. 'Görtler vortices'. *Annual Review of Fluid Mechanics* 26.1 (1994), pp. 379–409.

[24] S. Navarro-Martinez and O. Tutty. 'Numerical simulation of Görtler vortices in hypersonic compression ramps'. *Computers & Fluids* 34.2 (2005), pp. 225–247. DOI: 10.1016/j.compfluid.2004.05.002.

[25] Y. Ishiguro, H. Nagai, K. Asai and K. Nakakita. 'Visualization of hypersonic compression corner flows using temperature-and pressure-sensitive paints'. In: *45th AIAA Aerospace Sciences Meeting and Exhibit*. 2007, p. 118.

[26] H. Görtler. 'Über eine dreidimensionale Instabilität laminarer Grenzschichten an konkaven Wänden'. PhD thesis. Universität Göttingen, 1940.

[27] M. S. Loginov, N. A. Adams and A. A. Zheltovodov. 'Large-eddy simulation of shock-wave/turbulent-boundary-layer interaction'. *Journal of Fluid Mechanics* 565 (2006), pp. 135–169.

[28] G. Simeonides. *Hypersonic shock wave boundary layer interactions over simplified deflected control surface configurations*. Tech. rep. AGARD Tech Report AR-792, 1993.

[29] M. Grilli, S. Hickel and N. A. Adams. 'Large-eddy simulation of a supersonic turbulent boundary layer over a compression–expansion ramp'. *International journal of heat and fluid flow* 42 (2013), pp. 79–93.

[30] S. Priebe, J. H. Tu, C. W. Rowley and M. P. Martín. 'Low-frequency dynamics in a shock-induced separated flow'. *Journal of Fluid Mechanics* 807 (2016), pp. 441–477.

[31] F. Tong, X. Li, Y. Duan and C. Yu. 'Direct numerical simulation of supersonic turbulent boundary layer subjected to a curved compression ramp'. *Physics of Fluids* 29.12 (2017), p. 125101.

[32] V. Pasquariello, S. Hickel and N. A. Adams. 'Unsteady effects of strong shock-wave/boundary-layer interaction at high Reynolds number'. *Journal of Fluid Mechanics* 823 (2017), pp. 617–657.

[33] Y. Zhuang, H.-j. Tan, Y.-z. Liu, Y.-c. Zhang and Y. Ling. 'High resolution visualization of Görtler-like vortices in supersonic compression ramp flow'. *Journal of Visualization* 20.3 (2017), pp. 505–508.

[34] A. J. Smits and J.-P. Dussauge. *Turbulent shear layers in supersonic flow*. Springer Science & Business Media, 2006.

[35] F. Grasso and M. Marini. 'Analysis of hypersonic shock-wave laminar boundary-layer interaction phenomena'. *Computers & Fluids* 25.6 (1996), pp. 561–581. DOI: 10.1016/0045-7930(96)00019-9.

[36] P. Balakumar, H. Zhao and H. Atkins. 'Stability of hypersonic boundary layers over a compression corner'. *AIAA Journal* 43.4 (2005), pp. 760–767. DOI: 10.2514/1.3479.

[37] Y. Ohmichi and K. Suzuki. 'Three-Dimensional Numerical Simulation of Görtler Vortices in Hypersonic Compression Ramp'. In: *51st AIAA Aerospace Sciences Meeting Including the New Horizons Forum and Aerospace Exposition*. 2013, p. 262. DOI: 10.2514/6.2013-262.

[38] S. Cao, I. Klioutchnikov and H. Olivier. 'Görtler Vortices in Hypersonic Flow on Compression Ramps'. *AIAA Journal* 57.9 (2019), pp. 3874–3884. DOI: 10.2514/1.J057975.

[39] V. Theofilis. 'Advances in global linear instability analysis of nonparallel and three-dimensional flows'. *Progress in aerospace sciences* 39.4 (2003), pp. 249–315.

[40] V. Theofilis. 'Global linear instability'. *Annual Review of Fluid Mechanics* 43 (2011), pp. 319–352.

[41] K. Taira, S. L. Brunton, S. T. Dawson, C. W. Rowley, T. Colonius, B. J. McKeon, O. T. Schmidt, S. Gordeyev, V. Theofilis and L. S. Ukeiley. 'Modal analysis of fluid flows: An overview'. *AIAA Journal* 55.12 (2017), pp. 4013–4041.

[42] V. Theofilis, S. Hein and U. Dallmann. 'On the origins of unsteadiness and three-dimensionality in a laminar separation bubble'. *Philosophical Transactions of the Royal Society of London. Series A: Mathematical, Physical and Engineering Sciences* 358.1777 (2000), pp. 3229–3246.

[43] D. Rodriguez and V. Theofilis. 'Structural changes of laminar separation bubbles induced by global linear instability'. *Journal of Fluid Mechanics* 655 (2010), pp. 280–305.

[44] G. Sidharth, A. Dwivedi, G. V. Candler and J. W. Nichols. 'Onset of three-dimensionality in supersonic flow over a slender double wedge'. *Physical Review Fluids* 3.9 (2018), p. 093901. DOI: 10.1103/PhysRevFluids.3.093901.

[45] N. Hildebrand, A. Dwivedi, J. W. Nichols, M. R. Jovanović and G. V. Candler. 'Simulation and stability analysis of oblique shock-wave/boundary-layer interactions at Mach 5.92'. *Physical Review Fluids* 3.1 (2018), p. 013906.

[46] A. Dwivedi, G. Sidharth, J. W. Nichols, G. V. Candler and M. R. Jovanović. 'Reattachment streaks in hypersonic compression ramp flow: an input–output analysis'. *Journal of Fluid Mechanics* 880 (2019), pp. 113–135. DOI: 10.1017/jfm.2019.702.

[47] J. Robinet. 'Bifurcations in shock-wave/laminar-boundary-layer interaction: global instability approach'. *Journal of Fluid Mechanics* 579 (2007), pp. 85–112.

[48] D. Barkley, M. G. M. Gomes and R. D. Henderson. 'Three-dimensional instability in flow over a backward-facing step'. *Journal of Fluid Mechanics* 473 (2002), pp. 167–190.

[49] G. A. Bres and T. Colonius. 'Three-dimensional instabilities in compressible flow over open cavities'. *Journal of Fluid Mechanics* 599 (2008), pp. 309–339.

[50] G. S. Sidharth, A. Dwivedi, G. V. Candler and J. W. Nichols. 'Global linear stability analysis of high speed flows on compression ramps'. In: *47th AIAA Fluid Dynamics Conference*. 2017, p. 3455.

[51] V. Zapryagaev, I. Kavun and I. Lipatov. 'Supersonic laminar separated flow structure at a ramp for a free-stream Mach number of 6'. *Progress in Flight Physics* 5 (2013), pp. 349–362. DOI: 10.1051/eucass/201305349.

[52] D. A. de la Chevalerie, A. Fonteneau, L. De Luca and G. Cardone. 'Görtler-type vortices in hypersonic flows: the ramp problem'. *Experimental thermal and fluid science* 15.2 (1997), pp. 69–81. DOI: 10.1016/S0894-1777(97)00051-4.

[53] S. Matsumura, S. P. Schneider and S. A. Berry. 'Streamwise vortex instability and transition on the Hyper-2000 scramjet forebody'. *Journal of Spacecraft and Rockets* 42.1 (2005), pp. 78–89.

[54] I. Klioutchnikov and H. Olivier. 'Direct Numerical Simulation of Hypersonic Flows over Compression Ramps and Study of Appearing Görtler Vortices'. In: *Proceedings of the 8th European Symposium on Aerothermodynamics for Space Vehicles*. 2015, pp. 1–15.

[55] A. Durna and B. Celik. 'Effects of Double-Wedge Aft Angle on Hypersonic Laminar Flows'. *AIAA Journal* 58.4 (2020), pp. 1689–1703.

[56] A. Dwivedi, C. J. Broslawski, G. V. Candler and R. D. Bowersox. 'Three-dimensionality in shock/boundary layer interactions: a numerical and experimental investigation'. In: *AIAA AVIATION 2020 FORUM*. 2020, p. 3011.

[57] F. Schrijer. 'Investigation of Görtler vortices in a hypersonic double compression ramp flow by means of infrared thermography'. *Quantitative Infrared Thermography Journal* 7.2 (2010), pp. 201–215.

[58] E. Schülein and V. M. Trofimov. 'Steady longitudinal vortices in supersonic turbulent separated flows'. *Journal of Fluid Mechanics* 672 (2011), pp. 451–476.

[59] P. Chuvakhov and V. Radchenko. 'Effect of Görtler-like vortices of various intensity on heat transfer in supersonic compression corner flows'. *International Journal of Heat and Mass Transfer* 150 (2020), p. 119310.

[60] P. V. Chuvakhov, I. V. Egorov, H. Olivier and A. Roghelia. 'Joint influence of high entropy layer and Goertler vortices on heat transfer in supersonic compression ramp flow'. *Computational Thermal Sciences: An International Journal* 8.6 (2016).

[61] E. Touber and N. D. Sandham. 'Large-eddy simulation of low-frequency unsteadiness in a turbulent shock-induced separation bubble'. *Theoretical and Computational Fluid Dynamics* 23.2 (2009), pp. 79–107.

[62] I. N. Kavun, I. I. Lipatov and V. I. Zapryagaev. 'Flow effects in the reattachment region of supersonic laminar separated flow'. *International Journal of Heat and Mass Transfer* 129 (2019), pp. 997–1009. DOI: 10.1016/j.ijheatmasstransfer.2018.09.125.

[63] V. Hermes. 'Numerische Untersuchung des Einflusses von stromauf laufenden Druckwellen auf die Transition im Transschall'. PhD thesis. RWTH Aachen University, 2014.

[64] M. A. Gageik. 'Direkte Numerische Simulation von Druckwellenphänomenen bei transsonischer Profilumströmung'. PhD thesis. RWTH Aachen University, 2017.

[65] G. Jiang and C.-W. Shu. 'Efficient implementation of weighted ENO schemes'. *Journal of Computational Physics* 126.1 (1996), pp. 202–228. DOI: 10.1006/jcph.1996.0130.

[66] I. Klioutchnikov. *Numerical Simulation at SWL*. URL: http://www.swl.rwth-aachen.de/en/numerical-simulation/ (visited on 04/09/2020).

[67] V. Hermes, I. Klioutchnikov and H. Olivier. 'Linear stability of WENO schemes coupled with explicit Runge–Kutta schemes'. *International Journal for Numerical Methods in Fluids* 69.6 (2012), pp. 1065–1095. DOI: 10.1002/fld.2626.

[68] V. Hermes, I. Klioutchnikov and H. Olivier. 'Numerical investigation of unsteady wave phenomena for transonic airfoil flow'. *Aerospace Science and Technology* 25.1 (2013), pp. 224–233.

[69] M. Gageik, I. Klioutchnikov and H. Olivier. 'Comprehensive mesh study for a Direct Numerical Simulation of the transonic flow at Re_c= 500,000 around a NACA 0012 airfoil'. *Computers & Fluids* 122 (2015), pp. 153–164. DOI: 10.1016/j.compfluid.2015.08.030.

[70] M. Gageik, J. Nies, I. Klioutchnikov and H. Olivier. 'Pressure wave damping in transonic airfoil flow by means of micro vortex generators'. *Aerospace Science and Technology* 81 (2018), pp. 65–77.

[71] I. Klioutchnikov, S. Cao and H. Olivier. 'DNS of Hypersonic Ramp Flow on a Supercomputer'. In: *International Symposium on Shock Waves*. Springer. 2017, pp. 897–903. DOI: 10.1007/978-3-319-91017-8_112.

[72] S. Cao, I. Klioutchnikov and H. Olivier. 'Influence of the separation bubble flow at a compression ramp on Görtler-type vortices'. In: *Proceedings of the 32nd International Symposium on Shock Waves*. 2019, pp. 899–909. DOI: 10.3850/978-981-11-2730-4_0052-cd.

[73] S. Cao, I. Klioutchnikov and H. Olivier. 'Görtler Number Evaluation for Laminar Separated Hypersonic Compression Ramp Flow'. *AIAA Journal* 58.8 (2020), pp. 3706–3710.

[74] S. Pirozzoli. 'Numerical methods for high-speed flows'. *Annual review of fluid mechanics* 43 (2011), pp. 163–194.

[75] C.-W. Shu and S. Osher. 'Efficient implementation of essentially non-oscillatory shock-capturing schemes'. *Journal of Computational Physics* 77.2 (1988), pp. 439–471. DOI: 10.1016/0021-9991(88)90177-5.

[76] C. Hirsch. *Numerical computation of internal and external flows: The fundamentals of computational fluid dynamics*. Elsevier, 2007.

[77] M. Gageik and I. Klioutchnikov. *SHOCK*. URL: https://www.fz-juelich.de/ias/jsc/EN/Expertise/High-Q-Club/SHOCK/_node.html/ (visited on 04/09/2020).

[78] A. Roghelia. *Einfluss einer Entropieschicht auf die Ausbildung von Görtler Wirbeln in einer Hyperschallströmung*. Tech. rep. Shock Wave Laboratory, Germany, 2017.

[79] J. D. Anderson Jr. *Hypersonic and high-temperature gas dynamics*. American Institute of Aeronautics and Astronautics, 2006.

[80] M. L. Rasmussen and D. R. Boyd. *Hypersonic flow*. Wiley, 1994.

[81] J. L. Stollery. 'Hypersonic viscous interaction on curved surfaces'. *Journal of Fluid Mechanics* 43.3 (1970), pp. 497–511. DOI: 10.1017/S0022112070002549.

[82] F. M. White and I. Corfield. *Viscous fluid flow*. Vol. 3. McGraw-Hill New York, 2006.

[83] E. Eckert. *Engineering relations for friction and heat transfer to surfaces in high velocity flow*. 1955.

[84] I. Nompelis and G. V. Candler. 'US3D predictions of double-cone and hollow cylinder-flare flows at high-enthalpy'. In: *44th AIAA Fluid Dynamics Conference*. 2014, p. 3366. DOI: 10.2514/6.2014-3366.

[85] G. V. Candler, H. B. Johnson, I. Nompelis, V. M. Gidzak, P. K. Subbareddy and M. Barnhardt. 'Development of the US3D code for advanced compressible and reacting flow simulations'. In: *53rd AIAA Aerospace Sciences Meeting*. 2015, p. 1893. DOI: 10.2514/6.2015-1893.

[86] S. L. Gai and A. Khraibut. 'Hypersonic compression corner flow with large separated regions'. *Journal of Fluid Mechanics* 877 (2019), pp. 471–494. DOI: 10.1017/jfm.2019.599.

[87] S. Mallinson, S. Gai and N. Mudford. 'The interaction of a shock wave with a laminar boundary layer at a compression corner in high-enthalpy flows including real gas effects'. *Journal of fluid mechanics* 342 (1997), pp. 1–35. DOI: 10.1017/S0022112097005673.

[88] M. S. Holden. *Theoretical and experimental studies of the shock wave-boundary layer interaction on compression surfaces in hypersonic flow*. Tech. rep. CORNELL AERONAUTICAL LAB INC BUFFALO NY, 1970.

[89] D. H. Rudy, J. L. Thomas, A. Kumar, P. A. Gnoffo and S. R. Chakravarthy. 'Computation of laminar hypersonic compression-corner flows'. *AIAA Journal* 29.7 (1991), pp. 1108–1113. DOI: 10.2514/3.10710.

[90] F. Grasso and M. Marini. 'TVD multigrid solutions of three-dimensional viscous hypersonic flows'. In: *33rd Aerospace Sciences Meeting and Exhibit*. 1995, p. 470.

[91] M. Marini. 'Analysis of hypersonic compression ramp laminar flows under sharp leading edge conditions'. *Aerospace Science and Technology* 5.4 (2001), pp. 257–271. DOI: 10.1016/s1270-9638(01)01109-9.

[92] H. S. Lee, J. H. Lee, G. Park, S. H. Park and Y. H. Byun. 'Three-dimensional supersonic flow around double compression ramp with finite span'. *Shock Waves* 27.1 (2017), pp. 69–77. DOI: 10.1007/s00193-016-0630-7.

[93] S. Cao, J. Hao, I. Klioutchnikov, H. Olivier and C.-Y. Wen. 'Unsteady effects in a hypersonic compression ramp flow with laminar separation'. *Journal of Fluid Mechanics* 912 (2021).

[94] G. Inger. 'Three-dimensional heat-and mass-transfer effects across high-speed reattaching flows'. *AIAA Journal* 15.3 (1977), pp. 383–389.

[95] P. Welch. 'The use of fast Fourier transform for the estimation of power spectra: a method based on time averaging over short, modified periodograms'. *IEEE Transactions on audio and electroacoustics* 15.2 (1967), pp. 70–73.

[96] P. J. Schmid. 'Dynamic mode decomposition of numerical and experimental data'. *Journal of fluid mechanics* 656 (2010), pp. 5–28.

[97] M. R. Jovanović, P. J. Schmid and J. W. Nichols. 'Sparsity-promoting dynamic mode decomposition'. *Physics of Fluids* 26.2 (2014), p. 024103.

[98] D. M. Bushnell and L. M. Weinstein. 'Correlation of peak heating for reattachment of separated flows.' *Journal of spacecraft and rockets* 5.9 (1968), pp. 1111–1112. DOI: 10.2514/3.29432.

[99] J. J. Ginoux. *Laminar boundary layers*. Tech. rep. Course Note 104, von Karman Institute for Fluid Dynamics, Belgium, 1978.

[100] G. Simeonides. 'Hypersonic shock wave boundary layer interactions over compression corners'. PhD thesis. University of Bristol, 1992. DOI: 10.12681/eadd/28688.

[101] D. R. Chapman, D. M. Kuehn and H. K. Larson. 'Investigation of separated flows in supersonic and subsonic streams with emphasis on the effect of transition'. *NACA TR 1356* (1958).

[102] O. Burggraf. *Asymptotic theory of separation and reattachment of a laminar boundary layer on a compression ramp*. Tech. rep. OHIO STATE UNIV RESEARCH FOUNDATION COLUMBUS, 1975. URL: https://apps.dtic.mil/dtic/tr/fulltext/u2/a010861.pdf.

[103] G. Korolev, J. Gajjar and A. Ruban. 'Once again on the supersonic flow separation near a corner'. *Journal of Fluid Mechanics* 463 (2002), pp. 173–199. DOI: 10.1017/S0022112002008777.

[104] K. Stewartson. 'On laminar boundary layers near corners'. *The Quarterly Journal of Mechanics and Applied Mathematics* 23.2 (1970), pp. 137–152. DOI: 10.1093/qjmam/23.2.137.

[105] N. El Hady and A. K. Verma. 'Growth of Goertler vorticies in compressible boundary layers along curved surfaces'. In: *14th Fluid and Plasma Dynamics Conference*. 1981, p. 1278. DOI: 10.2514/6.1981-1278.

[106] P. Hall and Y. Fu. 'On the Görtler vortex instability mechanism at hypersonic speeds'. *Theoretical and Computational Fluid Dynamics* 1.3 (1989), pp. 125–134. DOI: 10.1007/BF00417916.